6-30-2004

Design and Analysis of a Process for Melt Casting Metallic Fuel Pins Incorporating Volatile Actinides

Yitung Chen
University of Nevada, Las Vegas, yitung.chen@unlv.edu

Randy Clarksean
University of Nevada, Las Vegas

Darrell Pepper
University of Nevada, Las Vegas, darrell.pepper@unlv.edu

Annual Report

Design and Analysis of a Process for Melt Casting Metallic Fuel Pins Incorporating Volatile Actinides

Submitted to

Advanced Accelerator Applications Program
Technical Focus Area
Fuel Development Research
ATTN: Dr. Anthony Hechanova
Harry Reid Center
University of Nevada Las Vegas

Submitted by

Dr. Yitung Chen, Principal Investigator, uuchen@nye.nscee.edu
Dr. Randy Clarksean, Co-Principal Investigator, rclark@lakesplus.com
Dr. Darrell W. Pepper, Co-Principal Investigator, pepperu@nye.nscee.edu
Department of Mechanical Engineering
University of Nevada Las Vegas
4505 Maryland Parkway, Box 454027
Las Vegas, NV 89154-4027
Phone: (702) 895-1202
Fax: (702) 895-3936

Collaborators

Dr. Mitchell K. Meyer, Leader of Fabrication Development Group
Dr. Steven L. Hayes, Manager of Fuels & Reactor Materials Section
Nuclear Technology Division
Argonne National Laboratory, Idaho Falls, ID

Project Dates: 5/1/01 – 4/30/04
June 30, 2004

Table of Contents

List of Figures

Abstract

Incorporating volatile actinides, mainly americium into a metallic fuel pin (MFP) has been a serious problem due to americium's high vapor pressure. An Induction Skull Melting (ISM) system was identified by Argonne National Laboratory (ANL) as a potential furnace design to cast MFPs. Through the development of the ISM system, the nuclear waste feedstock can be melted and injected into the mold for fabricating MFPs in the advanced nuclear fuel cycles. The main phenomena in this system include: induction melting process, casting process and mass transfer process of americium. Issues related to ISM system design for casting MFPs are discussed including heating mechanisms, furnace design, melting process, casting issues, and mass transport issues of americium.

The induction melting and casting problems are analyzed numerically through coupling the commercial finite element CFD package FIDAP (Fluent, Inc.) with FORTRAN and Perl subroutines. The finite element method employed in this project is analyzed. The mass transfer process is studied as well. Various values of the material properties and input parameters were employed in the simulations and the results are compared in order to provide a better parameter estimation for the system design and real operation.

1. Introduction and Background

1.1 Introduction

The United States is embarking on a national program to develop accelerator transmutation of high-level radioactive waste (ATW) as part of the U.S. Advanced Fuel Cycle Initiative (AFCI) program at Argonne National Laboratory (ANL). Metal fuel is designed at ANL as one of the potential solutions to improve the safety characteristics of the Light Water Reactor (LWR), an antecessor of the Integral Fuel Reactor (IFR) concept. University of Nevada, Las Vegas (UNLV) has entered into a partnership with the national laboratories through the Transmutation Research Program (TRP). A series of computational models are being developed for the Task 1 of TRP program, i.e. design and simulation of an induction skull melting (ISM) system, at the Nevada Center for Advanced Computational Methods (NCACM) of University of Nevada, Las Vegas. These models are to assist in designing both in the melting of nuclear waste contains americium and the fabrication for metallic fuel pins incorporating americium.

Americium is one of the important volatile actinides, which are the major contributors to the long-term radioactivity of nuclear waste. It is a major task to recover these materials to be "burnable" after the reprocessing of spent fuel since they have a high burn-up so that a large amount of energy will be available when fissions. On the other hand, a troublesome physical property of americium is its high vapor pressure. This property makes it very easy to volatilize and hence a hazard to operators and environment is presented if released. Also, it becomes very difficult to process both in the melting of the feedstock and in the casting for MFPs incorporating americium.

Induction heating is a method that heats electrically conducting materials through the use of alternative induced electric currents due to the eddy currency loss or magnetic hysteresis in alternating magnetic fields. [9] It has very high heat efficiency , can induces stirring effect of the molten material and is a very clean heating method . [6-8] Due to the described advantages and the difficulties in processing the high vapor pressure material, americium, an ISM system was designed to cast MFPs at ANL.

A segmented-structure of the crucible is designed. This special structure makes the metal crucible act as a high electrical resistivity material during the induction heating process. According to Faraday's Law, the "skin" effect (or Kelvin effect) and the special structure, the current was created mostly in the "skin" depth and most of the energy was deposited here. The "skin" depth reaches a high temperature rapidly because of the high power density and through the heat transfer the feedstock is heated up to its melting point. [11-12] Meanwhile, the metallic crucible still has a low thermal resistivity so that a "skull" is formed since the coolant-cooled crucible freezes the outer shell of the melt.

The induction melting process in the furnace is numerically calculated through coupling the commercial finite element CFD package FIDAPÔ (Fluid Dynamics Analysis Package, a product of Fluent, Inc.) with FORTRAN and Perl subroutines. A model for melting the feedstock of volatile americium is developed and the governing equations and the CFD solving techniques for the induction melting process are discussed. FIDAP is employed to determine the power deposition profile in electrically conducting region, i.e. the feedstock. The technique is to link the 6 governing equations of induction heating process for different parts of the system to the steady

species equation which can be easily solved in FIDAP although induction heating process is actually not a CFD problem. A FORTRAN subroutine is compiled to accomplish this work. The calculated power deposition is subsequently used as a source term in the heat equation to calculate the temperature distribution in the ISM system. To fulfill this purpose another FORTRAN subroutine is coded. A quasi-steady procedure is developed to analyze systems that experience a large change in electrical properties when undergoing heating. In order to simulate an induction melting process when the feedstock material has a variable property, such as the variable electric conductivity as a function of temperature or a changing value of a output power to the system as a function of time, Perl subroutines are programmed linking to FIDAP in the simulation.

The power deposition of the induced current, the consequent "skin" effect, and "skull" formation are observed in the simulation. The numerical results presented in this report show the sensitivity of the induction-heated furnace to both the electrical and thermal conductivities.

Another important aspect of this program is the development of a casting process by which americium can be easily incorporated into MFPs. Previous experience with the traditional casting process indicates that there is the potential for large losses of americium. The present process relies on a pressure-driving (if a controlled filling pressure is expected) or a gravity-driving casting procedure to the long, thin and straw-like quartz glass, copper or stainless steel tubes. After the feed is melted the molten metal flows into the mold by gravity or through rapid pressurization. The resistance heaters were employed to preheat of the molds to a desired temperature in order to ensure the melt flows into the whole molds before it solidifies. About one hundred of MFPs can be produced in one operation.

A "pure" filling model and a "pure" solidification model is built and varous of cases are simulated respectively. Finally a casting model is set up in which the solidification takes place when filling. A Volume of Fluid technique is employed in the filling and casting process and a "slope method" is again used here for the simulation of the phase change (solidification) as a reverse process of the melting process. The flow of the molten metal is treated as an incompressible Newtonian fluid. The casting problem was also calculated numerically through through coupling FIDAP with FORTRAN subrountines. Numerical simulations are performed to study process parameters that could impact the casting process of the melt within the mold. Mold material and mold preheated temperature, filling velocities and filling pressures, are varied to study what impact these parameters might have on the casting process in order to provide a better parameter estimation for the fabrication of a MFP.

At last, a mode is developed l to analyze the transport of Americium from the melt to the vapor phase above the crucible. The model considers mass transport in the melt, vaporization at the surface, and transport through the vapor phase. The greatest problem with the model is the uncertainty of the thermodynamic properties of the proposed ternary alloy. The details of the model and the specific quantities needed for the physical properties will be discussed.

1.2 Background

1.2.1. Nuclear Power and Nuclear Fuel Cycle

According to the International Atomic Energy Agency, nuclear power plants provide about 17 percent of the world's electricity. In addition, they are considered by some to be one potential solution to the energy crisis. In the United States, nuclear power supplies approximately

15 percent of the electricity. There are more than 400 nuclear power plants around the world, with more than 100 in the United States. Some countries depend more on nuclear power for electricity than others. In France, for instance, about 75 percent of the electricity is generated from nuclear power. [1-2]

Nuclear power can come from the fission of uranium, plutonium or thorium or the fusion of hydrogen into helium. Today it is almost all uranium. The only fissionable material found in nature is U-235. A basic energy fact is that the fission of an atom of uranium produces 10 million times the energy produced by the combustion of an atom of carbon from coal.

Like coal, oil and natural gas, uranium is an energy resource, which must be processed through a series of complex steps to produce an efficient fuel for use in the generation of electricity. To prepare uranium for use in a nuclear reactor, it undergoes the steps of mining, milling, conversion, enrichment and fuel fabrication. These steps make up the 'front end' of the nuclear fuel cycle. After uranium has been used in a reactor to produce electricity it is known as 'spent fuel' and may undergo a further series of steps including temporary storage, reprocessing, and recycling before eventual disposal as waste. Collectively these steps are known as the 'back end' of the fuel cycle. Plutonium becomes part of the cycle when the fertile material U-238 is converted into fissile Pu-239. [3-5]

The various steps that make up the entire Nuclear Fuel Cycle are shown in Figure 1.

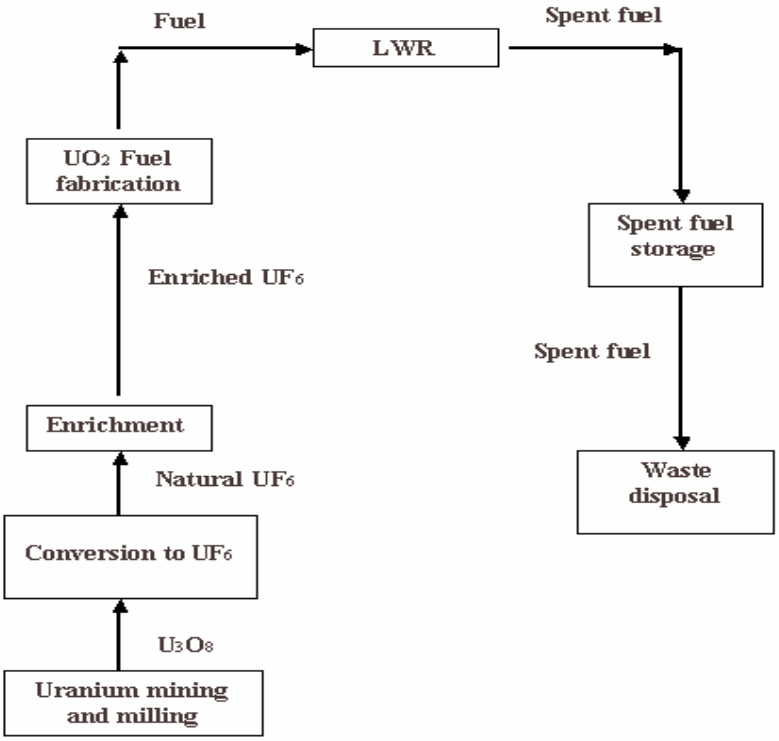

Figure 1 - The Nuclear Fuel Cycle (A once-through fuel cycle. In this cycle spent fuel is handled as waste and is prepared for permanent disposal.)

The uranium ore is mined and then sent to a mill at which the ore is crushed and ground to a fine slurry, which is leached in sulfuric acid to allow the separation of uranium from the waste rock. It is then recovered from solution and precipitated as uranium oxide (U_3O_8)

concentrate. The U_3O_8 is converted into the gas uranium hexafluoride (UF_6) at a conversion plant because uranium needs to be in the form of a gas before it can be enriched. Most of nuclear power reactors require 'enriched' uranium fuel in which the content of the U-235 isotope has been raised from the natural level of 0.7% to about 3.5% or slightly more. The typical enrichment process removes 85% of the U-238 by separating gaseous uranium hexafluoride into two streams: one stream is enriched to the required level and then passes to the next stage of the fuel cycle. The other stream is depleted in U-235 and is called 'tails'. It is predominantly U-238 and only low levels of U-235 remain in the 'tails' (usually less than 0.3%). The tails are of no further use for energy. [3-5]

The Canadian CANDU reactors don't require enriched fuel, but since they use expensive heavy water instead of ordinary water, their energy costs are about the same. [6] Then the enriched UF_6 is transported to a fuel fabrication plant where it is converted to uranium dioxide (UO_2) powder and pressed into small pellets. These pellets are inserted into thin tubes, usually of a zirconium alloy, copper, quartz glass or stainless steel, to form fuel rods. The rods are then sealed and assembled in clusters to form fuel elements or assemblies for use in the core of the nuclear reactor. Several hundred fuel assemblies make up the core of a reactor. In the reactor core the U-235 isotope fissions (or splits), producing heat in a continuous process called a chain reaction. The process depends on the presence of a moderator such as water or graphite, and is fully controlled. At the same time some of the U-238 in the reactor core is turned into plutonium and about half of this is also fissioned, providing about one third of the reactor's energy output. As in fossil-fuel burning electricity generating plants, the heat is used to produce steam to drive a turbine and an electric generator. In order to maintain efficient nuclear reactor performance, about one-third of the spent fuel is removed every year or so, to be replaced with fresh fuel.

Spent fuel assemblies taken from the reactor core are highly radioactive and give off a lot of heat. They are therefore stored in special ponds which are usually located at the reactor site, to allow both their heat and radioactivity to decrease. The water in the ponds serves the dual purpose of acting as a barrier against radiation and dispersing the heat from the spent fuel. Spent fuel can be stored safely in these ponds for long periods. It can also be dry stored in engineered facilities. However, both kinds of storage are intended only as an interim step before the spent fuel is either reprocessed or sent to final disposal. The longer it is stored, the easier it is to handle, due to radioactive decay. Some of the spent fuel is sent to long-term storage and final disposal without reprocessing as shown in Figure 1.

The spent fuel contains about 3% waste products, which are without radioactivity or with low-radioactivity. However, the spent fuel still contains approximately 96% of its original uranium (mostly U-238), of which the fissionable U-235 content has been reduced to less than 1%. [3] The remaining 1% is consists primarily of plutonium (mainly produced by the fission of U-238 in the reactor core), neptunium, americium, and curium (called transuranic elements) and long-lived isotopes of iodine and technetium created as products from the fission process in power reactors. Nearly all issues related to risks to future generations arising from long-term disposal of such spent nuclear fuel is attributable to this 1% "unburned" spent fuel. [4]

Reprocessing is necessary to recover the usable portion of the spent fuel. The typical reprocessing separates uranium and plutonium from the waste products (and from the fuel assembly cladding) by chopping up the fuel rods and dissolving them in acid to separate the various materials. Recovered uranium can be returned to the conversion plant for conversion to uranium hexafluoride and subsequent re-enrichment as shown in Figure 2. The problematical 1% reactor-grade high-level radioactive spent fuel can be blended with enriched uranium to produce

a fuel in a fuel fabrication plant. The separated plutonium can be used in a thermal Light Water Reactor (LWR), along with the uranium oxide in the "plutonium recycle". Figure 3 shows the fuel cycle with reprocessing and recycling of both uranium and plutonium.

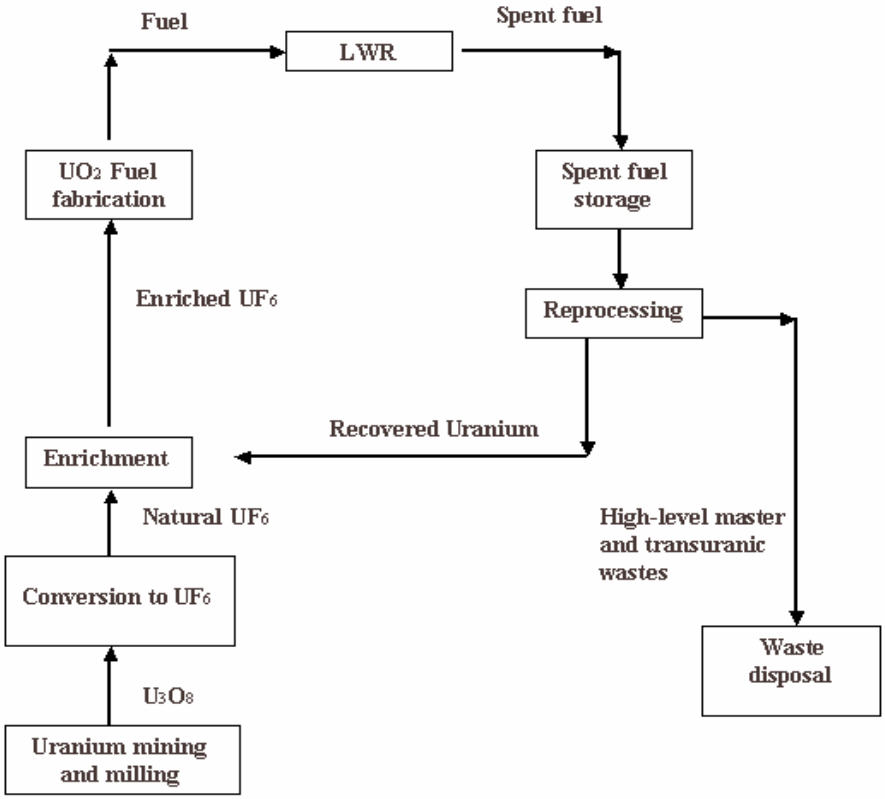

Figure 2 - Fuel cycle with uranium recovery only.

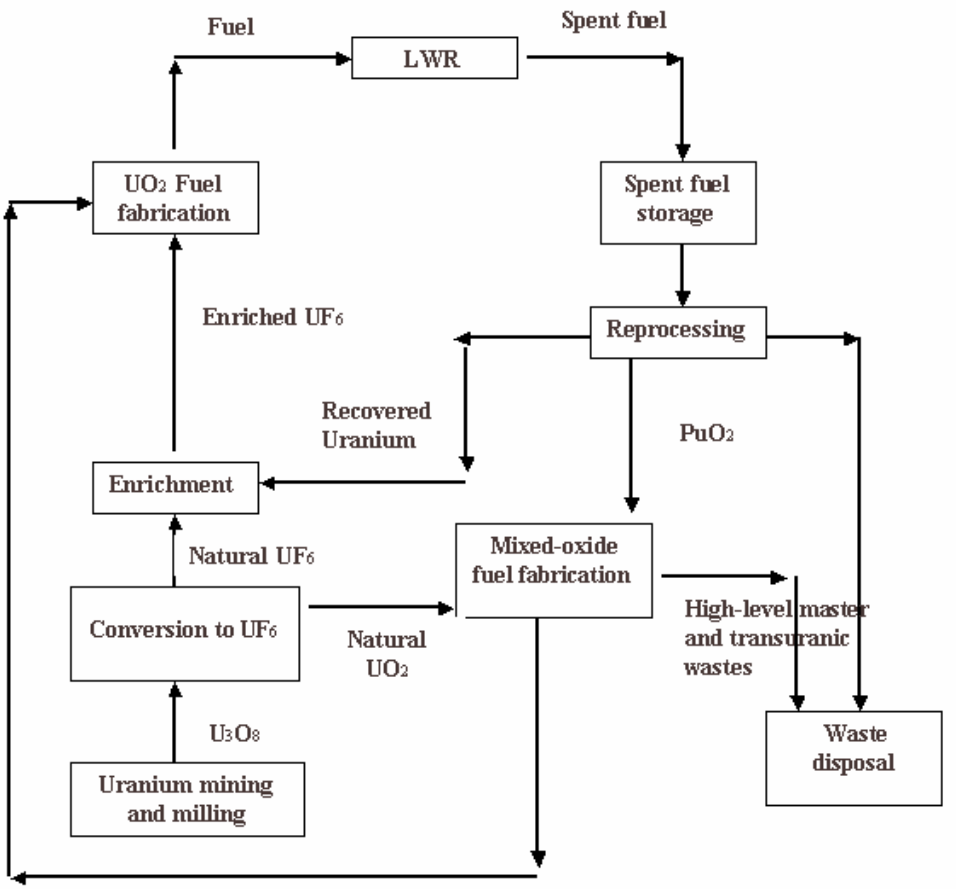

Figure 3 - Fuel cycle with reprocessing and recycling of both uranium and plutonium.

After reprocessing, the remaining high-level radioactive wastes can be stored in liquid form and subsequently be calcined (heated strongly) to produce a dry powder, which is incorporated into borosilicate (Pyrex) glass to immobilise the waste. The glass is then poured into stainless steel canisters and is readily transported and stored, with appropriate shielding. The most widely accepted plans for the final disposal are for these to be buried in stable rock structures deep underground. Many geological formations such as granite, volcanic tuff, salt or shale are suggested to be suitable. [3-5]

1.2.2. Nuclear Waste and Transmutation Technology

High-level radioactive waste is produced as a byproduct whenever nuclear fission takes place and it may remain hazardous for more than 100,000 years. In the United States, the roughly 100 operating reactors will create about 87,000 tons of discharged or "spent" fuel over the course of their lifetimes. Worldwide, there are more than 1 million tons of spent fuels from reactors, along with the defense nuclear waste, requiring disposal by year 2050. [1.2] It seems that one of the solutions for the present energy crisis, using nuclear power, will cause another crisis, that is, nuclear waste disposal.

On the other hand, the long-term hazards are posed by about 1% of the content of the spent fuel, which includes the actinides and other elements. Radioactive isotopes resulting from production of nuclear power fall into two categories: fission products and transuranium elements, also known as transuranics, actinides, or TRU. Fission products, result of nuclear power production, consist of literally hundreds of isotopes, many of them radioactive. However, they initially represent a major short-term hazard, but pose less risk even than the natural uranium ore from which the fuel material was originally extracted after only a few hundred years. Transuranics are the heavier "man-made" elements -- plutonium, americium, neptunium, curium, etc.-- that are created by other nuclear reactions in the fuel. They consist of relatively few isotopes, but they are radioactive on a geological time scale-up to several million years. So after the application of transmutation technology, the isotopes that are present in the problematical 1% (TRU) can be converted to either stable or short-lived hazards. This occurs when the TRU are exposed to neutrons in an appropriate energy range. Among which, americium has a long half-life, a high vapor pressure, and a higher burn-up. As was shown in studies made at CEA, recycling of the actinides, especially americium is mandatory in order to achieve a substantial reduction factor of the radiotoxic inventory before it is sent to geological repository. During the transmutation process in the fast reactors most of the materials in the 1% (the transuranics) will fission, release large amounts of energy and lower radioactive losses to secondary waste streams. [7,8]

Because the spent nuclear fuel contains unstable nuclei in sufficient quantities to render the material hazardous for a prolonged period of time, the process of reprocessing of the spent nuclear fuel is important. Nuclear waste transmutation is an option that arises when one examines the hazardous components in the spent nuclear fuel. Nuclear transmutation occurs every time the nucleus of an atom changes because of natural radioactive decay, nuclear fission, nuclear fusion, neutron capture, or numerous other processes.

Man has had the ability to cause transmutations to occur throughout most of the twentieth century, relying on the fission transmutation process to release and harness nuclear energy since the 1950s. Most transmutation processes that are induced involve the use of nuclear reactors or particle accelerators. In principle, any radioisotope can be produced or destroyed using nuclear transformations, although some transmutations are easier to induce than others. After applying transmutation technology, the isotopes that are present in the problematical 1% can be converted to either stable or short-lived hazards when exposed to neutrons in an appropriate energy range. Finally, most of the materials in the 1% (the transuranics) will fission, releasing large amounts of energy. [3-5]

In brief, transmutation applied to nuclear waste allows us to:

- reduce the volume, toxicity, and fissile content of waste now requiring repository disposal;
- reduce materials that create proliferation and environmental risks; and
- support a simpler repository.

1.2.3. Integral Fast Reactor and Light Water Reactor

The Integral Fast Reactor (IFR) concept addresses the most difficult problem with nuclear waste --- how to isolate it from human contact until it can decay to a level of minimal biological risk. In the IFR concept, plutonium will be recycled with uranium back into the reactor. The transuranics will stay with the fuel and become a useful constituent of the fuel in the process that separates the “unburned” fuel from the fission products. The nuclear waste leaving a multi-pass cycle IFR facility would ideally contain just fission products and be free of transuranics. The IFR offers the potential for making nuclear power a nearly unlimited resource. The benefits of the IFR can be realized without any build up of transuranic waste. Without IFR-type technology, nuclear power will only benefit a few generations of the world's population, while the care and isolation of nuclear waste will continue for eons.

It will be several decades before IFR technology could supplant current LWR technology. Virtually all the operating nuclear reactors in the world are founded on a water-moderated, water-cooled design. Regular water (H2O), as opposed to heavy water (D2O), is used in virtually all of them, so they are called "Light Water Reactors”, including boiling water reactors (BWRs) and pressurized water reactors (PWRs), the most common types used in the United States". Hydrogen (H) has one proton and one electron whereas deuterium (D), an isotope of hydrogen, has one proton, one electron, and one neutron, thereby increasing its atomic weight. [9-10] Present day LWRs operate on a once-through cycle only. As transuranium elements build up, plutonium fission produces 40% of the total energy over the life of the fuel.

Light water makes a good coolant/moderator for LWRs due to its high density, high specific heat, low viscosity, and abundance. [4] The advances in LWRs allow certain passive safety features that can greatly simplify the design and operation of the plant, for example, these passive safety features require no human intervention and are often referred to as being "inherently safe." This notion is one of the most important characteristics of an Advanced Reactors concept.

1.2.4. Nuclear Fuel

The selection of fuel for a LWR is crucial because nuclear accidents often result from situations where more heat is produced in the fuel than is carried away by the coolant. If the fuel gets hot enough, radioactive fission products will be released from the fuel because the cladding ruptures or melts.

Historically, three types of fuel have been used in nuclear reactors: Ceramic Fuel (including Carbide fuel and Oxide fuel), Particle Fuel and Metal Fuel. Liquid fuels have been tried but never used in a commercial nuclear reactor. [3]

Carbide fuel, one kind of Ceramic Fuel, is very difficult to fabricate on a large scale as it is highly pyrophoric and is highly susceptible to oxidation and hydrolysis. There is also a chemical reaction of this kind of fuel with stainless steel cladding. Swelling and cracking can be a problem and since carbide is an extremely hard material it may gouge the cladding. Moreover, reprocessing the spent carbide fuel is difficult as it is difficult to dissolve in nitric acid and leaves

behind organic complexes. Moreover, carbide fuel has attained a burn up value of just 100,000 MWday/tonne. Compare this with nearly 200,000 MWday/tonne achieved with oxide fuel in France.

Most LWRs today use uranium dioxide (UO_2) as fuel because uranium oxide has a high melting point, low vapor pressure and good mechanical stability due to the absence of metallic phase transitions. It has less swelling and chemical incompatibility than carbide. The microstructure can be controlled, which helps lower fission gas release. Also, oxide fuel is easy to fabricate as it is not pyrophoric and hence needs no inert atmosphere during fabrication.

In some cases plutonium dioxide (PuO_2) may also be mixed with the UO_2 to make mixed oxide fuel (MOX) pellets. Oxide with a fuel ratio of 30 percent plutonium oxide and 70 percent uranium oxide is a well-proven fuel world over. Neutron absorbing species, for example gadolinium, may also be mixed in at small concentrations to provide a burnable poison.

If oxide fuel and a MOX fuel are such a good choice for reactors then why the debate about using advanced fuels like nitride and metallic in future? The simple answer is that it has to do with breeding ratio. Breeding ratio is the amount of extra plutonium produced in a reactor to start a new one. Breeder technology works on the principle of self-sustenance and ability to produce more plutonium than it actually consumes to produce power. The breeding ratio is 1.1 in the case oxide fuel while it 1.2-1.3 in the case of carbide and nitride fuels. It is the maximum in the case of metallic fuel (1.4-1.5). Hence the doubling time (surplus plutonium produced to start a new reactor) is short in the case of metallic, and nitride fuels compared to oxide fuel. Using advanced fuel in lieu of oxide fuel can halve doubling time. Mixed oxide is a proven fuel but has low breeding ratio. The doubling time when advanced fuels are used will be half compared to oxide. It is a question of doubling time versus cost of power production. Moreover, the fuel pellet also cracks during normal operation in oxide fuel although the swelling is not so much a problem. [3-5]

Use of advanced fuel like nitride or metallic will reduce the time taken to make extra plutonium for a new breeder reactor.

Nitride fuel is a promising candidate for transmutation of long-lived minor actinides (MAs) such as Np, Am and Cm because of its high thermal conductivity, high fuel density and low swelling characteristics and excellent neutronics properties. The pyrochemical process, which has been developed, originally by ANL, may be applicable to the reprocessing of nitride fuel with minor modifications. Japan Atomic Energy Research Institute (JAERI) has proposed the double-strata fuel cycle, constituted by commercial power reactor fuel cycle (the first stratum) and transmutation fuel cycle (the second stratum), for transmutation of MAs. Actinide nitride is a good electric conductor and the free energy changes for the formation of chlorides from nitrides of actinides and most of fuel properties are similar to the case of metal fuel.

Metal fuel is another solution to improve the safety characteristics of the Integral Fast Reactor (IFR), as well as to a new and much simpler fuel cycle technology. Compared to oxide, metal fuel has a thermal conductivity about ten times higher than that of the ceramic fuel (ceramics are usually thought of more as insulators, rather than conductors, of both electricity

and heat). With high thermal conductivity, the heat generated by fission within the fuel slug is transferred to the coolant more effectively, resulting in a much lower temperature in the center of the fuel. This is a major safety advantage. [6,9]

1.2.5. Actinide and Americium

The elements known as the actinides are the elements from actinium (element 89) to lawrencium (element 103). All members of the series can resemble actinium in their chemical and electronic properties, and so they form a separate group within the periodic table. All actinides are metals and all are radioactive.

Actinides such as uranium, neptunium, plutonium, and americium are the major contributors to the long-term radioactivity of nuclear waste currently targeted for the proposed Yucca Mountain repository in Nevada. It is a major task to recover these materials and to then be able to "burn" them after the reprocessing of spent fuel.

Americium, element 95, was discovered in 1944-45 [11] by Seaborg et al. at the metallurgical laboratory of the university of Chicago. It is a white metallic transuranic element of the actinide series, having isotopes with mass numbers from 237 to 246 and half-lives from 25 minutes to 7,950 years. Americium is a fissionable, artificial element that can be used to produce nuclear explosives. All the isotopes of americium from Am-237 to Am-246, only Am-243 (half-life = 7600 years) and Am-241 (half-life = 433 years) are sufficiently long lived to permit accurate property studies and are the most important and the most useful for chemical research. The principal isotope, americium 241, is created as a result of the decay of plutonium 241. A troublesome physical property of americium is its high vapor pressure. The high vapor pressure makes it very easy to volatilize and hence if released, presents a hazard to operators and environment. Also, it becomes very difficult to process both in the melting of nuclear waste contains americium and the fabrication for metallic fuel pins incorporating americium. Furthermore it also has a high burn-up so a large amount of energy is available when it fission in the fuel. [12-14] The analysis above makes it very important to study and simulate the melting and casting processes incorporating americium in an ISM system.

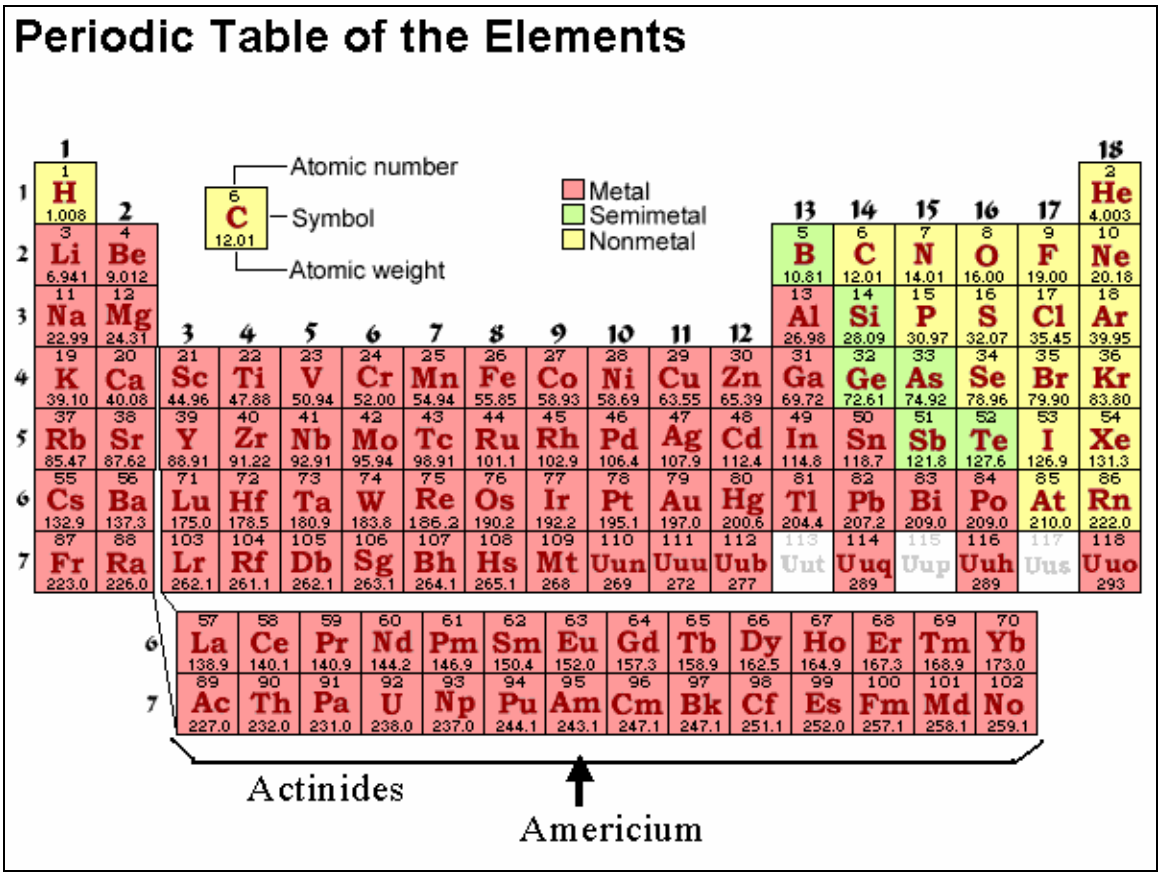

Figure 4 - Actinide and Americium in the element table.

1.3 Transmutation Research Program

The University of Nevada, Las Vegas (UNLV) has entered into a partnership with the national laboratories through the Transmutation Research Program (TRP). This program will establish a world-class program for transmutation technologies while building core competencies and facilities to promote UNLV's strategic growth goals. The central theme and purpose of this program is to involve UNLV students in research on the economically and environmentally sound refinement of spent nuclear fuel. The long-term goals of this program are to increase the University's research capabilities, attracting students and faculty of the highest caliber, while furthering the national program to address one of the nation's most pressing technological and environmental problems. A series of computational models are being developed at the Nevada Center for Advanced Computational Methods (NCACM) of University of Nevada, Las Vegas. These models are to assist in designing a fabrication process for the casting of a metallic fuel form. [15-18]

1.4 Project Objectives

Since induction heating provides high heat efficiency, induced stirring of the molten material and also combustion gas-free environment, an Induction Skull Melting (ISM) system

was selected to develop fuels for transmutation concepts as part of the U.S. Advanced Fuel Cycle Initiative (AFCI) program at ANL. Through the development of the ISM system, the nuclear waste feedstock can be melted and injected into a mold for fabricating metallic fuel pins (MFPs) used in advanced nuclear fuel cycles. However, due to the nature of high vapor pressure derived from certain actinides, such as americium, the challenge is to design a process to include high vapor pressure materials into the MFPs. From material accountability and objective of fuel fabrication standpoints, such a process is undesirable. Experience from conventional casting processes used at ANL indicated a significant amount of americium was lost through the process.

The objective of this project is to aid in the development of an ISM system through the use of computational fluid dynamic (CFD) models. These models will be used to design and evaluate the induction melting and casting processes that can facilitate the incorporation of volatile actinide elements, particularly americium, into MFPs. Various casting furnace designs have been proposed, studied and analyzed by Argonne National Laboratory, while a series of computational models are under development at the Nevada Center for Advanced Computational Methods (NCACM) of the University of Nevada, Las Vegas.

Studying, analyzing and selecting a new ISM system design initialized this research. Next, a series of computational models were developed to assist in designing the induction melting and mass transfer processes from a bench-scale furnace. The models consider the induction melting process in the melter, MFP casting, and potential mass transfer from the melt of americium.

Induction melting is an important and challenging area of engineering in which material is melted through the use of alternating electric currents. From a modeling viewpoint it is a complicated simulation process due to the interaction of various effects including the coupling of thermal and electric fields together with phase change and fluid flow. As the conductor melts a flow field develops in the molten material that in turn affects the temperature distribution. The major difficulty in analyzing such flows of the molten feedstock is the occurrence of a boundary (or interface) surface, across which latent heat jump conditions (physically the phase change process) must be satisfied and the location of which is unknown a priori. One numerical approach to these problems the "slope method," is to introduce an equivalent specific heat and viscosity. These equivalent models are curves representing the specific heat and viscosity in the numerical simulations as a function of temperature.

Two main modeling concerns for the induction skull melting process are the treatment of the electric field and the treatment of the melting process (phase change). The segmented crucible structure and how a "skull" is formed during the fast induction heating process are studied. Such segmented structure design creates a high electrical resistivity during the induction heating process. Current flow is induced near the surface of the material in the crucuble, i.e., the "skin" of the metal feedstock. This induced current generates heat in a thin layer near the surface of the material. The heat generation can be very high and lead to rapid melting.

The numerical procedure is broken out into two parts: the calculation of the induction heating field and then the heat transfer is calculated. The calculated power is used as a source term in the heat equation to calculate the temperature profile in the ISM system. The feedstock is

heated and melted quickly. However, the segmented structure crucible still has a low thermal resistivity so that a "skull" is formed because the coolant-cooled crucible freezes the outer shell of the melt.

The molten metal must them be cast into a mold to form a fuel pin. The casting process is sensitive to flow velocity, specific heat, mold thermal properties, and initial mold temperature. The improper selection of any of these conditions can easily cause the melt to solidify before it fills the whole mold.

This project analyzes the casting process for melt casting a MFP and the induction heating process. A MFP mold is a long, thin, straw-like pipe, which has a cylindrical shape. The casting process was analyzed, at first, by "dividing" it into a "pure" filling process, a "pure" solidification process and being studied respectively. In the "pure" solidification process we assume that the molten metal has filled the whole mold before the phase change takes place whereas in the "pure" filling process we assume that there is no phase change while casting. Finally we combine these two processes together to a complex casting process, i.e. VOF-solidification, (Volume of Fluid), in which the solidification takes place when filling. A "slope method" is again used here for the simulation of the phase change (solidification) as a reverse process of the melting process. The flow of the molten metal is treated as an incompressible Newtonian fluid.

The casting problem was also analyzed numerically through using FIDAP. Numerical simulations are performed to study process parameters that could impact the casting process of the melt within the mold. Mold material and mold preheated temperature, filling velocities and filling pressures, are varied to study what impact these parameters might have on the casting process in order to provide a better parameter estimation for the fabrication of a MFP.

2. Literature Survey

The United States is embarking on a national program to develop fuels for transmutation concepts as part of the U.S. Advanced Fuel Cycle Initiative (AFCI) at Argonne National Laboratory. Through this program, the U.S. joins international efforts to evaluate the potential of partitioning and transmutation along with advanced nuclear fuel cycles. Transmutation means nuclear transformation that changes the contents of the nucleus (protons and/or neutrons). This program is to develop fuel cycle technologies that enable recovery of the energy value from spent nuclear fuel from commercial plants, reduce the toxicity of high-level radioactive waste bound for geological deposit, reduce the inventories of civilian plutonium in the U.S., and to enable more effective use of the currently proposed geologic repository. The research and development efforts will consider a coupled accelerator and sub-critical multiplying assembly, explore the transmutation of waste from used nuclear fuel, testing of advanced nuclear fuels, and the production of isotopes that may be required for national security and commercial applications. [15-18]

As mentioned in Chapter 1, huge-amount, high-level, and long-hazard radioactive waste is produced whenever nuclear fission takes place. However, the isotopes that are present in the

problematical 1% can be converted to either stable or short-lived hazards if a transmutation technology is applied. The desire to reduce the long term radiologic hazard associated with the disposal of spent nuclear fuel has motivated numerous studies in several countries of ways to destroy the transuranium products of fuel irradiation. [19-23] Key features of the Integral Fast Reactor (IFR) concept include the metallic fuel and inexpensive techniques being developed for fuel reprocessing form and the compact (pyrometallurgical process) and refabrication (injection - casting). [23,24] With a much higher thermal conductivity to keep the center of the fuel at a lower temperature, mental fuel is crucial to the safety of IFR. To produce the MFP, especially from the long-term hazardous nuclear waste, is a challenge task for the future advanced reactors. [11,12,25,26]

The AFCI program requires a non-fertile actinide form to serve as the "fuel" for the transmuter blanket. The AFCI program has listed several critical issues in fuel requirements: cladding integrity, fission product retention, and dimensional, chemical, and metallurgical stability during irradiation under both normal and off-normal conditions. The currently proposed candidates for this fuel form still include a metallic alloy fuel, a ceramic fuel, and a nitride fuel. Each of these candidates has been proposed based on known performance of the fertile fuel (i.e., uranium) analogue. One of the potential fuel types is a metallic fuel, which is being developed by Argonne National Laboratory (ANL). An important aspect of this program is the development of an ISM system by which volatile actinide elements (i.e., americium) can be easily incorporated into MFPs. The current process for fabricating metal fuel relies on a traditional casting process using induction heating and quartz glass. This process works well for the fabrication of MFPs traditionally composed of alloys of uranium and plutonium, but does not work well when highly volatile actinides (i.e., americium) are included in the melt. [11,12,15-18,26]. Trybus observed that in their experiment of casting for metallic U-20%Pu-10%Zr (by weight) nuclear fuel with the addition of two minor actinides, 2.1% Am and 1.3% Np, only about 60% of the initial Am was present in the as-cast fuel even though 100% of the Np charge was captured. This potential for large losses of americium was attributed to volatile contaminants in the feedstock and evaporation at the high casting temperature (1465°C). [25] The high vapor pressure actinides, particularly americium, loss most likely occurs both during the extended time period required to superheat the alloy melt as well as when the chamber must be evacuated. Americium is susceptible to rapidly vaporize and transport throughout the casting furnace, resulting in only a fraction of the charge being incorporated into the fuel pins as desired. This is undesirable both from a materials accountability standpoint as well as from the failure to achieve the objectives of including actinides in the fuel for transmutation. [12,19-21] Americium volatility during fabrication and irradiation, and actinide compatibility with cladding are also very important fuel issues. [11-12] The chamber pressure could be increased to decrease the evaporation of americium. Inert gas can be filled in the chamber, since the addition of an inert gas in a chamber increases the recondensation of the volatile elements and consequently reduces the americium evaporation losses. Another technique might be to react the americium to another material to form a material that has a higher vapor pressure. [27-29]

Induction heating is used in a number of industrial applications for rapid heating of metals. Induction heating has very high heat efficiency and induces continuous stirring of the molten material as well, which helps to guarantee the uniformity of composition and temperature of the melt. It combines the advantages of induction melting and cold crucible melting and is

easy to control the super-heat temperature and avoid contamination of the alloy melt. It is also a very clean method without combustion gases. [30-32] Due to the described advantages, the ISM system has been selected as the type of furnace for melting the spent fuel before casting MFPs in the proposed design. Induction heating is a method that heats electrically conducting materials by eddy currency loss or magnetic hysteresis in alternating magnetic fields. [33] According to Faraday's Law and the skin effect, induction heating refers to the generation of heat energy by the current and eddy current created on the surface of a conductive object when it is placed in a magnetic field, formed by a coil, where the Alternating Current (AC) current flows. The amount of heat energy created by hysteresis is in proportion to the size of the hysteresis. It is shown that the additional energy created by hysteresis can be ignored because it is far smaller (less than 10%) than the energy generated by induction current. [30-34] Gross et al. proved that a relatively high frequency for the current is needed to decrease the power lost in the coils and the crucible. A high temperature can be achieved rapidly because of the high power density. [35-36]

A segmented structure crucible will be employed and this special structure will make the copper crucible act as a higher electric resistivity material during the induction heating process because each palisade is electrically isolated from group to group. By using the edge-based finite element method, Cingoski and Yamashita showed that the efficiency of the furnace depends to a great degree on the number and position of the palisades and the size of the gaps between them [37]. It becomes possible, however, to optimize the number and the position of the palisades by taking into consideration the electromagnetic forces, and the weight and amount of molten feedstock.

Commercial finite element method software, FIDAPÔ (Fluid Dynamics Analysis Package, a product of Fluent, Inc.) is employed to analyze this system to determine the power deposition profile in electrically conducting region, i.e. the feedstock. Before that, a "mapped" type mesh was used to discretize the geometry of our computational domain. A general-purpose pre-processor called GAMBIT was used for generating the mesh. FIDAP is a general-purpose heat transfer and fluid mechanics code based on the finite element method (FEM). Gresho and Derby [41] proposed an induction heating model to be solved within the commercial code FIDAP. The model was for simulating the induction heating process in a Czochralski crystal growth apparatus. They first applied this analysis to the case of induction heating of a metal crucible as part of a Czochralski crystal growth furnace. Based on this version of FIDAP, Martin [42] analyzed a process to grow large rectangular crystals by a Bridgman-like method, in which a crystal of virtually any geometry can be grown. With this simulation scheme the calculated power is subsequently used as a source term in the heat equation to calculate the temperature profile. The results show the sensitivity of the induction-heated furnace to electrical and thermal conductivities. [41,42]

The design of the ISM system will be analyzed and the main dimensions will be studied during the simulation. Chapter 3 will also analyze the physical model and then give a theoretical background and model equations governing casting process and induction melting process in the system. Chapter 4 will present results of the modeling, and conclusions will be given in Chapter 5.

3. Physical Model and Theoretical Background

3.1 Furnace Selection of the ISM System

Four major issues need to be considered in the furnace design: heating mechanisms, casting issues, crucible design, and americium volatility (mass transfer problem).

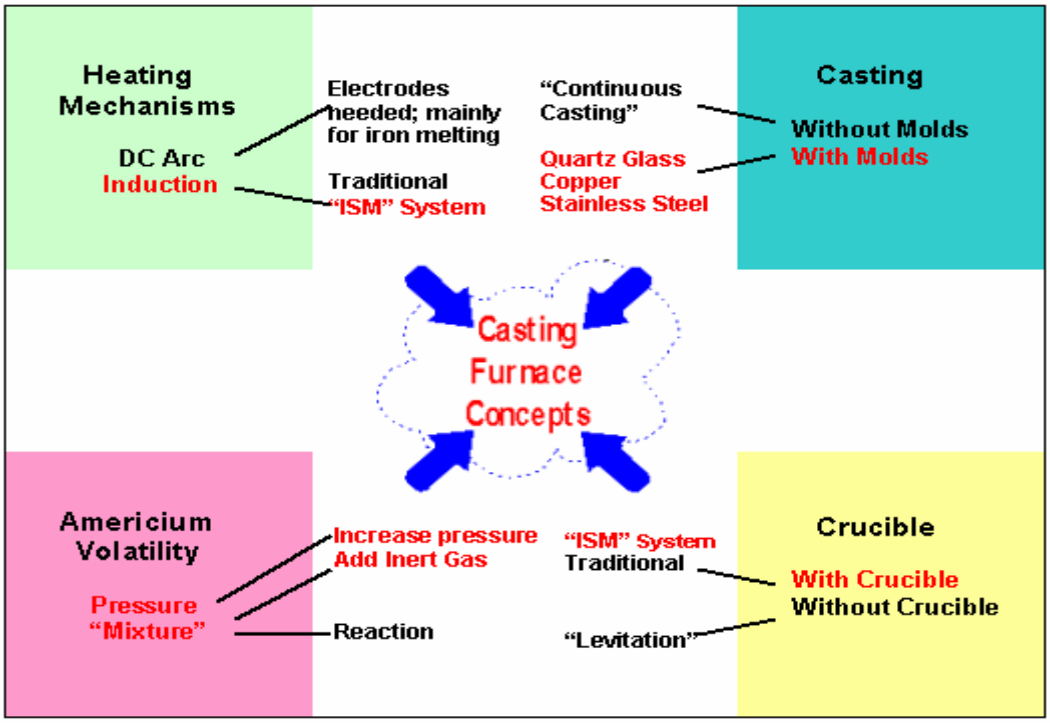

Figure 5 - Outline of mechanisms and furnace options evaluated in the design process.

Figure 5 schematically shows the main fundamental issues and different choices during the selection of the furnace design. An Induction Skull Melting system with crucible and molds is the most possible choice. As for the volatility problem of americium, some possible solutions, such as adding inert gas or increasing the crucible pressure, will be considered. The details in the furnace selection are shown in the former graduate student at NCACM of UNLV, Mr. Xiaolong Wu's thesis. [43]

Several possible candidate choices are listed in Figures 6 to 9:

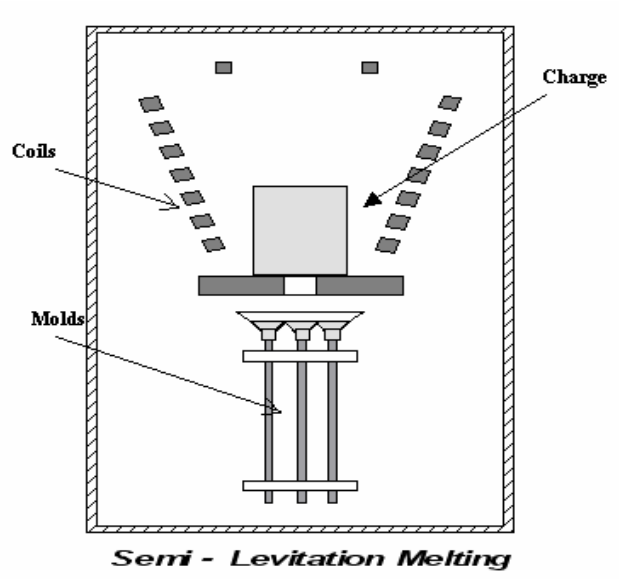

Figure 6 - Semi-levitation melting system.

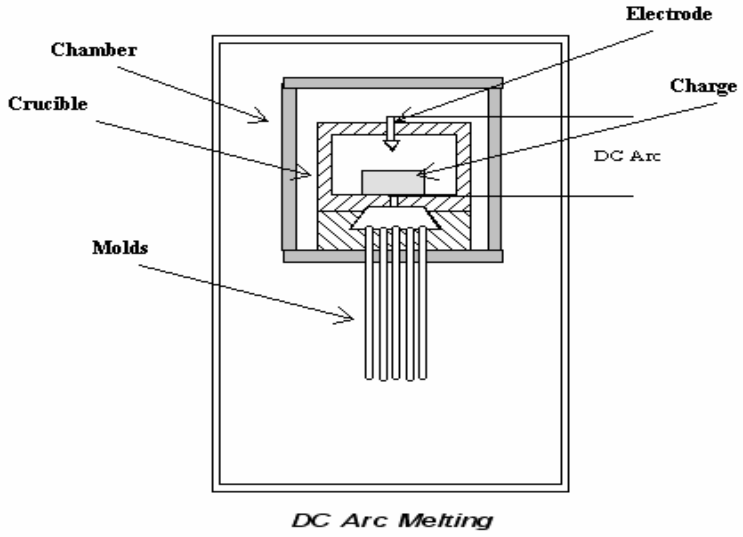

Figure 7 - DC Arc melting system with pressurized/gravity molds.

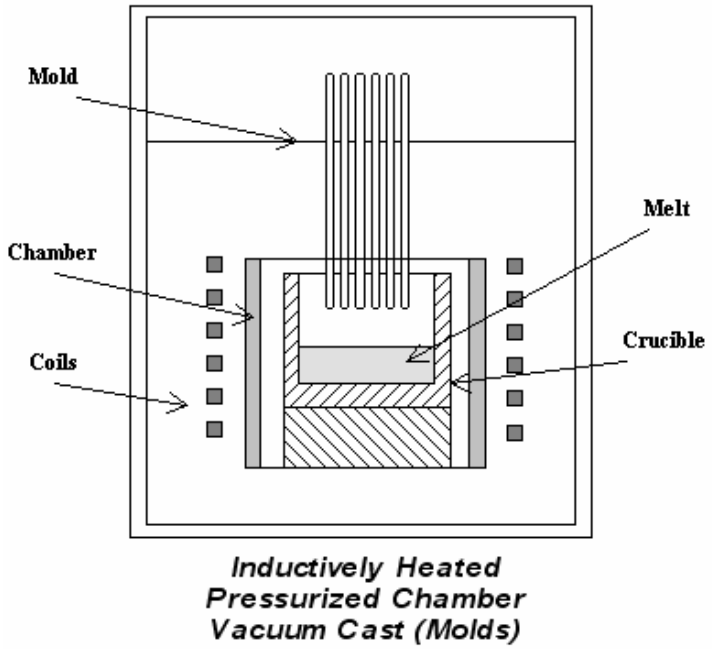

Figure 8 - Inductively heated pressurized chamber vacuum cast (molds).

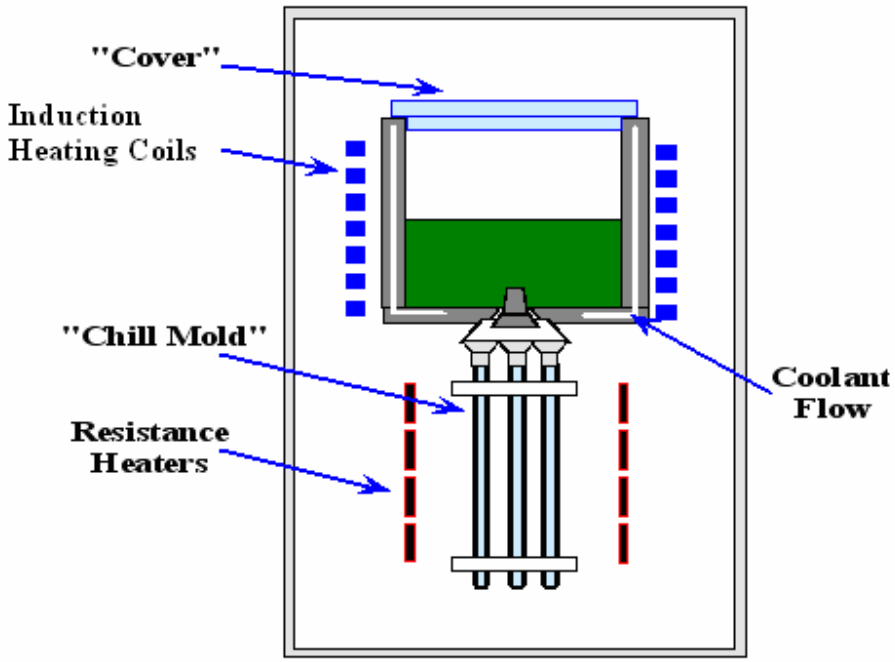

Figure 9 - Induction Skull Melting (ISM) with pressurized/gravity molds.

In order to obtain a round shape in a tight tolerance of the MFPs, molds are employed rather than the "continuous casting" method in which there is no mold used. The ability of absorbing the heat from the molten metal is the most important concern for each kind of

material. The possible material for the mold could be quartz glass, stainless steel or copper. This ability for each kind of material will be analyzed in the following chapters.

Most traditional casting furnaces have a crucible for containing the molten material. Levitation melting, as shown in Figure 6, was developed to avoid the contamination of molten metal form the crucible if the melting point of the feedstock is higher than the material of the crucible. However, this method is not suitable for the casting of americium because of its high vapor pressure. So a crucible is needed to reduce the vaporization of the americium from the feedstock. Since the feedstock has a higher melting point than the crucible's material, copper, to solve this difficulty a "skull melting" method is introduced. With the coolant inside the crucible, a "skull" region is formed along the inner surface of the crucible which can separate the molten material and the crucible so there will be no contamination of the crucible material.

An induction heating (IH) method, as shown in Figure 7, is selected since it has several merits over DC Arc heating:

- The arc heating is mainly used for melting of iron, and induction heating is used for melting of other metals.
- Higher uniformity because of the self-stirring effect of induction heating as a result of the inductive field. Furthermore, we can adjust the self-stirring effect and we can even choose a surface heating or a throughout heating by arranging the numbers and position of the induction coils, along with the frequency of the electrical field in the coils. However, DC Arc heating tends to yield a melt of an inhomogeneous temperature.
- Induction heating is a very clean method. DC Arc heating method needs one or more electrodes. The arc may destroy some species and vapors during DC Arc heating process.

Again because of americium's high vapor pressure, a vacuum melting method shown in Figure 8 will not be considered in the melting process.

Two kinds of induction melting systems with crucible usually used in industry are: induction-Slag Melting (or "USBM" system) or the induction skull melting (ISM) system.

In the 1970s the U.S. Bureau of Mines (USBM) developed an induction melting method, which includes a crucible consists of four circular quadrants brazed to a copper plate. The quadrants and base plate have integral cooling passages through which water is circulated, and refractory cement is paced where the quadrants meet. Induction coils surround the copper crucible, and the whole assembly is installed in a vacuum chamber. A metal charge, which is desired in the melt, is placed in the crucible with granular calcium fluoride add to act as an electrical insulator between the metal and the crucible to prevent arcing and crucible damage. The chamber is then evacuated and power is supplied to induction coil. Here is where the segmented crucible becomes important, because if it were not nearly all of the field generated by the induction coil could dissipate before it could melt the charge. When power is applied, the metal charge heats up, but the calcium fluoride melts first, effectively coating the crucible. As the metal melts, the water-cooled crucible freezes the outer shell of the melt, forming a titanium "skull" similar to that created in arc melting.

This process combines the advantages of induction melting and cold crucible melting. For example, using the process it is easy to control the super-heat temperature and to avoid the contamination of the interstitial elements and crucible materials to the alloy melt. Specifically, the major advantage of the ISM process is the continuous stirring, which helps to guarantee the uniformity of composition and temperature of the melt.

From the above comparison it is obvious that the ISM method is a better choice since there is no slag needs to keep the fuel from contamination. Based on the analysis above, an ISM system is selected by ANL in the system design for casting of americium.

3.2 Physical Model

The proposed process relies on an induction heating and melting procedure, and a pressure/gravity-driving casting procedure into the MFP that is briefly overviewed here. During the process the mass transfer of americium from the molten feedstock to the heated air is a very important phenomena and some new methods for controlling this transfer speed is needed. The proposed ISM concept is shown in Figure 9. The structure of the crucible, the induction coils and the cooling system are shown in Figure 10. [15-18]

The system consists of an induction skull crucible, a crucible cover, “chill” molds, and resistance heaters. The use of ”chill molds” (quartz glass, copper, stainless steel, or yet to be determined material for a cylindrical mold) assist in controlling a proper geometry for the MFPs within required tolerances.

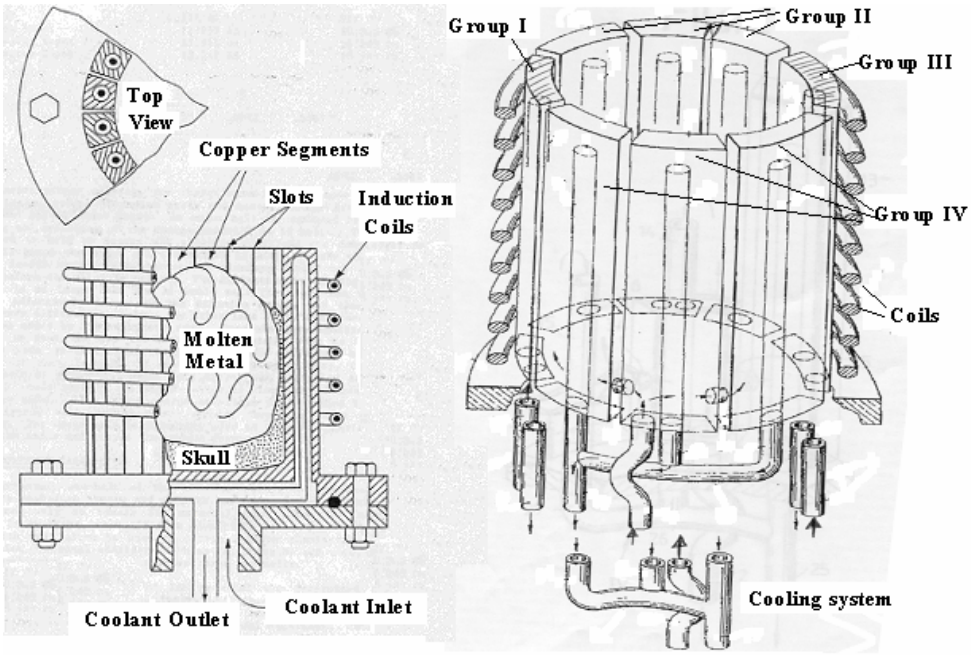

Figure 10 - Schematic of proposed ISM furnace for the casting of high americium content fuels.

The crucible cover was added to aid in controlling the transport of americium from the melt. This segmented-structure crucible consists of palisades, which are set up vertically and parallel to each other and distributed around the arc of a circle in such a way as to surround the melt. The circular palisades are brazed to a copper base plate. The palisades and base plate have integral cooling passages through which coolant is circulated, and refractory cement is placed between the palisades. The segmented structure makes the copper crucible act as a higher electric resistivity material during the induction heating process because each palisade is electrically isolated from group to group. For example, in a four-group crucible as shown in Figure 10, Group I and Group III include a single palisade whereas Group II and Group IV both have 3 palisades. Palisades in Group II or Group IV are conductive to each other because of the cooling system structure. However, they are isolated electrically to Group III and I. Thus, in our project, the current was created directly on the surface "skin" of the metal feedstock inside the crucible and the "skin" depth itself serves as the secondary circuit due to the "skin" effect or Kelvin effect. [33] Thus, most of the energy will be dissipated in the spent fuel when the power is supplied to induction coil. Induction coils surround the copper crucible, and the whole assembly is installed in a vacuum chamber. The feedstock, which consists of the end pieces chopped from previously cast fuel slugs, leftover fragments from previous casting, rejected slugs, and fresh feedstock (including actinides, americium, plutonium and zirconium), is loaded into the crucible. The feedstock is inductively heated until it is melted. The segmented-structure crucible has a pretty low thermal resistivity and a cooling system inside so that the outer shell of the melt is frozen and a "skull" is formed. Then the molten metal flows into the "chill" molds by gravity or through rapid pressurization if a controlled filling pressure is anticipated. The resistance heaters were employed to preheat of the molds to a desired temperature in order to ensure the melt flows into the whole molds before it solidifies. The casting process takes less than a second. Once filled, the molds are withdrawn from the pallet and cooled - producing about a hundred MFPs - all in one operation. [15-18,37-39]

FIDAP is employed to determine the time average power deposition profile in electrically conducting region. Then the calculated time average power deposition is subsequently used as a source term in the heat equation to calculate the temperature profile.

Several basic phenomena that need to be analyzed exist in the proposed furnace. These phenomena include:

- Induction heating on the feedstock, heat transfer, melting, and the "skull" formation in the crucible
- The flow of melt into the chill molds and solidification, and
- Transport of americium from the melt into the upper regions of the crucible region

The important physics of the induction heating process include:

- Induction heating system size, coils' number
- The current density, current frequency and other electrical parameters
- The skin effect or Kelvin effect

- Heat transfer from the melt to the crucible,
- The cooling system of the crucible and the "skull" formation
- Self-stirring effect induced by the induction current, and
- Phase change (melting) characteristics of the feedstock.

The important physics of the casting process include:

- Mold size, shape and material,
- Preheating of the molds,
- Heat transfer from the molten metal to the solidified metal, and from the metal to the mold,
- Mechanism to force the flow into the molds (pressure injection vs. gravity), and
- Phase change characteristics of the melt.

3.2.1. Induction Melting Model

At first a simple system was set up and simulated (shown in Figure 11). This simulation is a benchmark work of induction heating model in FIDAP for calculation of the two complex components (C and S, details will be discussed later) of time average power deposition. From this work, we wish to obtain the same profile of C and S as the conclusion of Philip and Jeffrey Derby [41].

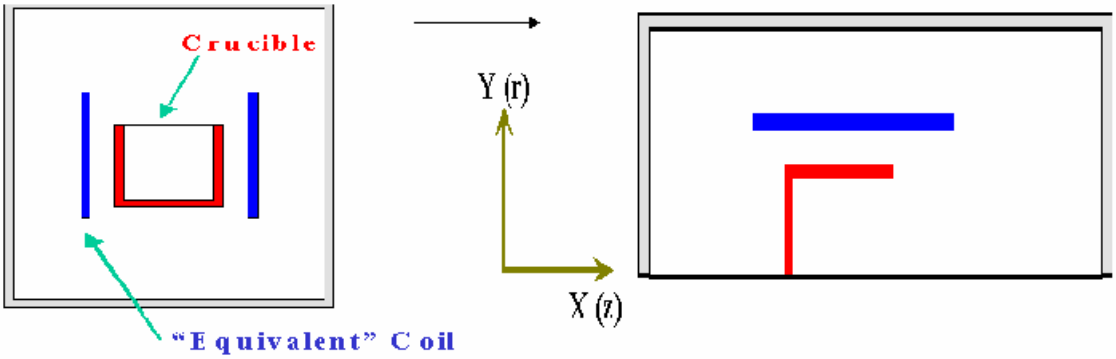

Figure 11 - The geometry of the simple system for induction heating, which can be simplified to an axisymmetric geometry.

The geometry is simplified to an axisymmetric geometry for its cylindrical shape. This simple system consists of 4 domains:

- the coil region
- the crucible
- the outer vessel
- the "filler" (all other spaces)

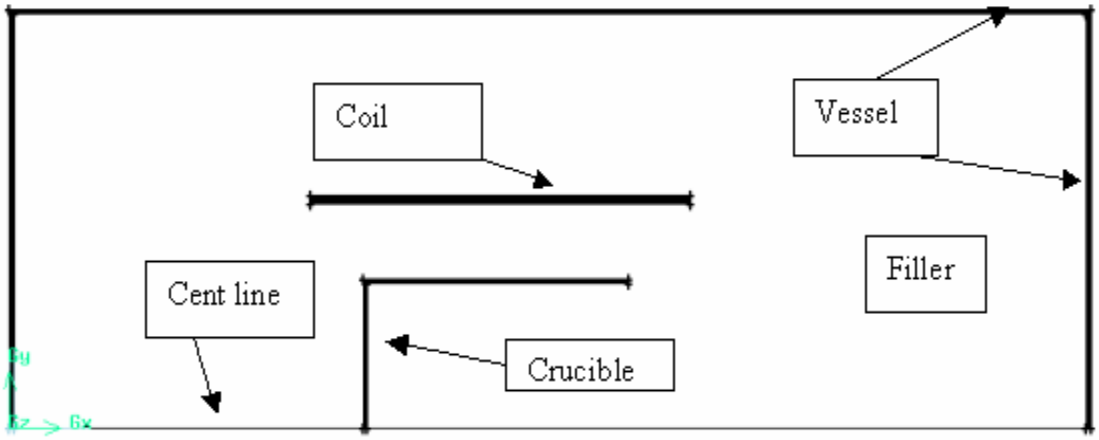

Figure 12 - The simplified geometry and the domains.

In the calculation, the crucible and the vessel will be considered as a conductor and the "filler" will be treated as an insulator. The coils are assumed to be equivalent to one coil for simplifying the problem. (The mesh can be generated in Cartesian coordinate and redefined as a cylindrical coordinate mesh for an axisymmetric geometry problem.) A general-purpose pre-processor called GAMBIT was used for generating the mesh. A "mapped" type mesh was used to discretize the geometry of our computational domain. The domains and mesh are shown as Figure 13:

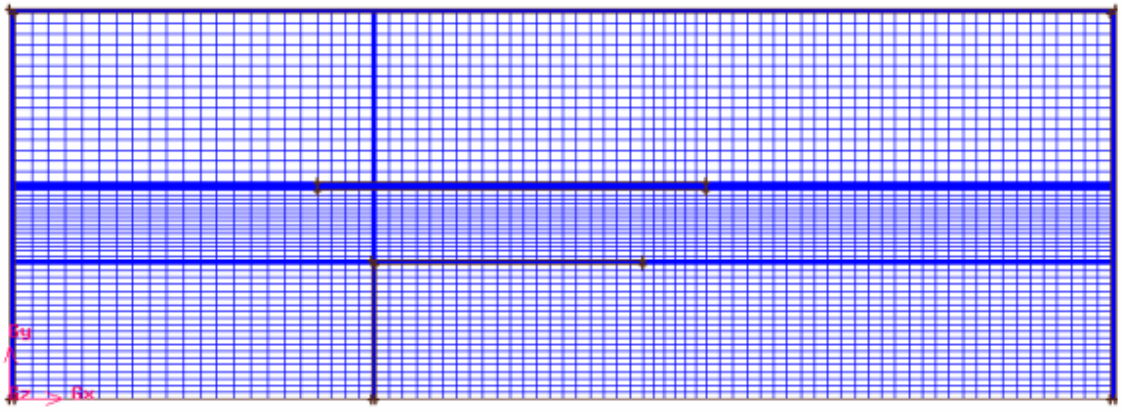

Figure 13 - The domains and mesh in GAMBIT (9095 nodes, 9248 elements).

Secondly, a more complex case shown in Figure 14 was simulated. In this system, a "melt" domain will be added. Meanwhile, a "segregated-structure" crucible is used instead of a whole metal structure crucible. Thus the crucible will be calculated as an electric insulator. This system consists of 6 domains:

- the coils (4 Coils)
- the melt
- the crucible
- the cover

- the “inspace”
- the “outspace” (all other spaces)

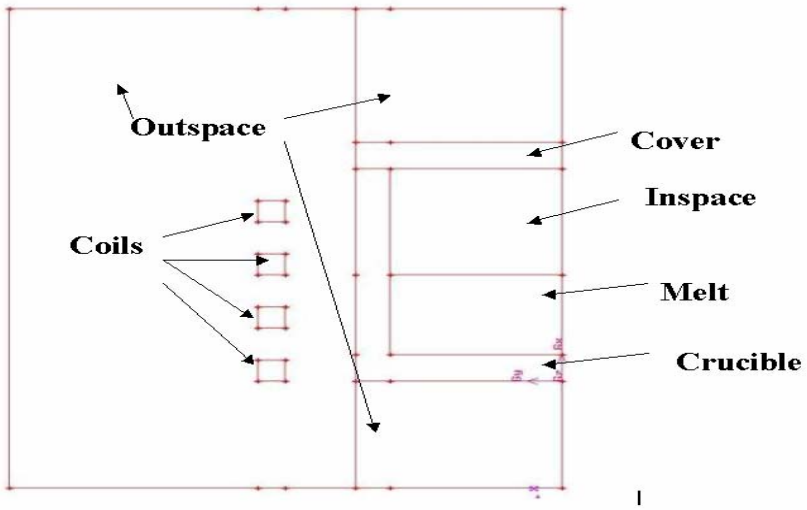

Figure 14 - Geometry and domains of the second system.

The mesh is created in GAMBIT and the mesh was compressed along the inter surface of melt and crucible.

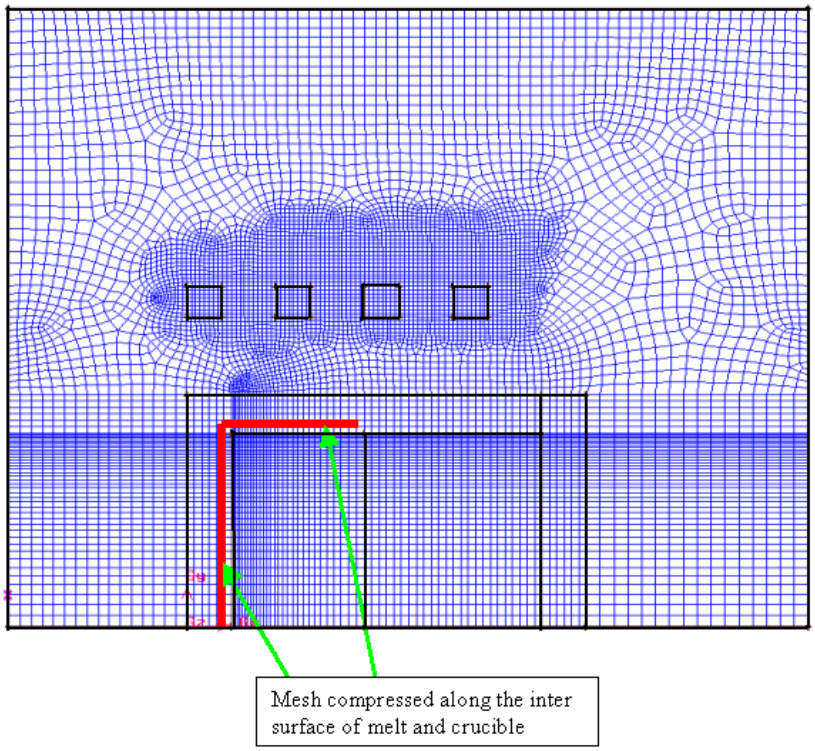

Figure 15 - Mesh of the second system (10360 nodes, 10188 elements).

After the works on the C and S, we began our work for calculation the power deposition. A benchmark ISM model for this calculation is selected. This model was developed by Gross et al. as shown in Figures 16-17. [35,36] It was simulated by a corresponding 2-D finite-element program developed at the Institute of Electroheat, University of Hanover and the results are proved agreeable to their experimental data.

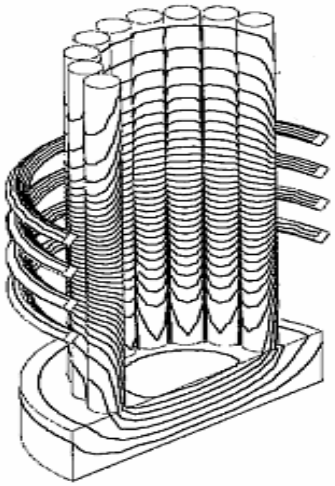

Figure 16 - One half of the crucible of the selected model [35,36]

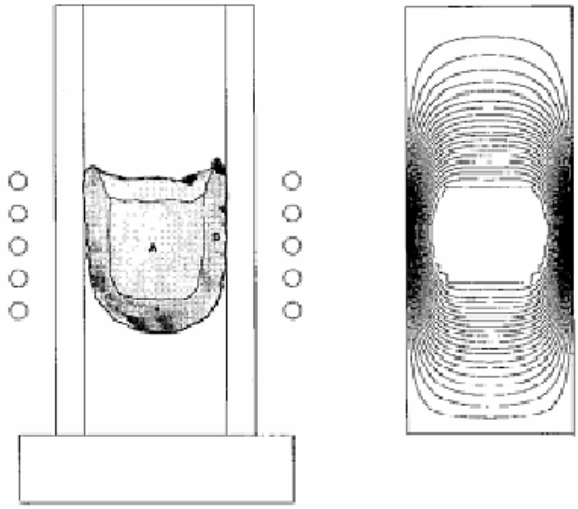

Figure 17 - Comparison of the experimentally determined shape of the molten zone (left plot) and the numerically calculated shape of the molten zone (white zone in the center of the right plot, the curves are isothermals in the unmolten material) [35,36].

According to the axisymmetric assumption discussed before, the geometry for simulation and the main dimensions studied are shown as in Figures 18 and 19:

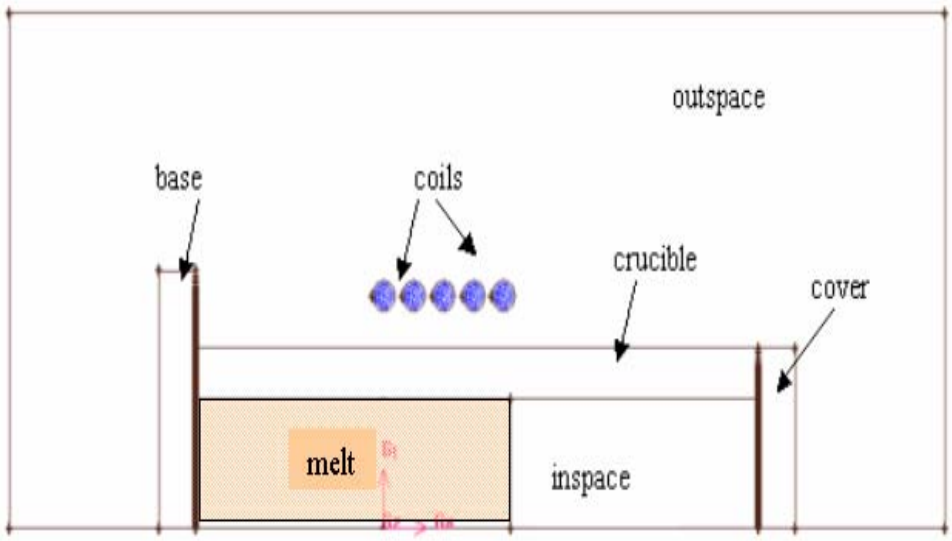

Figure 18 - The geometry of the Gross' system

This modeling process allows us to evaluated different design concepts. Different processes can be simulated, for example, direct inducting heating and indirect heating. The important dimensions in the design and the coils group number are analyzed and the results were compared for different values. Later more cases for different values of current frequency and current density are calculated. The comparisons allow us to determine which dimension has the greatest impact on the induction heating process.

A "mapped" type mesh was used for most domains. In order to generate a mapped mesh for the "outspace" domain, it was divided to 3 sub-domains. Thus, only the middle one we need to use a "pave" mesh because of the presence of the coils. The mesh was compressed near the coils, along the interface of the melt and the inner face of the crucible, and the top of the melt. The reason for this mesh compression is that a great gradient of C and S values will be located around the coils and the "skin" of the melt. Furthermore, with this division, it is easy for us to regenerate the mesh for different cases of different coil numbers, different location of coils. The only thing that we need to change is the middle sub-domain of the "outspace" whereas the other mesh can be remained unchanged.

Later we analyzed a smaller ISM furnace developed by ANL for the tests of stainless steel. Modeling efforts are underway to predict the induction heating that occurs during melting and the results are compared to the limited available test data. The axisymmetric geometry is shown in Figure 19.

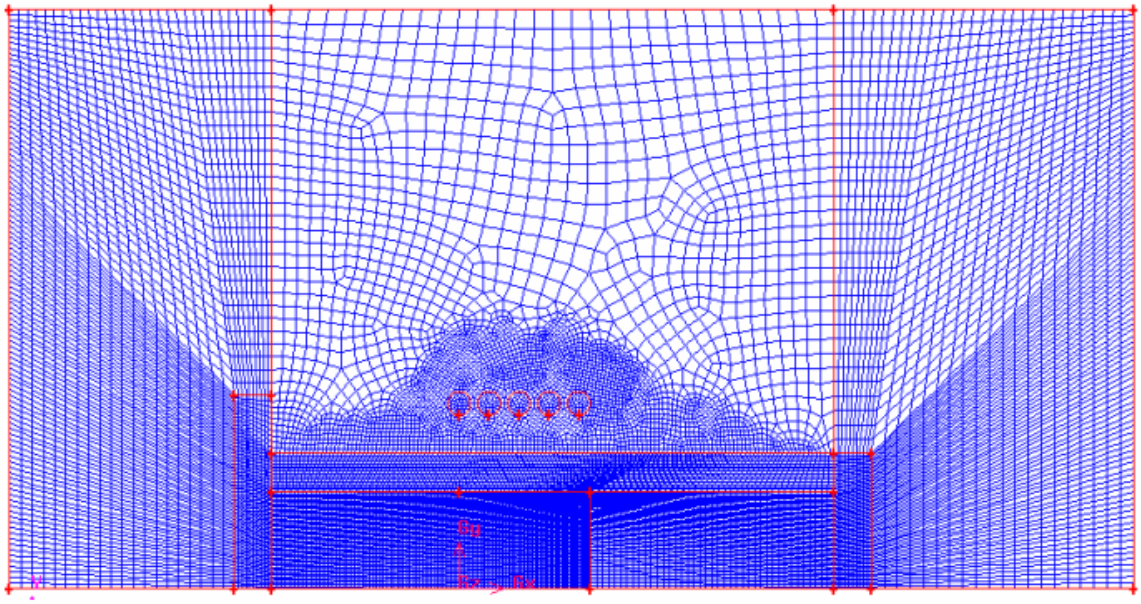

Figure 19 – Mesh of Gross' system.

The important characteristics of ANL'S crucible differs to Gross' crucible are:

- ANL's crucible is smaller (the height of is 5.5")
- More coil groups (n=9)
- Relatively larger intersection area of the coil (0.25" by 0.375" for each coil)
- A small slope of 4o at the lower part of the inner surface

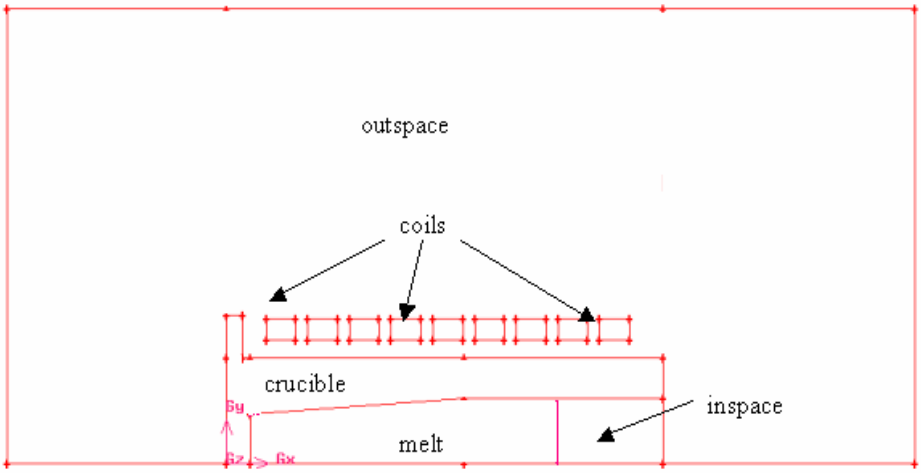

Figure 20 - Geometry of the small ISM furnace developed by ANL

The simulation scheme is similar to the former calculation for the Gross' crucible whereas we used stainless steel as the feedstock in order to compare the experimental data from ANL.

A “mapped” type mesh generated from GAMBIT is shown in Figure 21. The same ideas of domain division and mesh compression are employed here. Since this model has much faster heat efficiency, a “boundary-layer” is used along the “skin” of the metal.

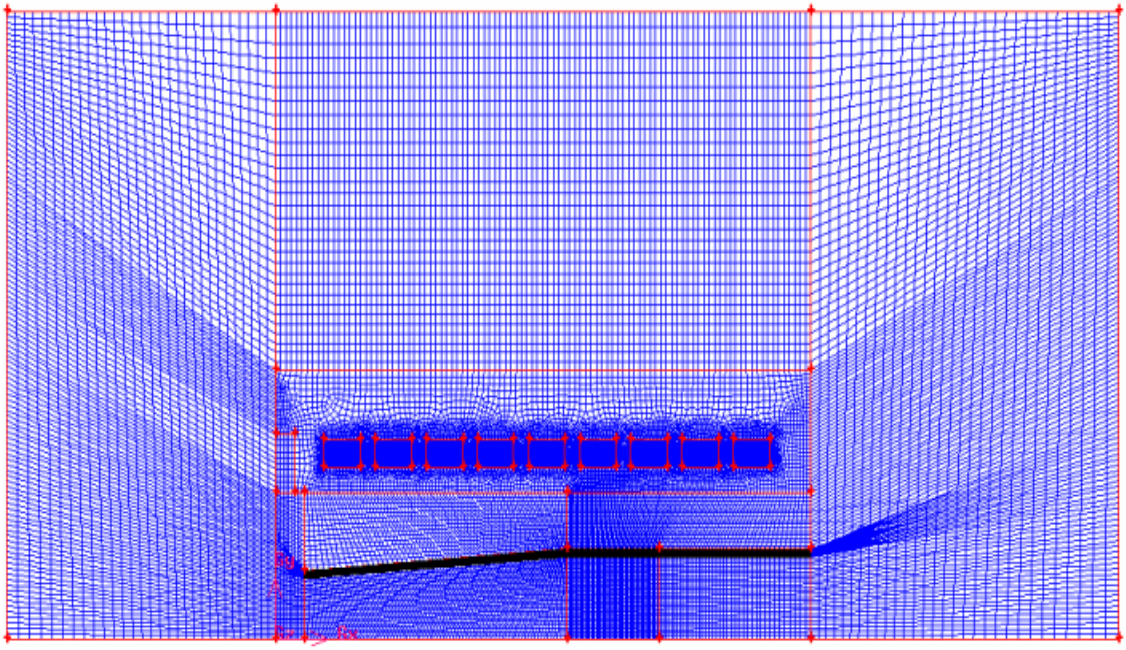

Figure 21 – Mesh of the ANL system.

3.2.2. Casting Model

The important physics of the mold casting process include the heat transfer into the mold, cooling and solidification rate of the melt, thermal mass of the mold, and the necessary forces to cause the melt to flow into the mold. The significant physics of the problem can be assessed through the analysis of a simplified geometry. Figure 22 shows a schematic of the model, which includes the melt and the mold. The problem can further be simplified through the use of an axisymmetric model, while the applied fluid is a high-temperature melt mixture of Am, Pu, Zr, etc. that is treated as an incompressible Newtonian fluid. An axisymmetric geometry is used to model the system. The inner radius of the mold is 0.004 m. The outer diameter of the mold is 0.008 m and the length is assumed to be 0.5 m.

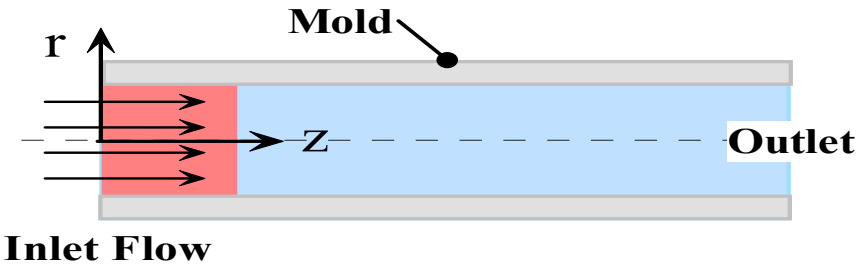

Figure 22 - Schematic of fuel rod casting model

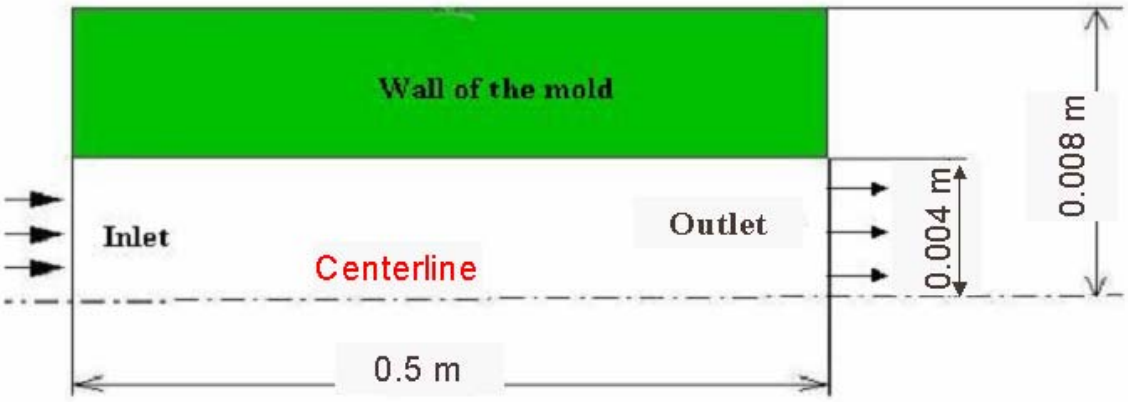

Figure 23 - Geometry of casting model.

To model the casting process, we selected three mold materials, copper, stainless steel and quartz glass. The model also considers the various boundary conditions and initial conditions, such as filling temperature, initial mold temperature, constant uniform filling velocity, constant parabolic filling velocity, constant filling pressure, and different convective heat transfer coefficient.

The modeling process was examined by two different modeling approaches. One will be referred to as filling and the other as solidification. Filling considers the flow and filling of the melt into the mold region. The "solidification" modeling approach assumes that the mold is filled with melt and that the flow is passing through the mold. This scenario would only be valid if the phenomenon is predominantly one-dimensional. One-dimensional if the flow is so rapid that heat transfer occurs predominantly in the radial direction. The results of the two approaches will be compared. From a design standpoint, if the heat transfer is predominantly one-dimensional, simple spreadsheet calculations could be used to aid in the design of a new system.

During the filling process, solidification process and casting process, several values of the initial filling velocity or filling pressure, which were taken as uniform, were employed to represent different filling mechanisms, such as the gravity filling and the pressurized filling. Through these simulations we can examine which property has the greatest influence on the solidification or filling process and then impact the casting process.

The mesh, as shown in Figure 24, was compressed near the melt-wall interface. There are 62,452 nodes and 60,000 elements altogether.

3.2.2.1. Simple Solidification Process

The analysis of "simple" or "pure" solidification considers the mold to be filled with molten material before the solidification begins. The inlet boundary condition can be either constant velocity (simplified injection), or a constant pressure condition (realistic boundary condition for injection casting). This type of analysis gives insight into the time scales one must consider for the solidification of the melt once it is in the mold. In the "simple" solidification as shown in Figure 25, a solidification process is anticipated in which the interface of the melt and

the solidified melt moves in a radial direction. Note that the inlet temperature of the melt is set to a constant temperature representative of the superheat of the melt.

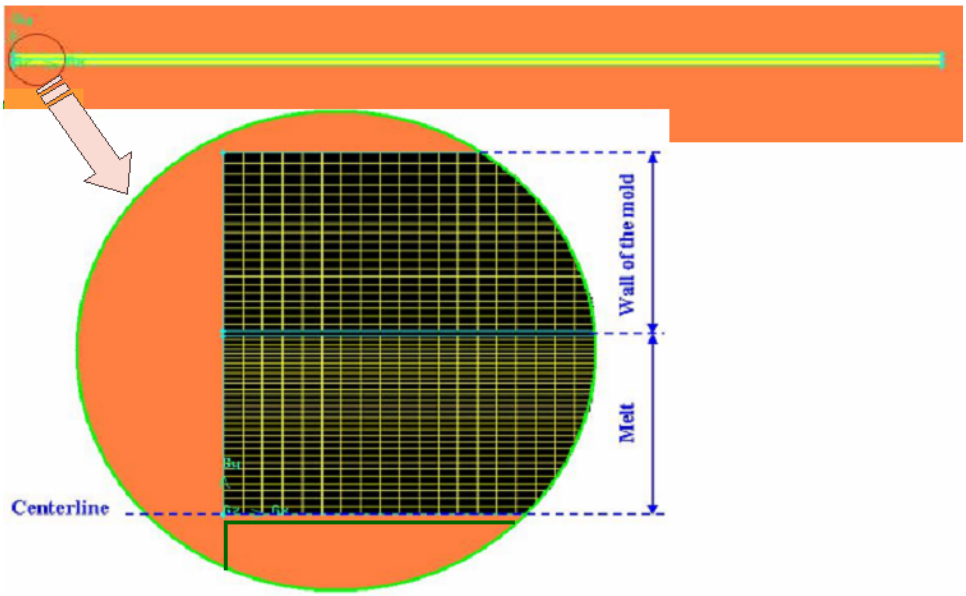

Figure 24 - Mesh of casting model.

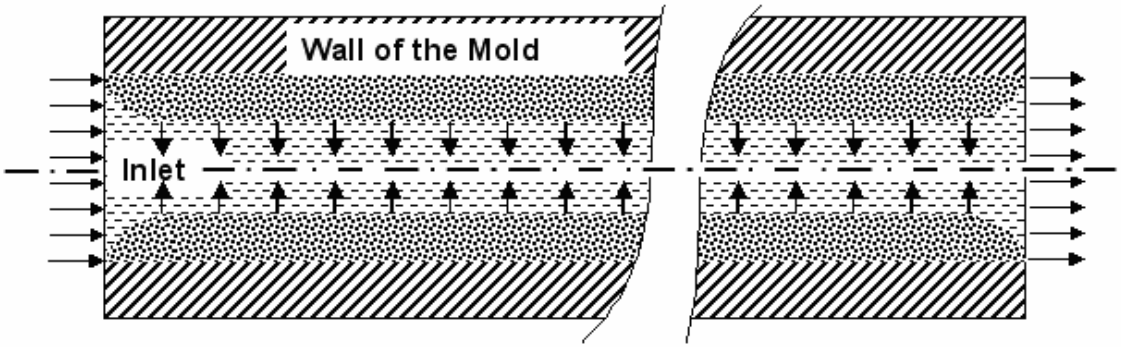

Figure 25 - The schematic of the "pure" solidification process

3.2.2.2. "Pure" filling process

The second portion of this research work involves the detailed analysis of the "pure" filling of the mold by the melt. The Volume of Fluid (VOF) technique is used to simulate the flow entering the mold. Present research efforts employ the single-fluid approach and the two-fluid scenario will be studied in the future work. In the "pure" filling process as shown in Figure 26, we wish to see a parabolic velocity profile be kept from the inlet till the leading head of the melt.

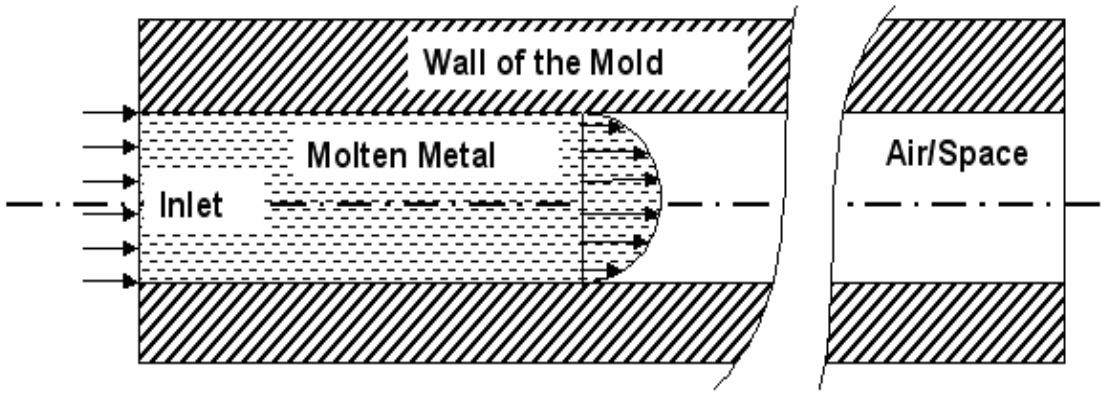

Figure 26 - The schematic of the "pure" filling process.

3.2.2.3. Casting process (VOF-solidification process)

The VOF-solidification process, shown in Figure 27, combines the filling process and the solidification together. By this simulation study the real casting problem will be studied in which the solidification will take places during the filling process.

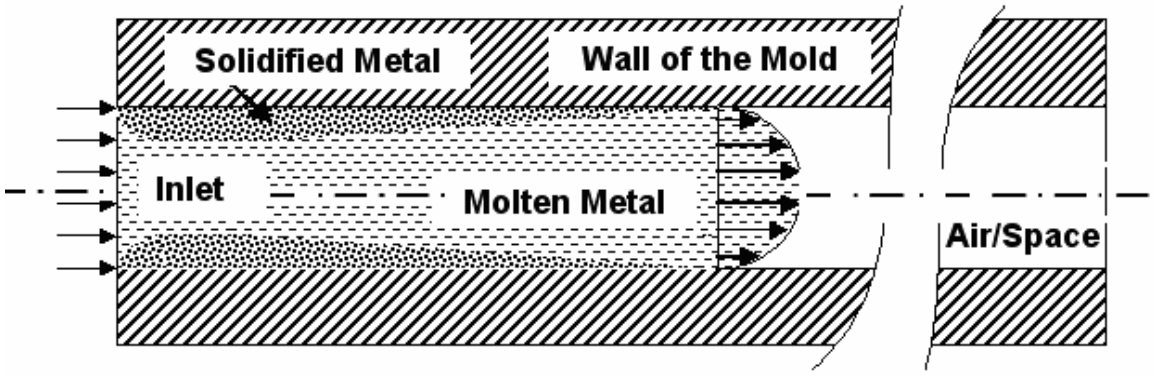

Figure 27 - The schematic of the casting process

In the VOF-solidification process, two slopes are anticipated to be observed, namely a declinational slope near the inlet of the mold and an acclivitous slope near the head of the melt. The declinational slope is because of that a constant temperature is held at the inlet and the mold-preheated temperature is much lower than this constant temperature while the acclivitous slope is due to the decreasing time for heat transfer at different location of the melt. This is the main difference between the VOF-solidification process and the "pure" solidification.

3.3 Mass Transfer Process

The mass transfer of the americium from the melt is an important consideration in the complete project. The mass transfer is best described by the schematic shown in Figure 28. References 55 through 91 were used for the development of the mass transfer model as it is presented here. The model requires the consideration and interaction of three phenomena. The mass transfer model considers the three steps of mass transport in the melt, vaporization at the surface, and transport through the vapor phase.

$$\beta_{Am} = \frac{1}{\beta_m + \beta_v + \beta_g} \tag{1}$$

where

β_{Am} = overall mass transfer coefficient.
β_m = mass transfer coefficient in molten phase.
β_v = mass transfer coefficient across liquid to vapor (interface).
β_g = mass transfer coefficient for gas phase.

Each of these mass transfer coefficients are evaluated from a thermodynamic point of view within the model.

- Mass transport within the melt to the interface region (item 1 in Figure 28). This effectively reduces to transport through a thin boundary layer type region at the surface of the melt. The mass transport coefficient is defined as β_m (cm/sec).
- Vaporization across the interface (item 2 in Figure 28). The mass transfer coefficient for this step is defined as K_m (cm/sec).
- Mass transport within the gas phase above the melt (item 3 in Figure 28). The mass transport coefficient for this step is defined as β_g (cm/sec).

The liquid boundary layer is step 1 is assumed to follow Machlin's model and can be defined as

$$\beta_m = 2\sqrt{2D\nu / \pi r}$$

where

D = diffusion coefficient
ν = speed of melt in boundary layer.
r = Machlin mode.

Each of these values can be estimated for the present system of interest.

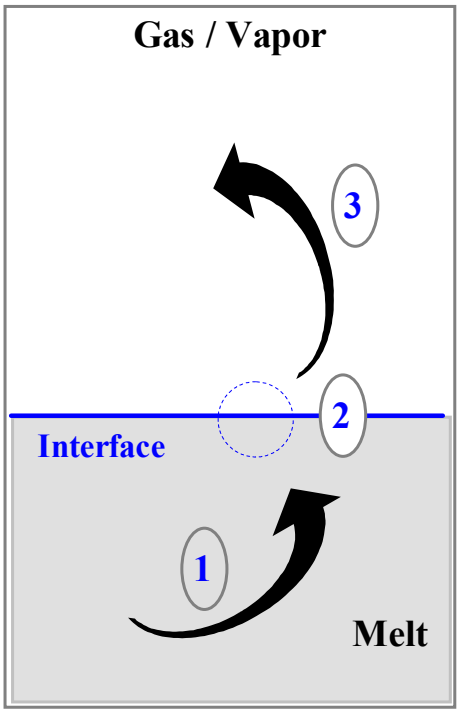

Figure 28 - Mass transport consists of (1) transport within the melt, (2) vaporization at the interface, and (3) transport in the gas phase.

The mass transfer rate across the interface (2) can be written as

$$N_m = K_m C_{ms(i)} = K_L \varepsilon (P_{e(i)} - P_{g(i)}) \sqrt{M_i / T_{ms}} \tag{1}$$

Accordingly, this allows the mass transfer coefficient to be written as

$$K_m = K_L \varepsilon (P_{e(i)} - P_{g(i)}) \sqrt{M_i / T_{ms}} \Big/ C_{ms(i)} \tag{2}$$

where

T_{ms} = temperature of the evaporating surface.
$P_{e(i)}$ = equilibrium partial pressure of component *i* at temperature T_{ms}
$P_{g(i)}$ = partial pressure of component *i* in the gas space.
K_L = Langmuir constant.
$C_{ms(i)}$ = average content of component *i* on the surface of the melt.
M_i = atomic weight of component *i*.
ε = condensation coefficient (1 for metals).

The components equilibrium partial pressure is defined as $P_{e(i)} = x_i \gamma_i P_i^o$, where P_i^o is the equilibrium pressure of pure substance *i* and x_i is the mole fraction of component *i*. The challenge for americium in our system is to evaluate γ_i, the activity coefficient.

In i-j binary system, the relationship between the activity coefficient γ_i of the component i and its partial mole excess free energy $\overline{G}_i^E$ can be written as

$$\overline{G}_i^E = RT \ln \gamma_i \tag{3}$$

in which

$$\overline{G}_i^E = G_{ij}^E + (1 - x_i) \frac{\partial G_{ij}^E}{\partial x_i} \tag{4}$$

where G_{ij}^E is the system's excess free energy and is given by

$$G_{ij}^E = \Delta H_{ij} - TS_{ij}^E \tag{5}$$

An approximate relationship between the heat formation of the binary system ΔH_{ij} and its excess entropy S_{ij}^E can be evaluated.

$$S_{ij}^E = 0.1 \Delta H_{ij} \left(\frac{T_{mi} + T_{mj}}{T_{mi} T_{mj}} \right) \tag{6}$$

where T_{mi} and T_{mj} are the melt points of components I and j, respectively. If we define

$$\beta_{ij} = 1 - 0.1T \left(\frac{T_{mi} + T_{mj}}{T_{mi} T_{mj}} \right) \tag{7}$$

Then

$$G_{ij}^E = \beta_{ij} \Delta H_{ij} \tag{8}$$

Taking the general information above and coupling it with other known thermodynamic relationships can be used to derive a relationship for the activity of Americium. Complete details of this development can be found in Appendix IV. The conclusion of these developments is shown in the equation shown below.

$$
\begin{aligned}
\ln\gamma_i \;=\; & \frac{\alpha_{ij} f_{ij}}{RT}\left[\left(\frac{x_i[1+u_i x_j(\phi_i-\phi_j)]x_j[1+u_j x_i(\phi_j-\phi_i)]}{x_i[1+u_i x_j(\phi_i-\phi_j)]V_i^{\frac{2}{3}}+x_j[1+u_j x_i(\phi_j-\phi_i)]V_j^{\frac{2}{3}}}\right)+\right. \\
& (1-x_i)\left\{\frac{(1+u_i x_j(\phi_i-\phi_j))(1+x_i u_j(\phi_j-\phi_j))}{(1+u_i x_j(\phi_i-\phi_j))x_j V_i^{\frac{2}{3}}+(1+u_j x_i(\phi_j-\phi_i))x_i V_j^{\frac{2}{3}}}+\right. \\
& \left(\frac{x_i(1+u_i x_j(\phi_i-\phi_j))x_j u_j(\phi_j-\phi_j))}{x_i(1+u_i x_j(\phi_i-\phi_j))x_j V_i^{\frac{2}{3}}+(1+u_j x_i(\phi_j-\phi_i))x_j V_j^{\frac{2}{3}}}\right)- \\
& \left(\frac{x_i(1+u_i x_j(\phi_i-\phi_j))x_j(1+x_i u_j(\phi_j-\phi_j))}{\left(x_i(1+u_i x_j(\phi_i-\phi_j))x_j V_i^{\frac{2}{3}}+(1+u_j x_i(\phi_j-\phi_i))x_j V_j^{\frac{2}{3}}\right)^2}\right)\times \\
& \left.\left.\left((1+u_i x_j(\phi_i-\phi_j))x_j V_i^{\frac{2}{3}}+u_j(\phi_j-\phi_i))x_j V_j^{\frac{2}{3}}\right)\right\}\right]
\end{aligned}
\tag{9}
$$

The variables used in Equation 9 are defined and discussed in detail in Appendix IV. The complete equation is only shown here to demonstrate the complexity of the solution.

The activities of Am in molten U-Am and Pu-Am will be calculated. Previous research efforts were focused on the transport to the melt surface and the evaporation at that interface. The additional two stages of transport are also important in the present work. The transport of the vapor through the gas phase and eventual deposition on surrounding surfaces is important. Knowing where the americium will deposit or where it will be transported is a major concern.

Once the activity coefficients are known, one can revisit the overall mass transfer coefficient and evaluate the total transfer from the melt.

$$\beta_{Am} = \frac{1}{\beta_m + \beta_v + \beta_g} \tag{10}$$

The overall mass transfer, which considers all three phenomenon is shown below. Using this relationship and assumptions relative to the rate of transfer from the melt into the gas phase, a relationship for the partial pressure of the americium in the vapor phase can be determined (see Equation 12 and Figure 29).

$$N = \beta_{Am}(C_m - C_g) \tag{11}$$

$$P_i^{t+dt} = \frac{RT(n_i^t + N^t S\,dt)}{VM_i} - \frac{R^2T^2 n_i^t (N^t S\,dt)}{PV^2 M_i} \tag{12}$$

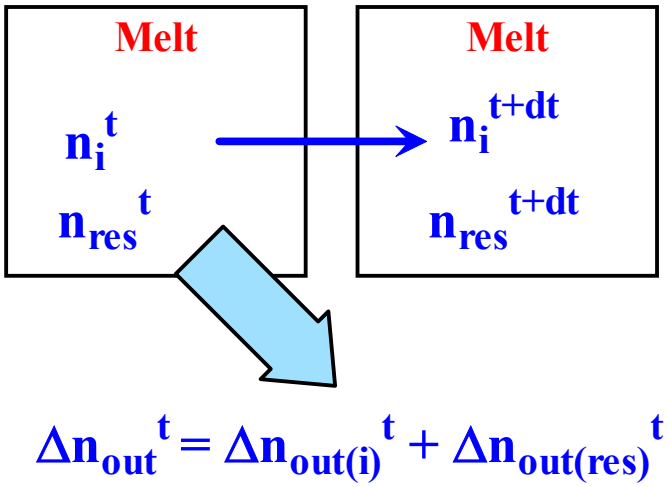

Figure 29 – Basic assumptions for mass transfer from the melt into the gas phase.

The mass transfer model is very complex and heavily relies on coefficients based on the work of Miedema in Reference 89. Further work is needed in order to fully evaluate or estimate what these constants should be within the model.

3.4 Numerical Models

3.4.1. Induction Heating Models

One can start from Maxwell's equations and derive the governing equations for a simplified geometry that includes induction heating. The current flow is assumed to be azimuthal and an axisymmetric geometry can be employed if the small pitch of the helical coils and the consequently produced axial component of the current flow can be neglected. [41,42] One ends up with a set of coupled equations for the variables C and S that can be used to calculate the heat generation due to induction heating. Complete details of the derivation can be found in references [41, 42, 44-46 and appendix VII].

For the coils:

$$\nabla \bullet (K \nabla C) = -\mu J_0 \tag{13}$$

$$\nabla \bullet (K \nabla S) = 0 \tag{14}$$

For the conductors:

$$\nabla \bullet (K \nabla C) = \frac{\mu\sigma\omega}{r} S \tag{15}$$

$$\nabla \bullet (K \nabla S) = -\frac{\mu\sigma\omega}{r} C \tag{16}$$

For all other locations:

$$\nabla \bullet (K \nabla C) = 0 \tag{17}$$

$$\nabla \bullet (K \nabla S) = 0 \tag{18}$$

where, C and S are real and complex components of time average power deposition rate $\dot{Q}'''$ and they are both functions of location and electrical parameters. The diffusivity based on K (or 1/r) is defined to assure for the proper solution of the equations. The source term is also dependent on the location within the domain as well.

The simulation of C and S is undertaken in FIDAP by the using two species equations (analogy C and S as two special species).

$$\rho_0 (\frac{\partial C_n}{\partial t} + \vec{u} \bullet \nabla C_n) = \rho_0 \nabla \bullet (\alpha_n \nabla C_n) + q_{cn} + R_n \tag{19}$$

In steady-state problem, and if we don't consider velocity for the source term Rn, we have:

$$\frac{\partial C_n}{\partial t} = 0 \tag{20}$$

$$\nabla \bullet (\alpha_n \nabla C_n) = - \frac{q_{cn}}{\rho_0} \tag{21}$$

The above equation (21) is needed for FIDAP to link the six induction heating equations (Equations (13)-(18)) relating to C and S. In the left hand side of the equation we associate C as C1 and S as C2. The right hand side uses a subroutine that is edited for different input values in different parts of the induction heating system. Once we calculate the value of C and S using FIDAP, the power deposition rate can be obtained.

Once the variables C and S have been determined, the time average power deposition can be calculated as shown below:

$$\dot{Q}''' = \frac{\sigma \omega^2}{2 r^2} (S^2 + C^2) \tag{22}$$

After the internal heating rates were calculated a transient heat transfer problem for the furnace system is simulated using the energy equation considering the proper initial and boundary conditions. A heat sink was set on the outer surface of the crucible to simulate the cooling system.

According to the skin effect or Kelvin effect, the higher the frequency of the current administered to the coils, the more intensive is the inducted current flowing around the surface of

the load. The density of the induced current diminishes near the center of the load. [33] The current density at x and the skin depth are given by the Equations (23) and (24) as below:

$$J_i(x) = J_i(0)\exp(-x/\delta) \tag{23}$$

$$\delta = \sqrt{\frac{2}{\mu\delta\omega}} \tag{24}$$

3.4.2. Induction Melting Process

The major difficulty in analyzing such flows of the molten feedstock is the occurrence of a boundary (or interface) surface, across which latent heat jump conditions must be satisfied and the location of which is unknown a priori.

One approach to these problems, "slope method" as shown in Figure 30, is to introduce an equivalent specific heat and curves of specific heat and viscosity in the numerical simulations. This scheme is the reverse of a solidification process during the MFPs' casting. [47]

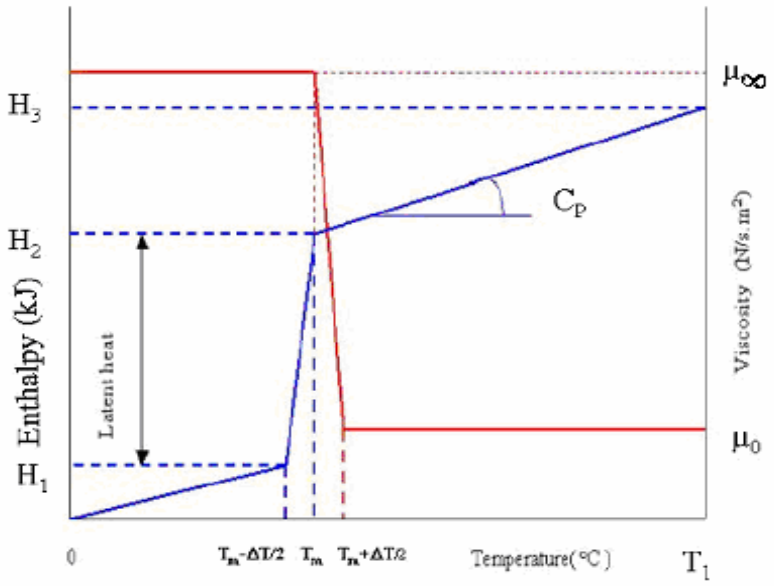

Figure 30 - Slope method (Enthalpy, specific-heat and viscosity curves).

The "slope" method for specific heat, in general, uses the slope of the enthalpy-temperature curve to define a specific heat of the material of interest. The enthalpy of a material that changes phase at a temperature T_m, is defined as

$$H(T) = \int_{T_{ref}}^{T} (C_p(T) + L\eta(T - T_m))dT \tag{25}$$

where

$$\eta(T-T_m)=\begin{cases}1 & if(T-T_m)\geq 0\\ 0 & if(T-T_m)<0\end{cases} \tag{26}$$

An equivalent specific heat can be defined as the derivative of the enthalpy function which gives

$$C_{eqiv}=\frac{dH}{dT}=C_p(T)+L\delta(T-T_m) \tag{27}$$

$$\delta(T-T_m)=\begin{cases}\infty & if\ T=T_m\\ 0 & others\end{cases} \tag{28}$$

where, δ(T-Tm) is the Dirac delta function.

Phase change occurs at a constant temperature for pure liquids. To approximate this process numerically, the slope method requires the definition of a finite temperature difference over which the phase change occurs. Without defining a small temperature difference, the specific heat determined from the enthalpy-temperature curve is infinite. To numerically implement the relationship shown above for the finite element technique, the following modification is made

$$C_{eqiv}=C_p(T)+L\delta^*(T-T_m,\Delta T) \tag{29}$$

$$\delta^*(T-T_m,\Delta T)=\begin{cases}\delta_l & if\ \ T_m\geq T\geq(T_m-\Delta T/2)\\ 0 & otherwise\end{cases} \tag{30}$$

where $\delta^*(T- T_m, \Delta T)$ is the modified Dirac delta function, has a large but finite value in the interval ΔT centered about T_m and is zero outside the interval. The interval ΔT is often referred to as the "mushy" zone and corresponds to the difference between the liquidus and solidus temperatures for the material. Through the use of this formulation for the specific heat the heat flux jump condition may be eliminated from the problem. This approach is a computationally effective approach since a two-region problem with a jump condition has been reduced to a single region problem with rapidly varying properties.

At the same time, the viscosity is modeled with a temperature dependence to allow for the change from a no-flow to a flow state. The viscosity of the melt is modeled as a fluid, while the viscosity of the solid material is infinite. To simulate it numerically the “slope” method is

employed here again. (See Figure 30) The viscosity is set to a large but finite value ($\mu\infty$) to prevent flow from occurring in the solidified material. It is recommended that the temperature range in which the value of the viscosity drops to fluid viscosity value be defined slightly above the temperature range in which latent heat is released. The result is the suppression of small convective effects that can destabilize the numerical solution.

$$\mu = \begin{cases} \mu_0 & if\ T < T_m \\ \mu_\infty & if\ T > T_m + \Delta T/2 \\ \mu = \mu_0 + \dfrac{2(\mu_\infty - \mu_0)}{\Delta T}(T - T_m) & \\ \qquad if\ \ (T_m + \Delta T/2) \geq T \geq T_m & \end{cases} \tag{31}$$

Conduction within the solid (crucible, unmelted feedstock, and so on) requires the solution of the conduction equation, which is shown below.

$$\rho_s C_p \frac{\partial T}{\partial t} = k \nabla^2 T \tag{32}$$

At the interface between the solid (unmelted feedstock) and the adjacent phase changing material the condition of energy conservation is required. The relationship governing the energy transfer across this interface is shown below.

$$k_{mt} \frac{\partial T_{mt}}{\partial n} = k_l \frac{\partial T_l}{\partial n} \tag{33}$$

At the interface between the solid (unmelted feedstock) and the liquid (molten feedstock) the conditions of equal temperatures between the interfaces and the heat transfer between the phases includes the latent heat release. These two relationships are shown below in equation form.

$$T_l = T_s \tag{34}$$

$$k_l \frac{\partial T_l}{\partial n*} - k_s \frac{\partial T_s}{\partial n*} = \rho_s L u* \tag{35}$$

3.4.3. Casting Process

The fluid is considered to be incompressible, have constant thermal properties, and is a Newtonian fluid. These assumptions lead to the governing equations for the transient analyses of the melting of the phase change material to include the continuity equation, the Navier-Stokes (momentum) equations, and the energy equation. These equations are shown in tensor notation as Equation (36-38). [15-18, 48]

$$\nabla \bullet \vec{u} = 0 \tag{36}$$

$$\rho \frac{\partial \vec{u}}{\partial t} + \rho(\vec{u} \cdot \nabla)\vec{u} = -\nabla \hat{p} + \mu \nabla^2 \vec{u} \tag{37}$$

$$\rho C_p \frac{\partial T}{\partial t} + \rho C_p \vec{u} \bullet \nabla T = k \nabla^2 T \tag{38}$$

At the interface between the solid (the solidified metal) and the liquid (the molten metal) the conditions of equal temperature and the heat transfer between the phases includes the latent heat release. These equations for the two relationships are the same as Equations (34) and (35).

The condition of a no-slip velocity within the liquid phase is also imposed.

Phase change (solidification) was modeled through the use of the "slope" method within FIDAP. [47] This is the reverse process of the melting process as above. (See Figure 30) Again, a modified specific heat equation is employed. (Same as Equation 25-31) The use of this "artificial" specific heat allows for the correct amount of energy removal to occur from an element before it is considered to be a solid. Physically, the total energy transfer required for solidification is correct. With adequate mesh and small time steps (VOF forces this to occur) this method is accurate. [49,50]

Again, a "slope" method is employed for the viscosity in the solidification. Here, the viscosity of the molten is modeled as a fluid, while the viscosity of the solidified material is infinite and is set to a large but finite value ($\mu\infty$) numerically.

Conduction within the solid (mold, solidified metal, and so on) required the solution of the conduction equation as Equation (32).

At the interface between the solid (metal) and the adjacent phase changing material the conditions of energy conservation is required. The interface temperature does not have to match identically because a convective heat transfer relationship is used to model the interface between the melt and the mold. This technique is commonly used in casting analyses.

The interface between the melt and solidified material must meet the requirement of energy conservation as well. The relationship governing the energy transfer across this interface is shown in Equation (33).

3.5 VOF and Non-VOF Modeling Approaches

For simulating the "pure" filling process and casting process (VOF-solidification process) with the free surface the technique of Volume of Fluid (VOF) method is used whereas for simulating the "pure" solidification process the Non-VOF model is employed in FIDAP. In the VOF approach the fluid moves through a fixed mesh instead of having the mesh moved with the melt. [49,50] Figure 31 shows the Non-VOF approach and the VOF approach for modeling:

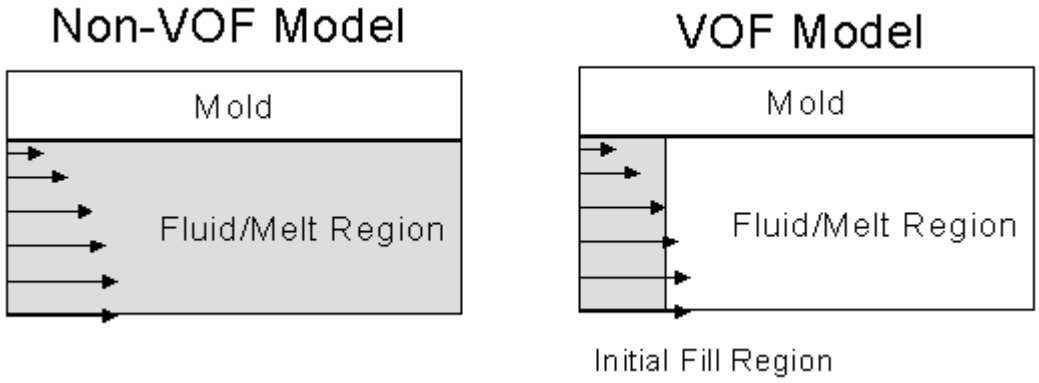

Figure 31 - The Non-VOF model and the VOF model

Through VOF approach the flow of the melt into the fuel rod region is modeled. Hence, an indicator function F is introduced to represent the fluid volume, which moves with the fluid. Thus the advection is governed by this function:

$$\frac{\partial F}{\partial t} + \bar{V} \cdot \vec{\nabla} F = 0 \tag{39}$$

The sharp interfaces are maintained by ensuring a sharp gradient of F. The value of this function is 1 when the cell of the meshing volume is filled and is equal to 0 when this cell is emptied. A steep gradient of F represents a free surface location.

$$F(\vec{x},t) = \begin{cases} 1 & Fluid \\ 0 & Void \end{cases} \tag{40}$$

The function F can be discretized, for element i, as follows:

$$f_i = \frac{1}{V_i} \int F dV_i \tag{41}$$

The limits of integration are restricted to the volume of an element V_i. The value of f_i corresponds to a filled state, an emptied state, or fractional filled state. Thus f_i varies between 0 and 1. An element whose $f_i = 1$ is referred to as a filled element. An emptied element is denoted by $f_i = 0$. The value of f_i between 0 and 1 means a fractional fill or a free surface.

Figure 32 shows the single-fluid scenario and the two-fluid scenario of the VOF approach. In the single-fluid scenario both the fluid and the void contact a solid region, i.e. the wall of the mold. A melt-mold interfacial heat transfer coefficient is specified along the interface of the solid and fluid regions. The value of the coefficient is a specified value and is automatically defined to zero between the void and the solid (mold), because there is no heat transfer to the void region. However, in the two-fluid scenario there is another fluid, for example, the air instead of the void. Thus, another nonzero heart transfer coefficient is employed to simulating the convection heat transfer between fluid B and the mold.

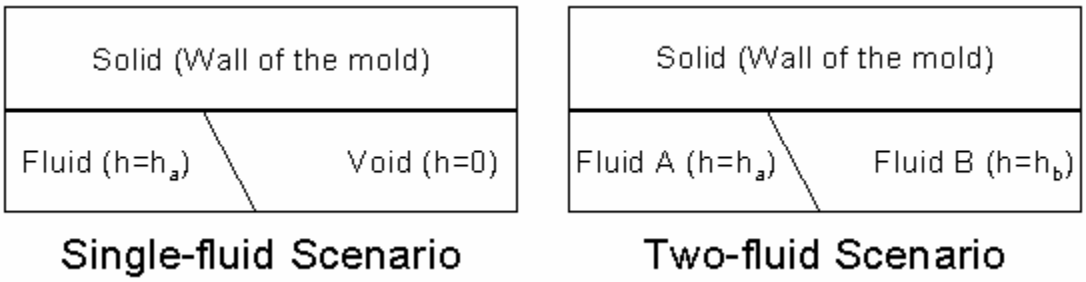

Figure 32 - The single-fluid scenario and the two-fluid scenario

3.6 FIDAP and the Simulation Scheme

The problem will be analyzed numerically through the use of the commercial finite element package FIDAP™ (Fluid Dynamics Analysis Package), which is based on the finite element method (FEM). This package is a general-purpose heat transfer and fluid mechanics code.

The finite element method is a well-known numerical method. The interesting aspect of the finite element method is that the problem formulation results in a system of simultaneous algebraic equations instead of a system of differential equations. This is because a system or a body is modeled by subdividing into smaller elements. Finite element analysis involves the following steps:

- Specify the geometry and divide domain into finite elements (small local regions where the governing equations are approximated)

- Formulate the properties of each element and determine the node properties using known information
- Assemble elements to obtain the finite element model of the domain
- Apply the known values – boundary and initial condition.
- Specify how the domain is affected by the known nodes
- Solve simultaneous linear algebraic equations to determine node transport properties (temperature, velocity, pressure, etc.)

The power of the finite element method resides principally in its versatility. The method can be applied to various physical problems. The body analyzed can have arbitrary initial and boundary conditions. The mesh can mix elements of different types, shapes, and physical properties. This great versatility is contained within a single computer program. User-prepared input data controls the selection of problem type, geometry, boundary conditions, and element selection. Another attractive feature of finite elements is the close physical resemblance between the actual system and its finite element model.

The finite element method also has disadvantages. A computer, a reliable program, and intelligent use are essential. A general-purpose program has extensive documentation, which cannot be ignored. Experience and good engineering judgment are needed in order to define a good model. Many input data are required and voluminous output must be stored and understood.

An iterative solution technique for a FEM solver was employed to solve the set of equations sequentially and separately for each active degree of freedom. This approach is referred to as a segregated solver. This method is used because it substantially reduces the memory requirement compared to the other solvers used, such as the fully coupled method. FIDAP uses the VOF (Volume of Fluid) technique to model transient flows involving free surfaces of arbitrary shape. The capabilities constitute a powerful tool in simulating complex free surface deformations including folding and breakup.

FIDAP was used to solve the fluid and heat flow inside the molds. A “mapped” type mesh was used to discretize the geometry. The general purpose pre-processor GAMBIT^{TM} was used for the mesh generation.

A mapped mesh is a regular “checkerboard” mesh for surface areas that are typically used for more regular geometries. The complete finite element mesh for the heat transfer problem was constructed from a collection of mapped mesh areas. This technique is not automatic, as the geometry must be decomposed into regions that are suited to a mapped mesh.

A backward Euler (implicit) scheme was used to solve the three transient equations. Segregated iterative method was used to obtain the solution at each time step using fixed time step. Although one can generally obtain high order accuracy, when convection is strong compared to the diffusion and sharp gradients of the flow variables are encountered in the computational grid, unstable results are likely to occur. Streamline upwinding is used to stabilize the oscillations in the computations.

There are two general approaches that could be used to model the flow of the molten material into the melt. The first is to move the mesh with the melt. This approach requires the mesh to be continually recalculated and it requires a technique to couple the heat transfer to the solid. The second choice is to have the fluid move through a fixed mesh. This latter technique is the approach FIDAP uses is Volume of Fluid (VOF) method and it is discussed in section 3.4.

4. Results and Discussions

4.1 Induction Melting Process

In the first simple model, the values of C (species 1 in FIDAP) and S (species 2 in FIDAP) solved from FIDAP are shown as Figures 33 and 34, respectively. The Surface plots of C and S are shown in Figures 35 and 36:

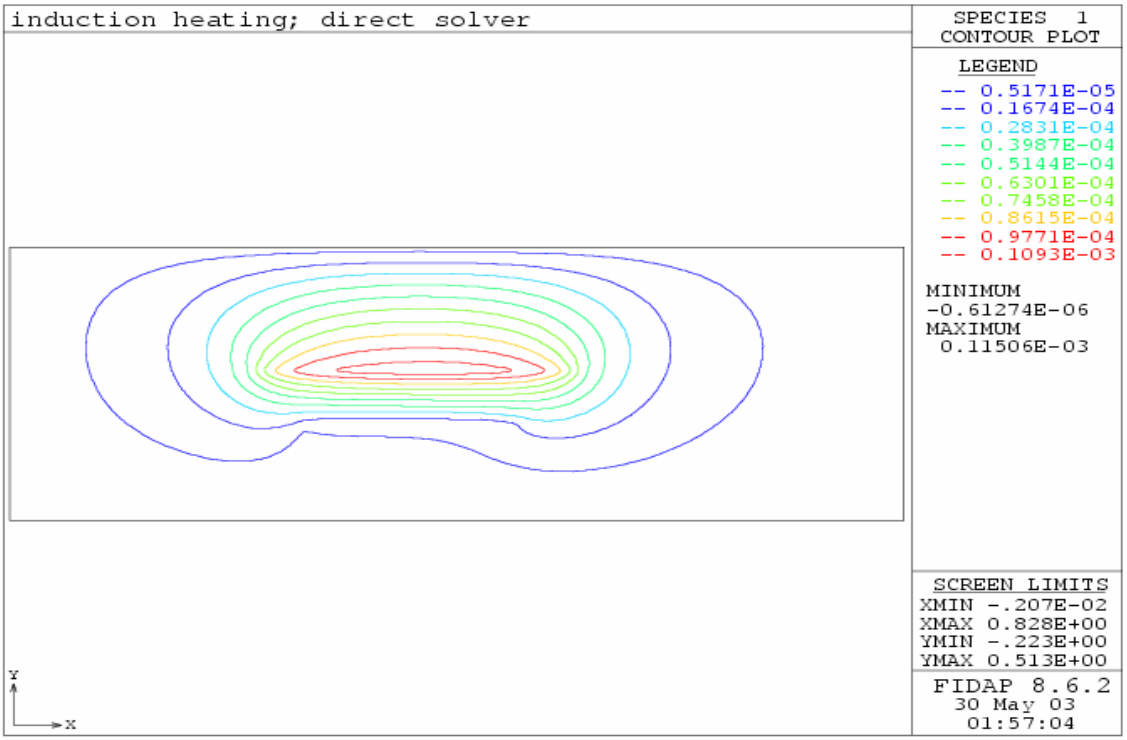

Figure 33 - The value of C (species 1 in FIDAP).

It can be found that the value of C variable and S variable are lager at the crucible or coil regions. The results indicate that the variable C is highest in the coil region, while the variable S is highest in the crucible region (a conductor). The sharp gradients exist around the coils and the "skin" of the conductor in the system. These results tally with the conclusion of Gresho and Derby [41, 44-46].

For the second system (see Figure 14), the values of C (species 1 in FIDAP) and S (species 2 in FIDAP) solved from FIDAP are shown as Figures 37 and 38 respectively:

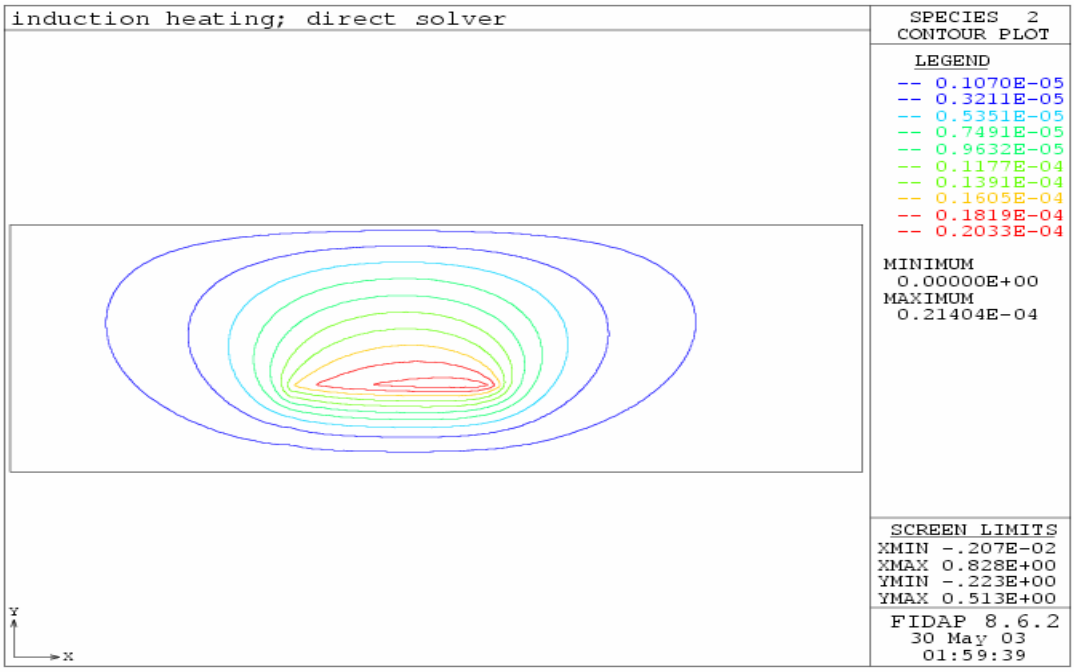

Figure 34 - The value of S (species 2 in FIDAP).

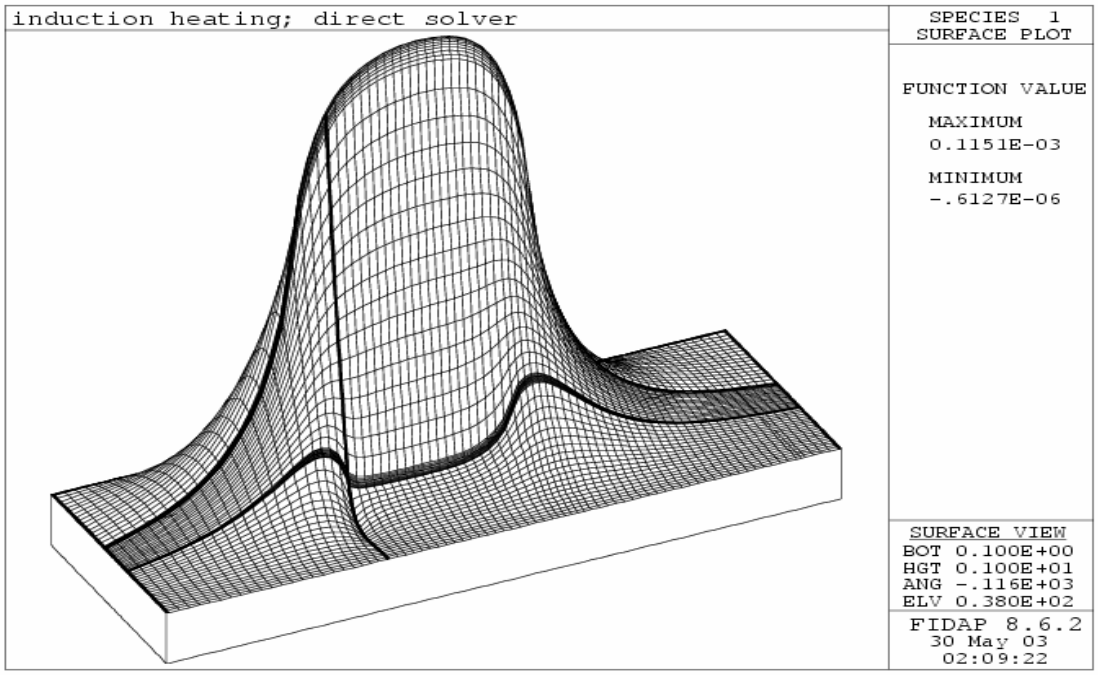

Figure 35 - Surface plots of the value of C (species 1 in FIDAP).

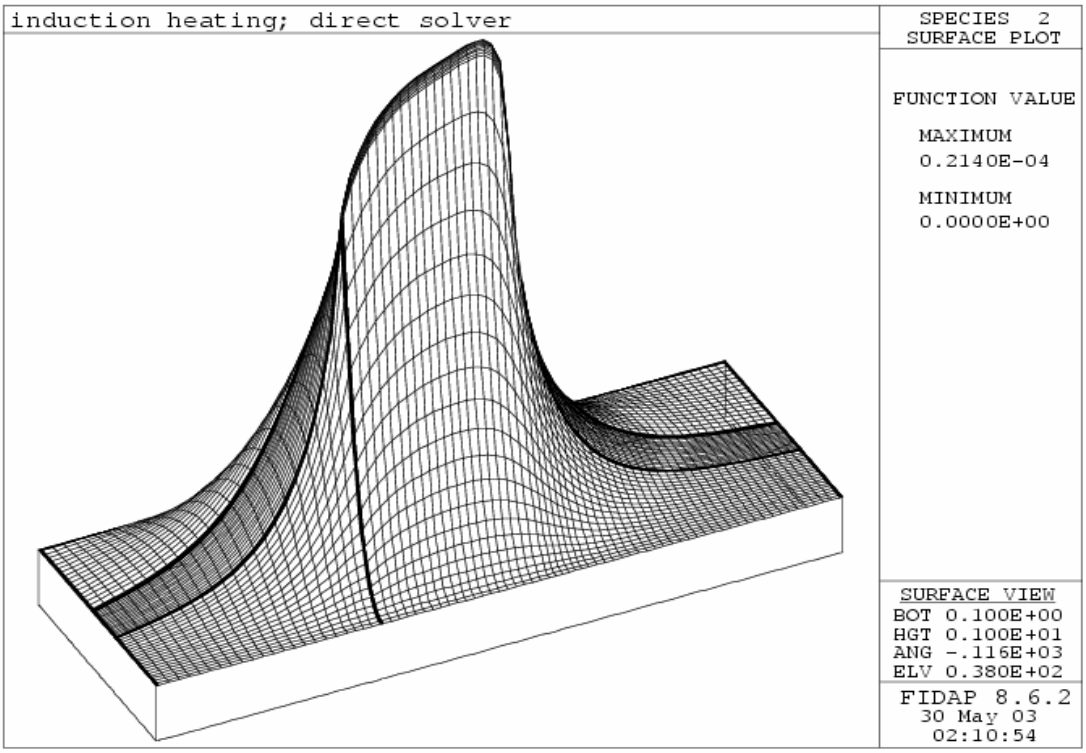

Figure 36 - Surface plots of the value of s (species 2 in FIDAP).

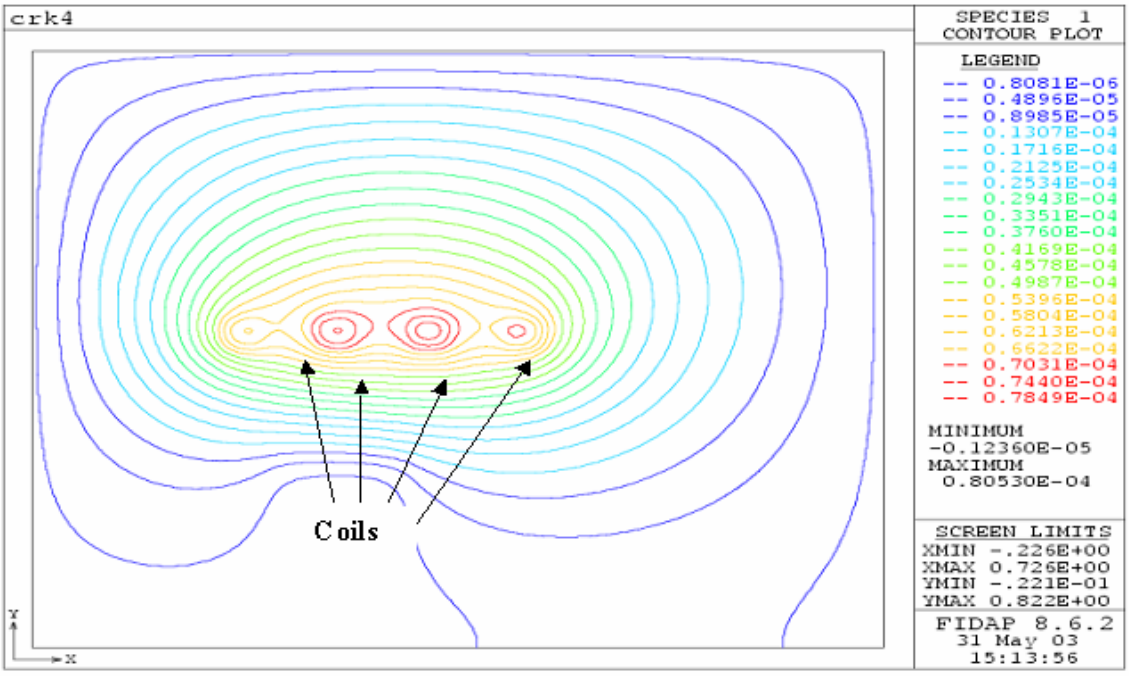

Figure 37 - The value of C (species 1 in FIDAP).

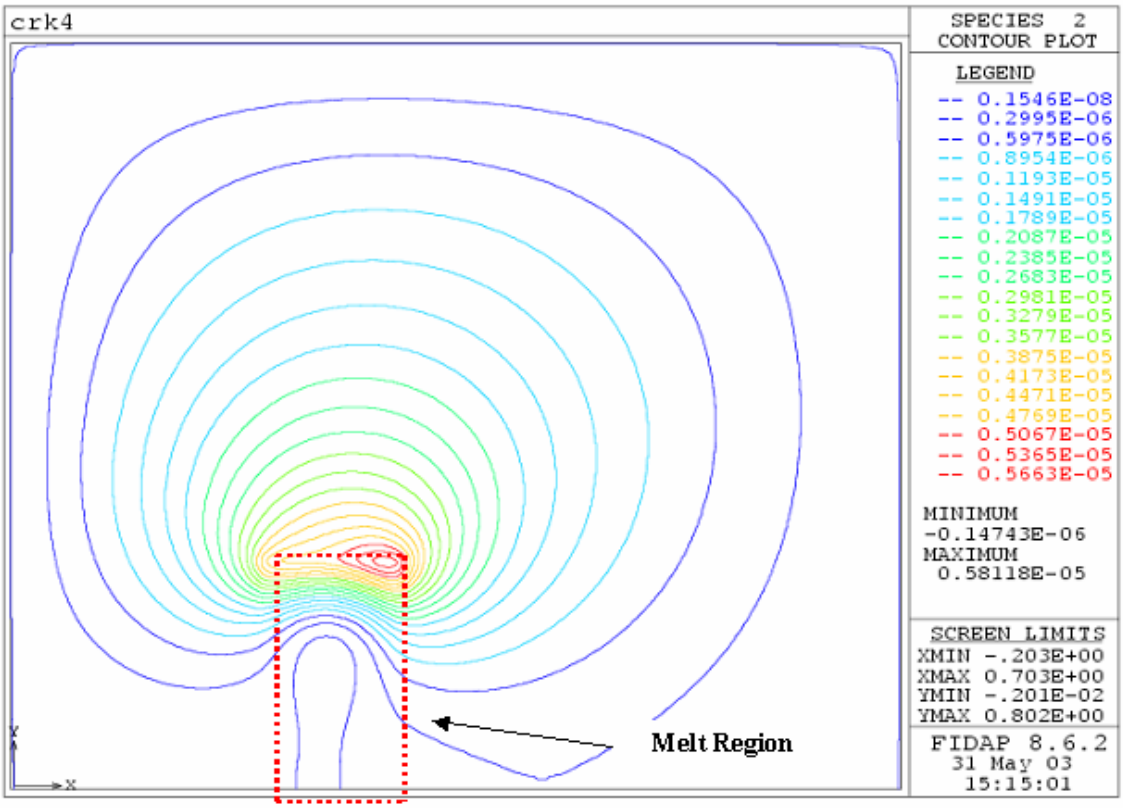

Figure 38 - The value of C (species 1 in FIDAP).

The Surface plots of C and S are shown in Figures 39 and 40:

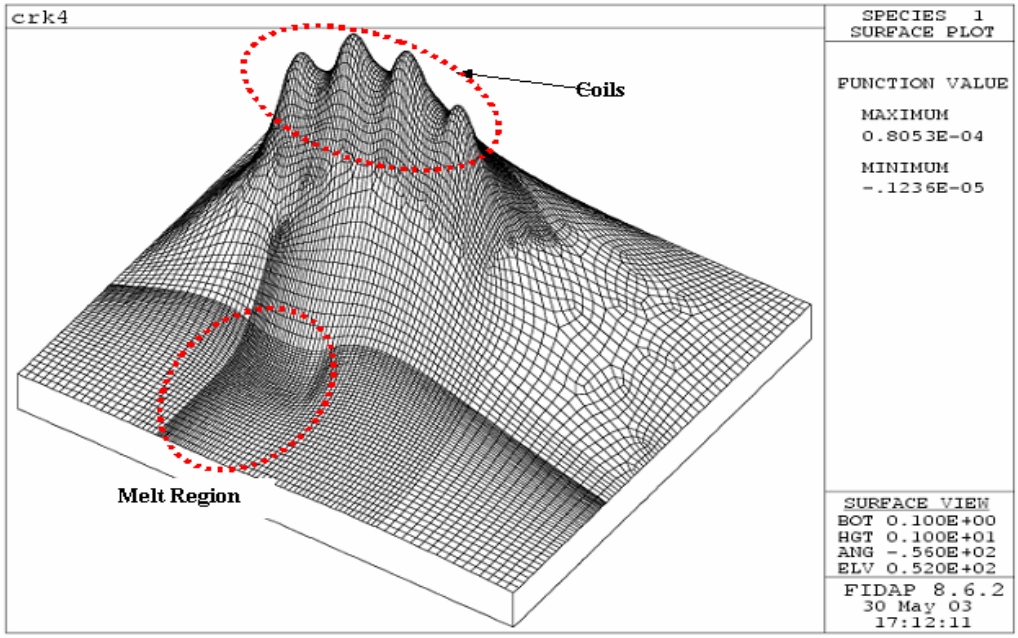

Figure 39 - Surface plots of the value of C (species 1 in FIDAP).

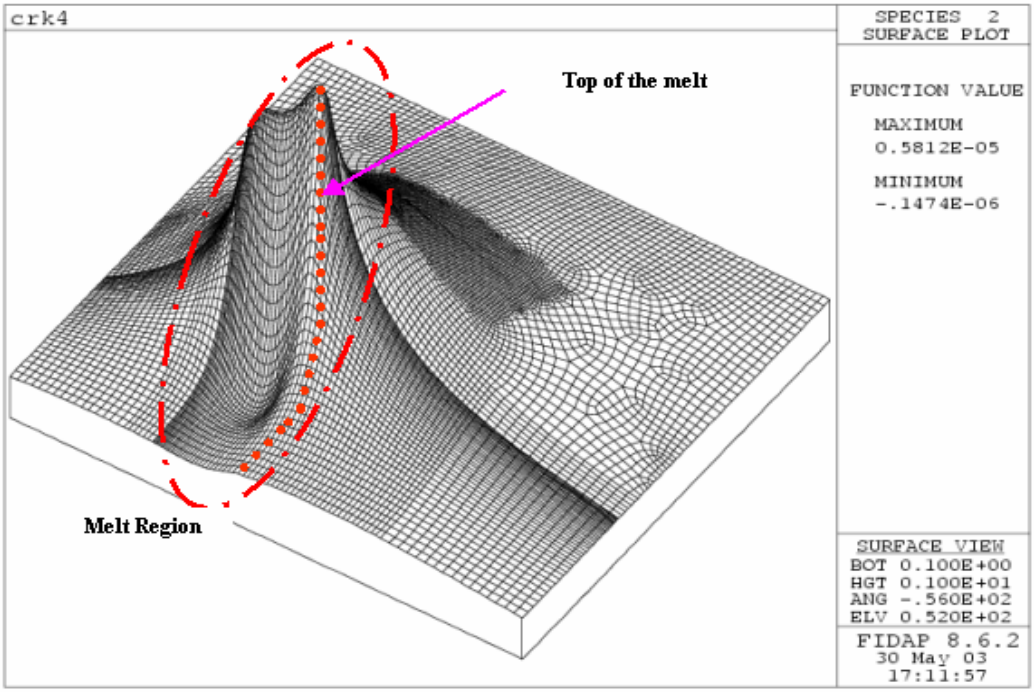

Figure 40 - Surface plots of the value of s (species 2 in FIDAP).

In this case, the same conclusion of the value of C variable and S variable can be drawn, i.e. the maximum value of C occurs near the coil regions whereas the variable S is highest in the melt region (a conductor). Since in this system, a "segregated-structure" crucible is used the "skin" effect occurs in the feedstock region ("melt"). The sharp gradients exist around the coils and the "skin" of the feedstock in the system.

From the calculation of the simple model and the second system, we can find that FIDAP is suitable for the calculation of induction heating problem. However, there is no feedstock in the crucible. This simple system is a good example for indirect induction heating process, especially for some non-conductor material. The non-conductor feedstock can absorb energy from the heated crucible. The temperature of the feedstock increases very slowly in the second system. The reason for this low efficiency is that the relatively small coil area.

So the next step, we continued our simulation by choosing another benchmark system (Gross' model). Typical numerical results are presented below. For Gross' model, Figure 41 shows contours of the field variable C. The variable C has its peak values in the coil region, which relates to the source term associated with this region (see Equation (13)). The contours of the center coil are slightly higher than others and the two end coils are lowest. The surface plot of C clearly shows how it is only high within the coil region itself, dropping off rapidly in the other locations. The plots for the second field variable, S, are shown in Figure 42. However, the peak value occurs near the top and outer edge of the melt region. This is the region where skin heating will occur as a result of the coupling of the fields.

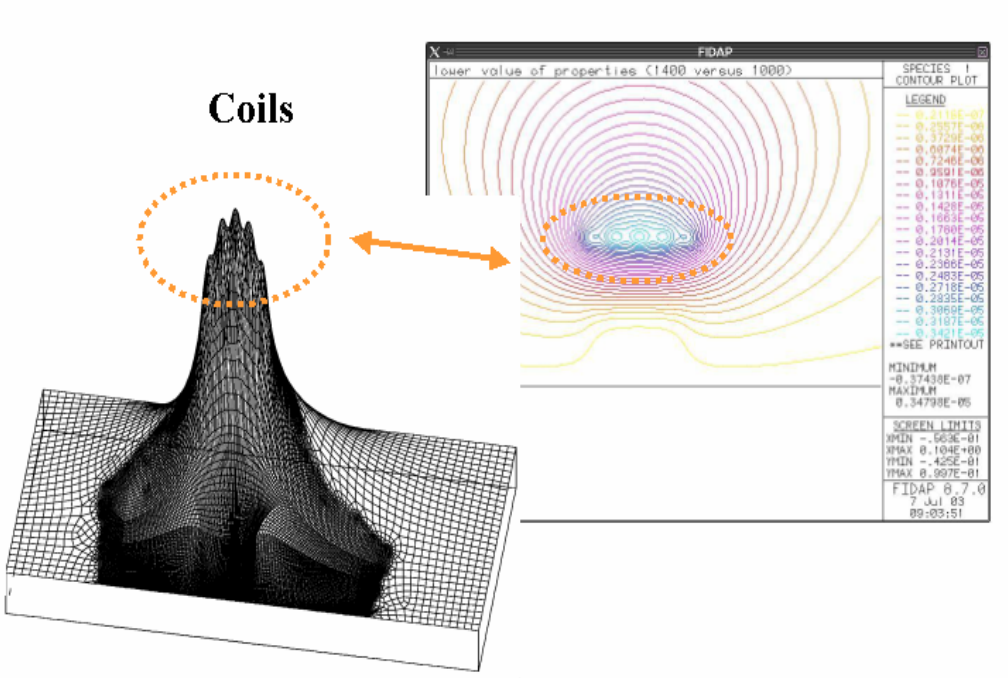

Figure 41 - Contour plot and surface plot of the field variable C in the induction field. Each peak resides at the location of a coil of the induction coil.

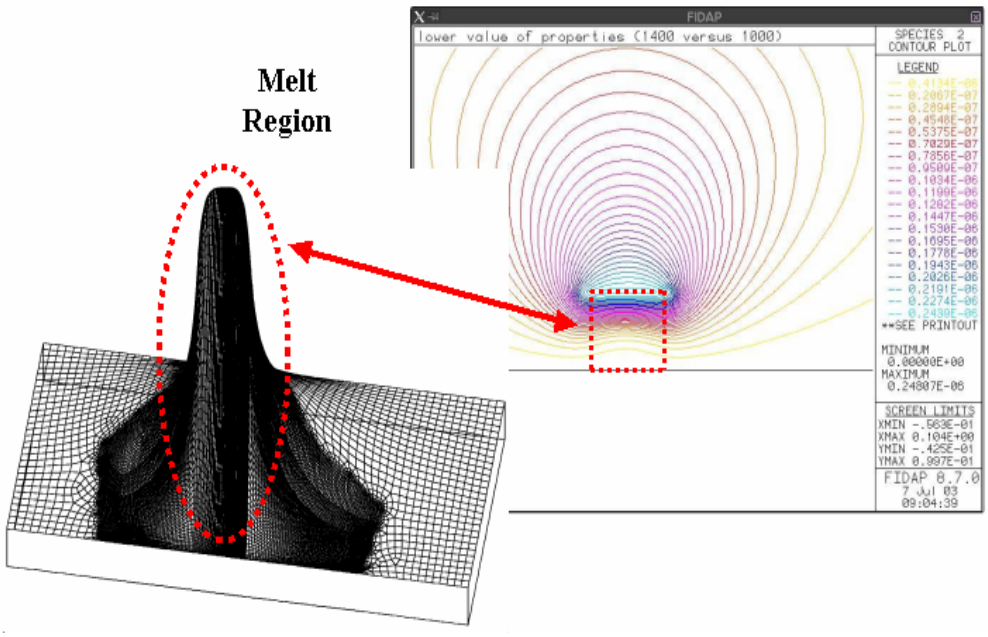

Figure 42 - Contour plot and surface plot of field variable S in the induction field. Peak occurs near the top edge of the melt region.

The radial profile of time average power deposition rate at one location within feedstock region is shown in Figure 43. This distribution is typical for a surface heating effect. The vertical line in Figure 43 represents the skin heating depth, as defined within that figure.

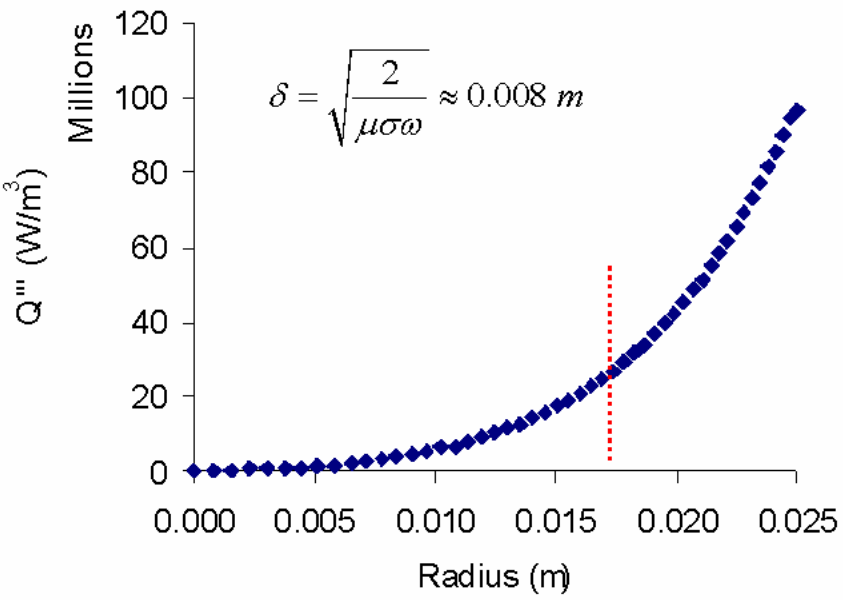

Figure 43 - The radial profile of time average power deposition rate at one location within "melt" region

The second step in simulating Gross' system is to input the time average power deposition as a source term to simulate the heat transfer process in the furnace. Figure 44 shows the temperature contour at time t=400s. From this plot we can see the temperature is much lower along the inner side of the crucible than the maximum temperature due to the heat sink set on the outer surface of the crucible. This will lead to the formation of the "skull" and the molten region will develop towards the center of the feedstock. Figure 44 shows the radial profile of temperature distribution of the melt region for different time step. Figures 45 and 46 show the melting process and the "skull" formation.

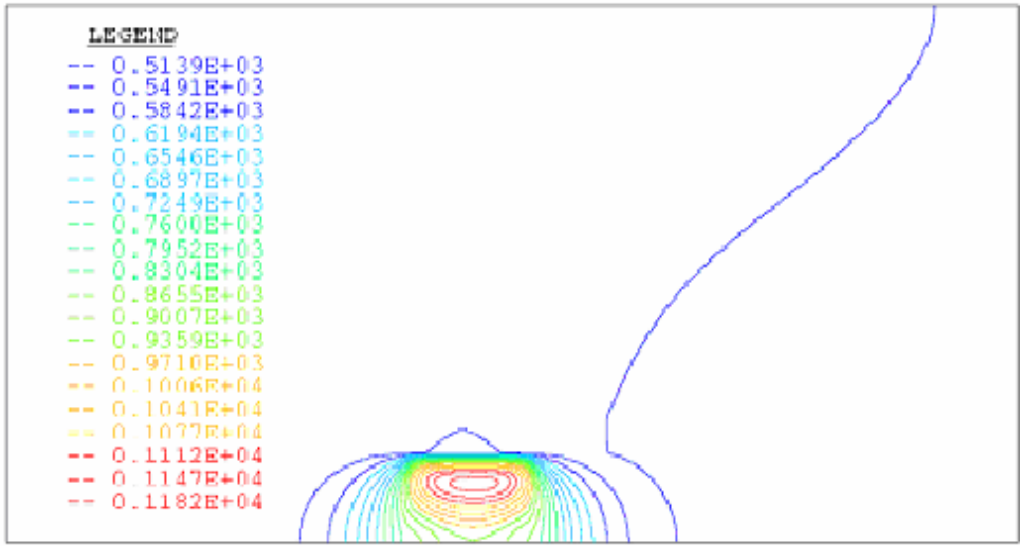

Figure 44 - The temperature distribution at time t=400s

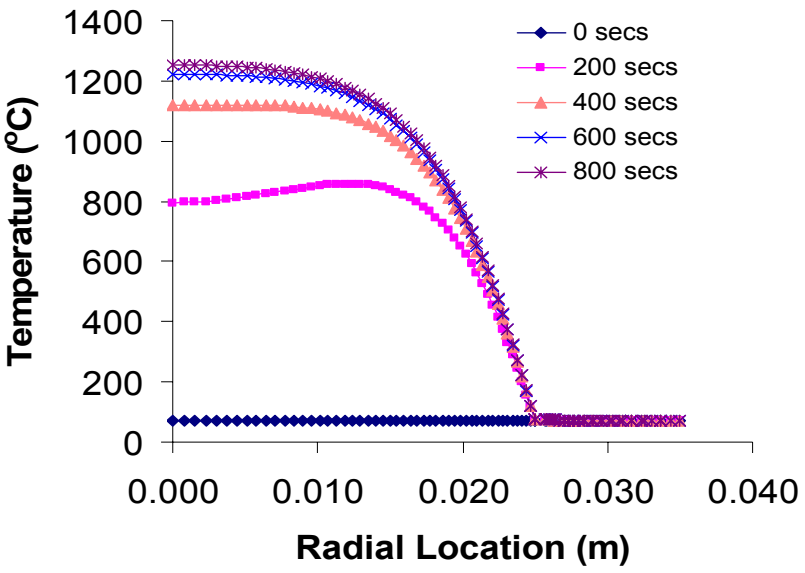

Figure 45 - The radial profile of temperature distribution

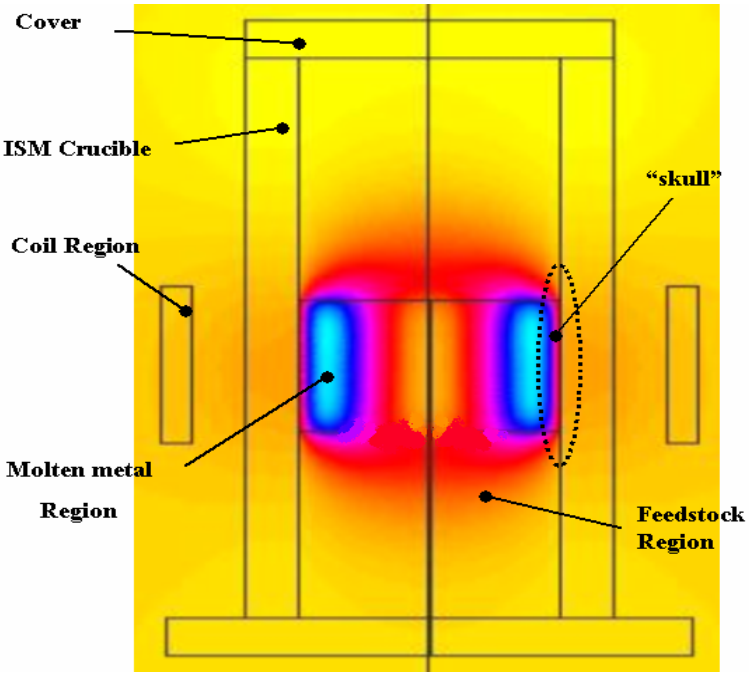

Figure 46 - Melting process and the "skull" formation

Now let us examine the impact of the important dimensions of the system. To compare with the former result, a smaller value d=2 mm and b=5 mm are studied (d_0 =3 mm, b_0= 10 mm). (See Figure 18)

From the plots above, we can see that for a smaller distance between the coils' surfaces (d=2 mm), the metal can be heated to the melting point in almost half time of the case of d_0=3 mm. For the same feedstock volume, the smaller the distance between the coils, the faster the feedstock is heated. Similarly, to decrease the distance between the coils and the crucible from b_0=10 mm to 5 mm can also greatly improve the induction heating effect. Thus, the location of the coils has very large influence on the induction heating process. Consequently, we need to make the coils as closer as possible to each other and to the outer surface of the crucible in order to get higher heat efficiency.

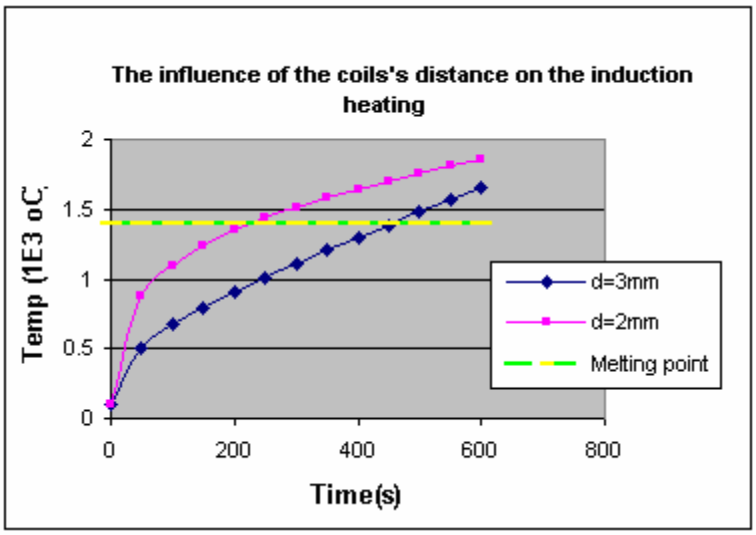

Figure 47 - The maximum temperature for different d values at b=10 mm

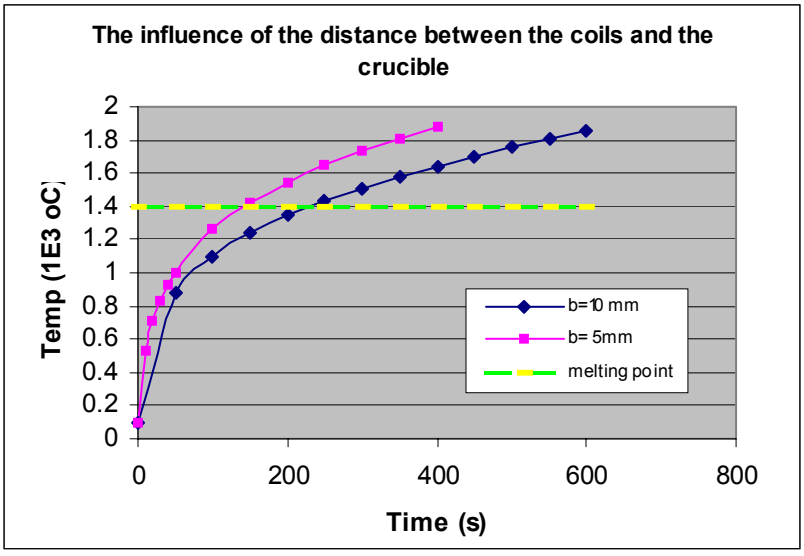

Figure 48 - The maximum temperature for different b values at d=2 mm

The coils' group number is changed from 5 to 6 in order to examine its influence on the induction process without changing any of the dimensions in the model. The result outputted

from FIDAP is shown in Figure 49. Obviously, the more the coils' turn number, the better the heat effect, especially at the beginning period of the process.

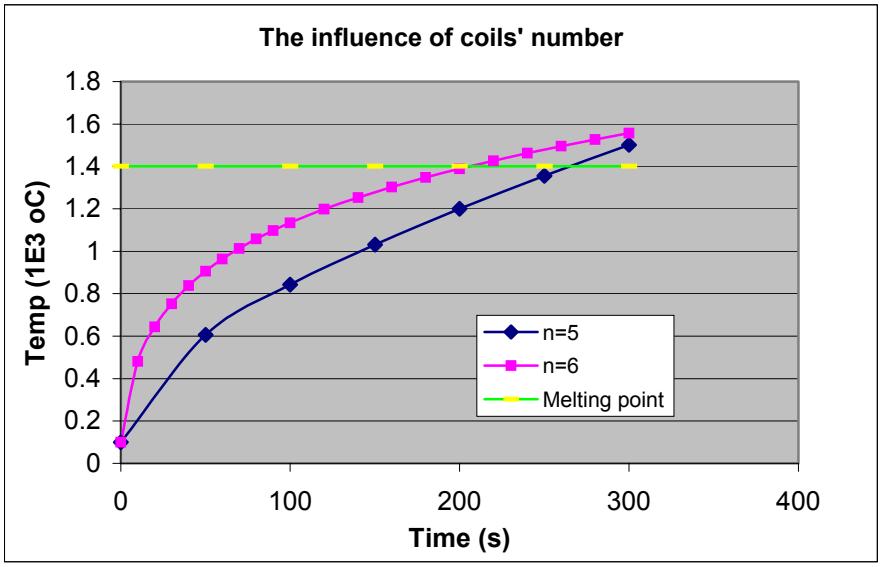

Figure 49 - The impact of coils' number on the induction heating process

If the dimensions of d and b, (see Figure 18), are decreased to 2 mm and 5 mm respectively and the coils' number is added from 5 to 6 at the same time, this modified design has very high heat efficiency (the temperature increases almost 3 times faster to the melting point) comparing to the original design as shown in Figure 50. From this calculation, we can draw a conclusion that we can optimize the induction heating process by modifying the design of the system.

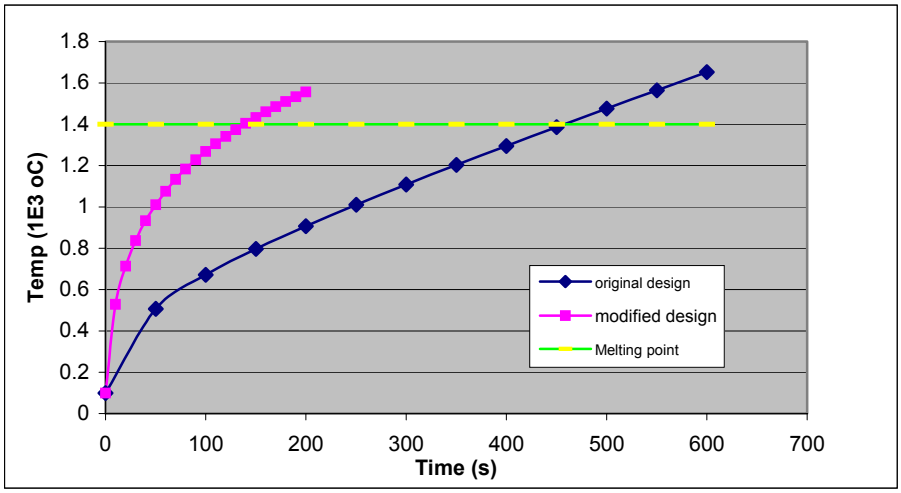

Figure 50 - The original design and the modified design of the induction heating process (Original: d_0=3 mm, b_0=10 mm, n=5; modified: d=2 mm, b=5 mm, n=6)

This model has shown the ability to calculate the induction-heating field for typical geometries (coil, crucible, melt). Rapid heating is typically experienced in the region indicated by the high fluxes, resulting in the melting of the material within the ISM. And the "skin effect" was observed and finally a "skull" was formed due to the presence of the cooling system. These conclusions coincide with the theoretical analysis and the numerical and experimental results.

The typical results of ANL's system are shown in Figures 51-54. The C and S results coincide with the theoretical analysis and the former simulation for Gross's system, i.e., C has high values around the coils and S has a high value along the edge of the feedstock.

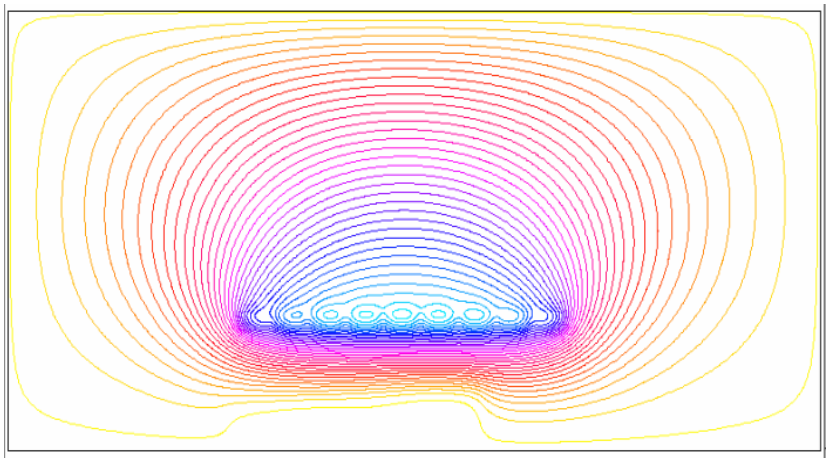

Figure 51 - Contour plot of the field variable C in the induction field (n=9, f=225 Hz, I=500A)

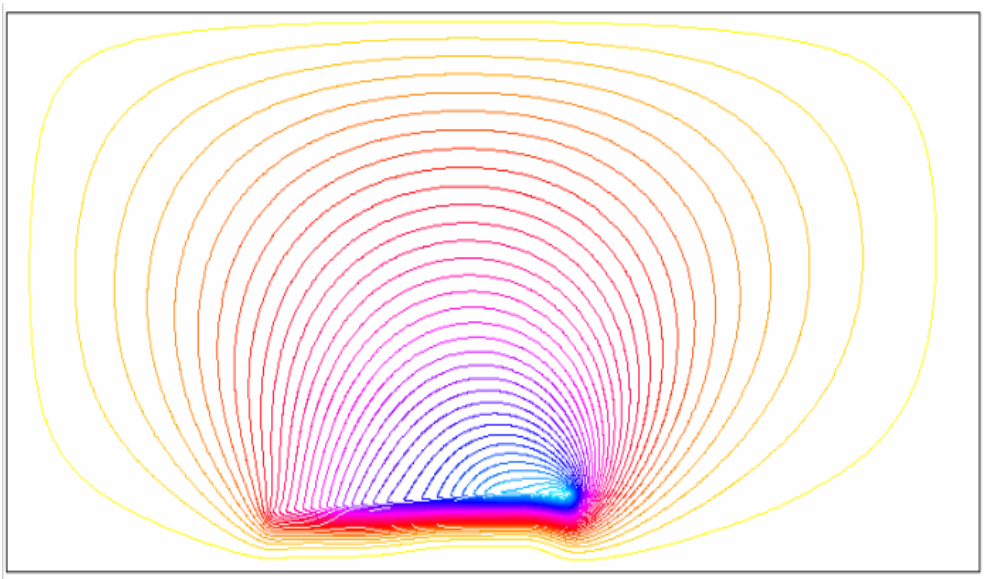

Figure 52 - Contour plot of the field variable S in the induction field (n=9, f=225 Hz, I=500A)

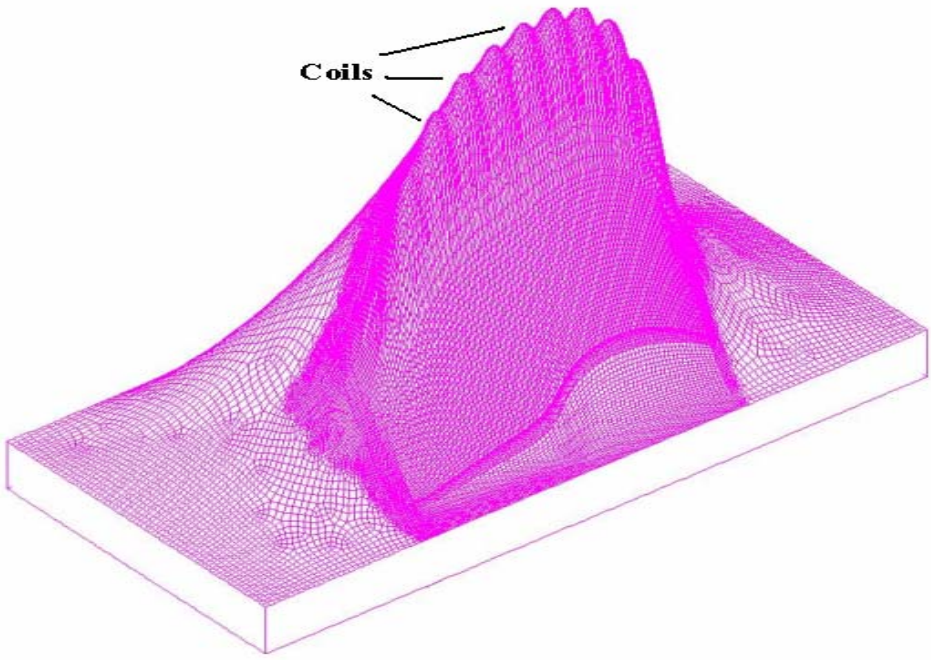

Figure 53 - Surface plot of C in the induction field (n=9, f=225 Hz, I=500A)

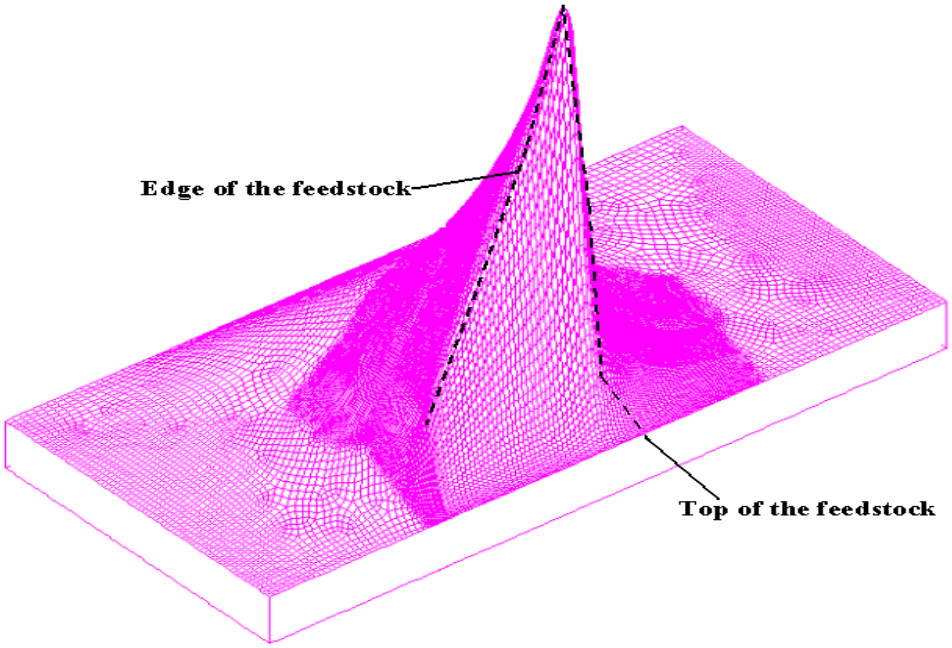

Figure 54 - Surface plot of S in the induction field (n=9, f=225 Hz, I=500A)

The 2-D and 3-D plots of the time average power deposition ($\dot{Q}'''$) are calculated by a Fortran subroutine we compiled and then output from a graphics postprocessor software Tecplot. It is shown as Figures 55-56. It accords with the analysis above that the maximum value of time lies in the "skin" and the top of the feedstock. The value of the time average power deposition

($\dot{Q}'''$) decreases quickly and approaches to zero near the center of the metal feedstock. And the $\dot{Q}'''$ value increases and reaches to the maximum value on the top of the region in x direction. The smaller the x value is, i.e. the closer it is located to the inner surface of the crucible; the faster the $\dot{Q}'''$ value increases as shown in Figure 57.

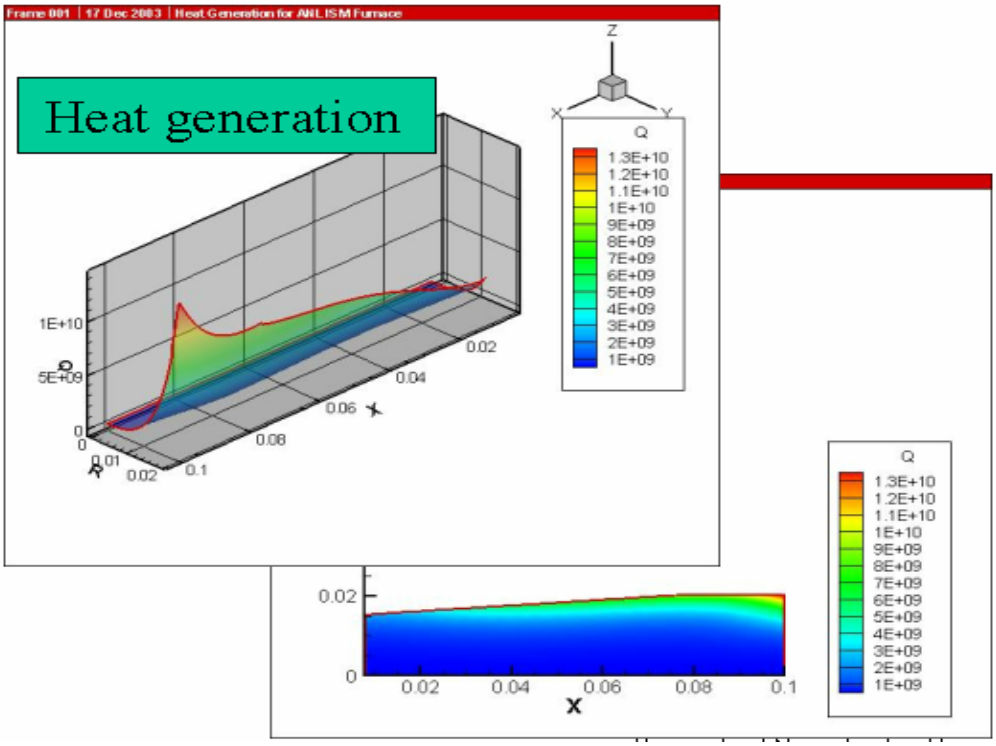

Figure 55 - 2-D and 3-D view of the time average power deposition (x (m), Q (w/m³))

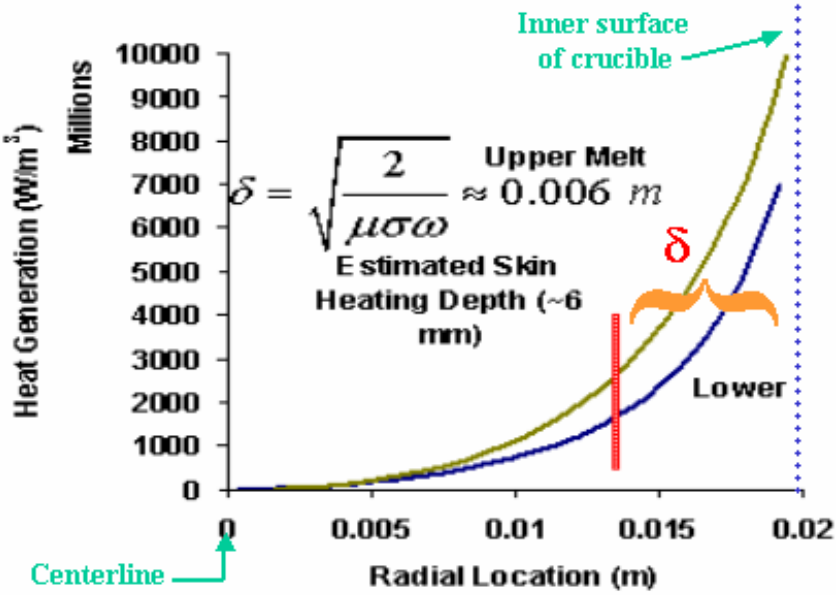

Figure 56 - Time average power deposition in the r-direction

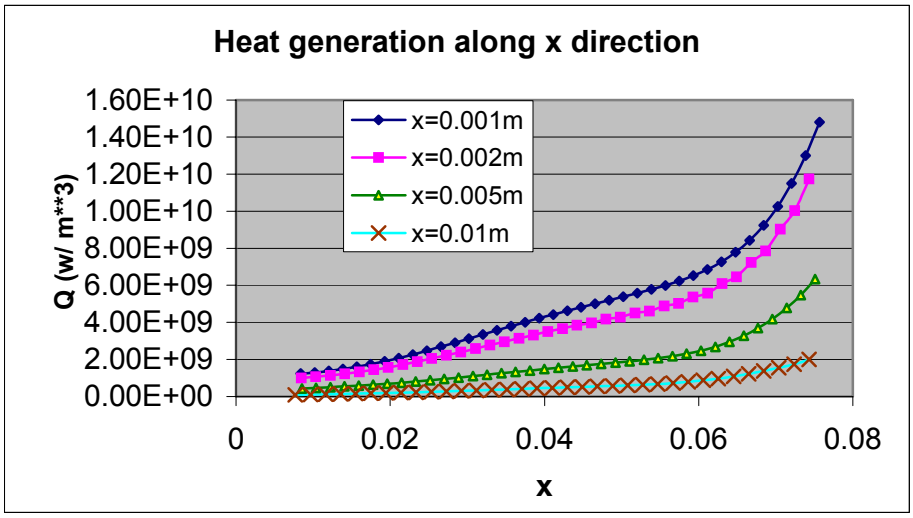

Figure 57 - Time average power deposition in x-direction for different location (x is the distance to the skin)

Later we also studied the impact of the current and the frequency of the alternative current on the induction heating process by employing different values in the simulation.

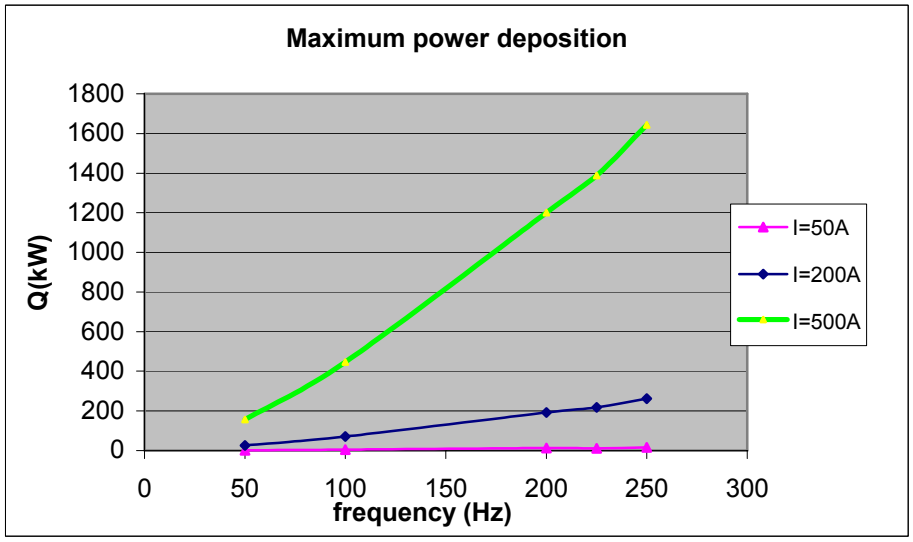

Figure 58 - Comparison of maximum value of power deposition for different current values

Comparison for different frequency value:

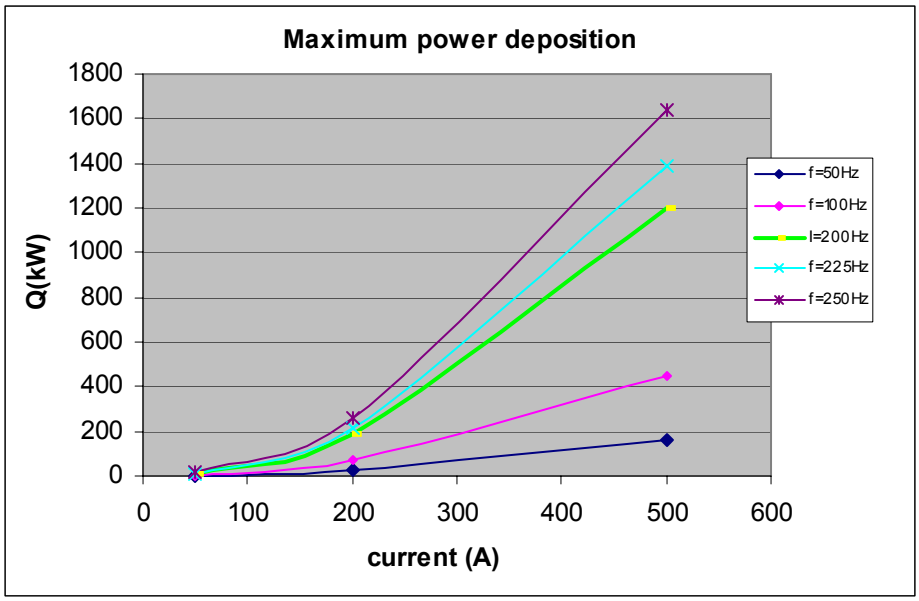

Figure 59 - Comparison of maximum value of power deposition for different current frequencies

From Figures 58 and 59 we can see that the maximum value of the induction heating power deposition keeps increasing with the current value or current density and the current frequency. Hence, we can draw a conclusion that the current value and the current frequency have a relatively larger impact on the induction heating process. It is also easy to understand directly from equations (13-19).

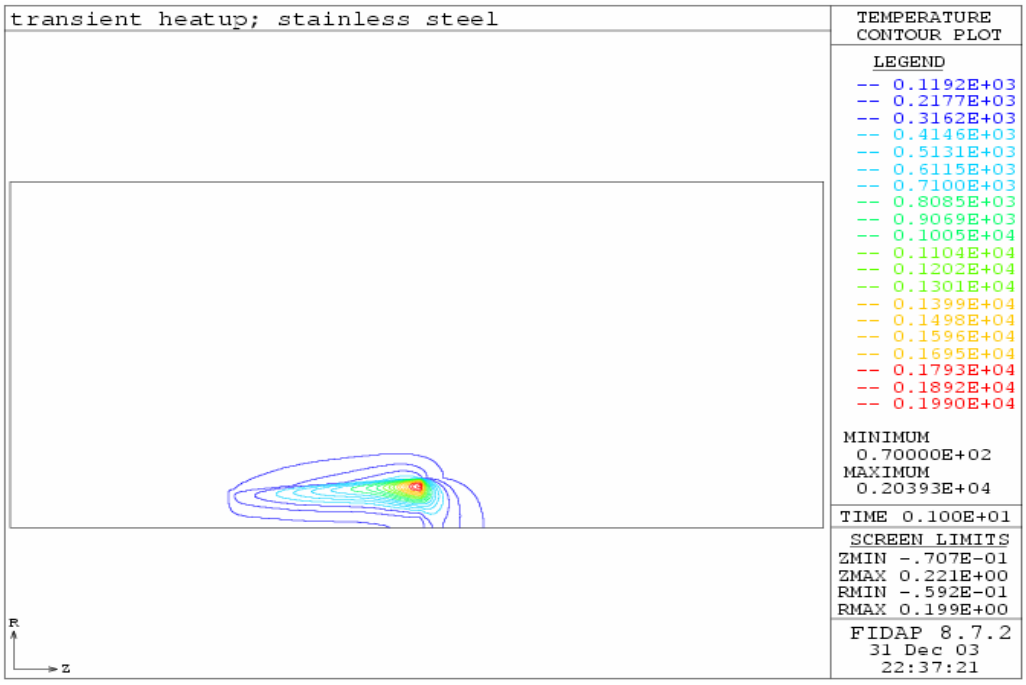

Figure 60 - Temperature distribution for ANL's system (n=9, f=6400 Hz, P=50% Pout)

Figure 60 shows the temperature distribution after inputting the time average power deposition as a source for heat transferred calculation. We obtained the similar time contour as in the simulation of Gross' model, i.e. a lower temperature exists along the inner surface and a skull is formed.

At the same time, the feedstock is heated up quickly and then is molten. The melt region develops fast towards the center of the feedstock during the continuous heat process. Since the induction heating has a very high efficiency the maximum temperature increases very fast before the heat was transfer to the close region from the hottest region. Although the maximum temperature increases at an incredible speed in the case of high power supply, we can observe from the below plot that the melt region develops at a reasonable speed towards the center of the feedstock during the continuous heat process. A big volume of melt was formed in 6 seconds and the "skull" remains unmolten along the crucible.

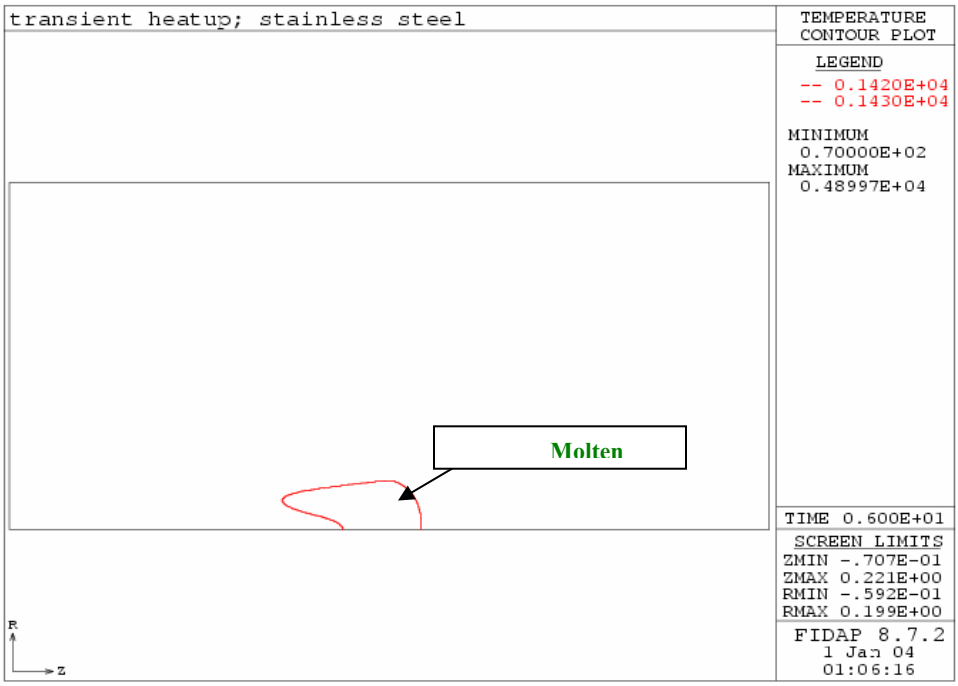

Figure 61 - The melting effect in the feedstock (t=6s, n=9, f=6400 Hz, P=50% Pout)

In ANL's experiment, 50% power is employed in the induction heating process for stainless steel. The 100% power is 150 kW. The frequency (f) is 6400 Hz in the experiment. Five different cases are simulated with power output rates varying from 10% to 50% in order to check their influence on the induction heating process in ANL's system. Figure 62 shows the maximum temperature for different power supply. The maximum temperature reaches 3000 ^{o}C in 2 seconds if 50% Pout is employed. On the other side, if a lower power supply is employed, it takes a long time or forever (for example, 10% Pout) to reach the melting point of the feedstock.

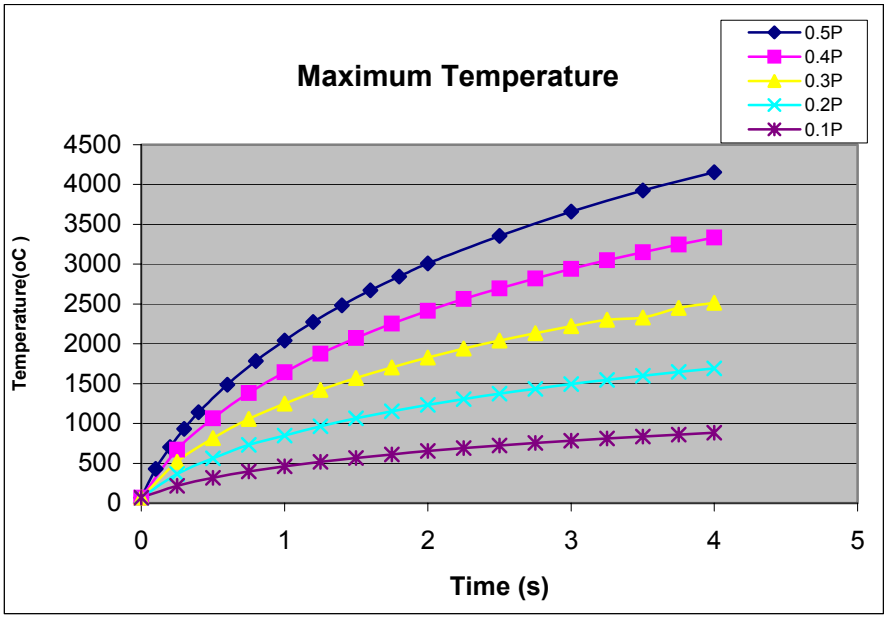

Figure 62 - The maximum temperature in the feedstock for different power supply values (n=9, f=6400 Hz, Pout=150 kW)

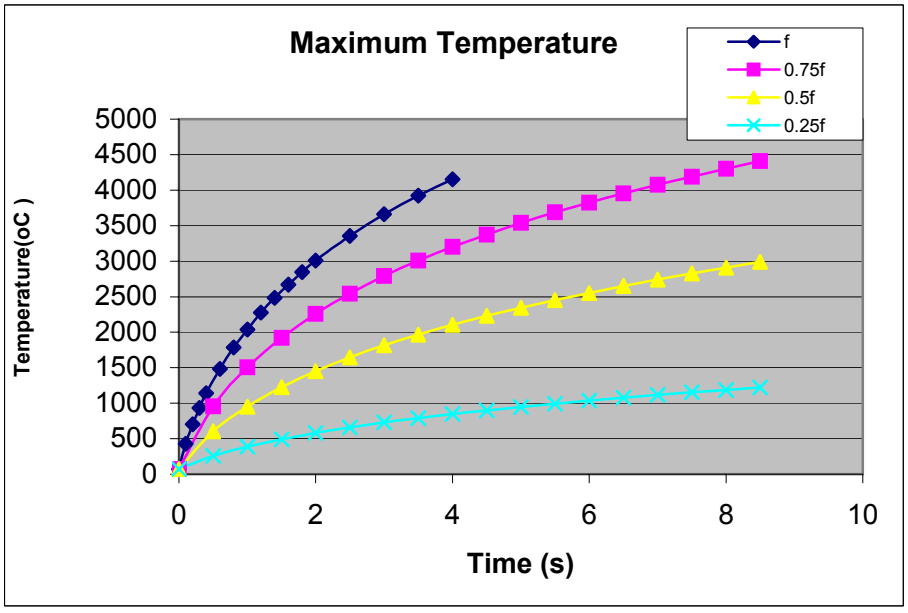

Figure 63 - The maximum temperature in the feedstock for different frequencies (n=9, f=6400 Hz, P=75 kW)

Four different cases of 100% f, 75% f, 50% f, and 25% f are simulated in order to check the influence of the frequency. Figure 63 shows the comparison of maximum temperature for different frequency values. It is obvious that the frequency of the current also has a great impact on the induction heating process. To reach the melting point, a pretty high frequency is needed. (To be higher than 1600 Hz is a must in our case.) Also we can control the melting process by controlling the frequency.

4.2 Results and Discussion of Casting Process

4.2.1. Energy Storage Ability of the Mold

When the melt flows into the mold there two issues to consider: the flow and initial solidification of the melt during the initial rapid transient and the final cooling and solidification of the melt once the flow stops. The discussion here centers on developing a simple energy balance to demonstrate whether or not the mold has adequate thermal mass to solidify all of the melt material. If the mold has adequate thermal mass, this implies the melt within the mold will be completely solidified and no additional cooling will be needed. If there were no adequate thermal mass, then active or passive cooling would be necessary to cool and solidify the melt within the mold.

Figure 64 shows a schematic of the simple thermal model. Energy transfers from the melt into the mold, until the system reaches equilibrium – both the melt and mold temperatures are equal.

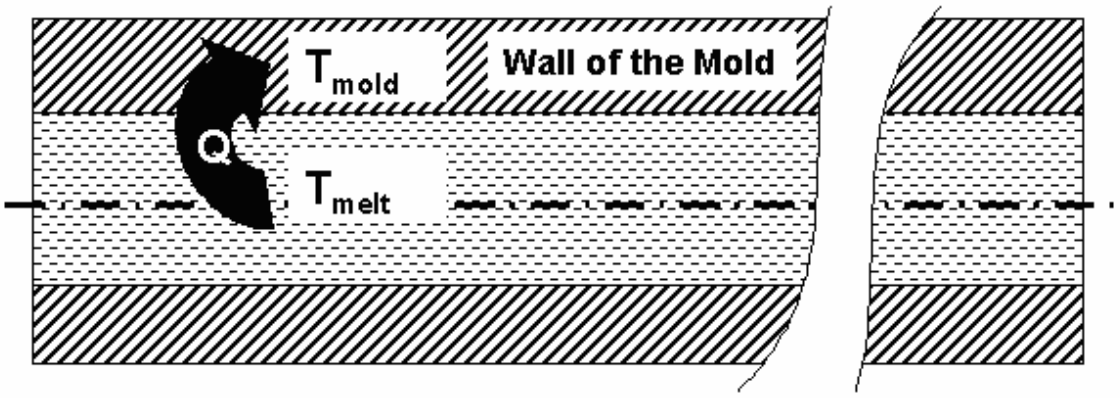

Figure 64 - Heat transfer from the melt to the mold

The ability of storing energy is evaluated by equation (42). We define this ability as how much energy can be stored in the mold to heat it from the preheated temperature to a high temperature for example, 1500 ^{o}C.

$$Q = m_{mold} C_{p\,.mold} \Delta T = \rho_{mold} \{\pi l (r^2{}_{mold} - r^2{}_{pin})\} C_{p.mold} (T_{melt} - T_{pre}) \tag{42}$$

On the other hand, the minimum heat needed to be absorbed from the melt to ensure the phase change. It is calculated from:

$$Q_{\min} = m_{melt} (C_{p\,.melt} \Delta T + L) = \rho_{melt} (\pi l \cdot r^2{}_{pin}) \{C_{p.mold} * (T_{melt} - T_{pch}) + L\} \tag{43}$$

The three different materials evaluated for the mold are quartz glass, copper and stainless steel. Their main properties are show as the Table 1.

Figures 65-67 show typical results for the analysis of the thermal storage capability of the mold. The solid horizontal line represents the amount of energy that must be absorbed by the mold in order to solidify the melt.

Table 1 – Properties for three different mold materials.

	Copper	Stainless Steel	Quartz Glass
Thermal Conductivity(W/m°C)	320	24	1.4
Specific Heat (J/kg°C)	380	461	670
Density (kg/m^3)	8933	7750	2200
Thermal Diffusivity (m^2/sec)	9.4E-05	6.7E-06	9.5E-07

In Figures 65-67, if the intersection of mold radius and dashed preheat line is above the solid line, the mold has enough thermal mass to solidify all of the melt. If the intersection falls below the solid line, then the mold will not absorb all of the energy needed to solidify the melt. It is clear that any practical mold radius will provide more than adequate thermal mass to solidify the melt.

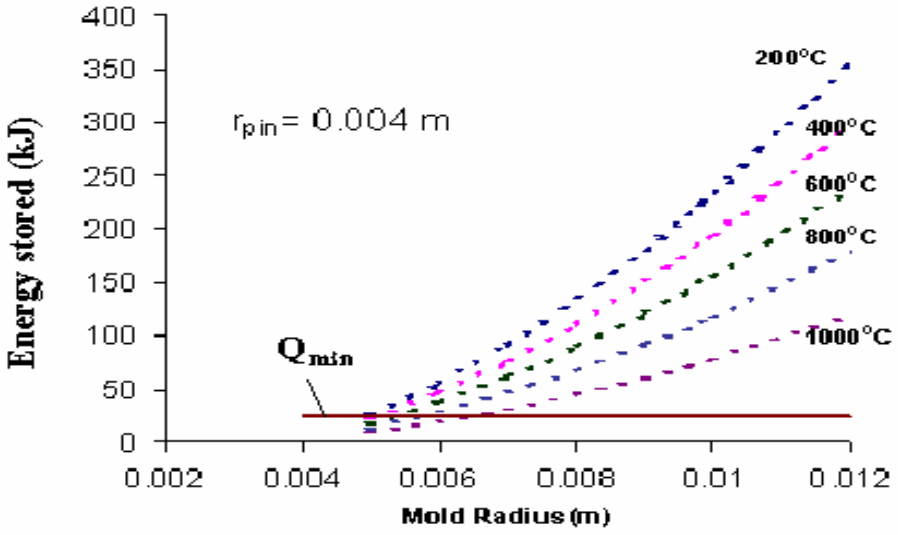

Figure 65 - Energy storing ability of a quartz glass mold

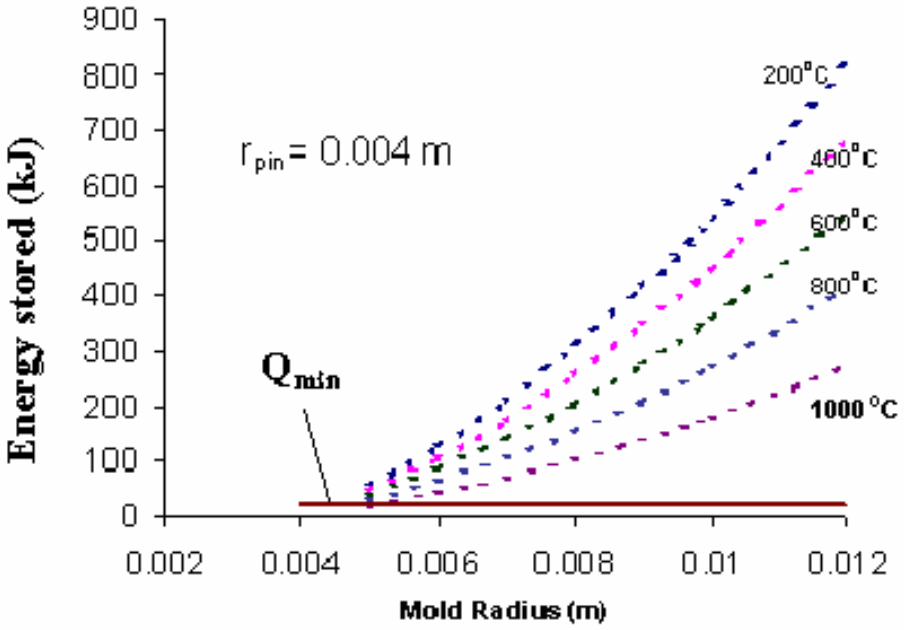

Figure 66 - Energy storing ability of a copper mold.

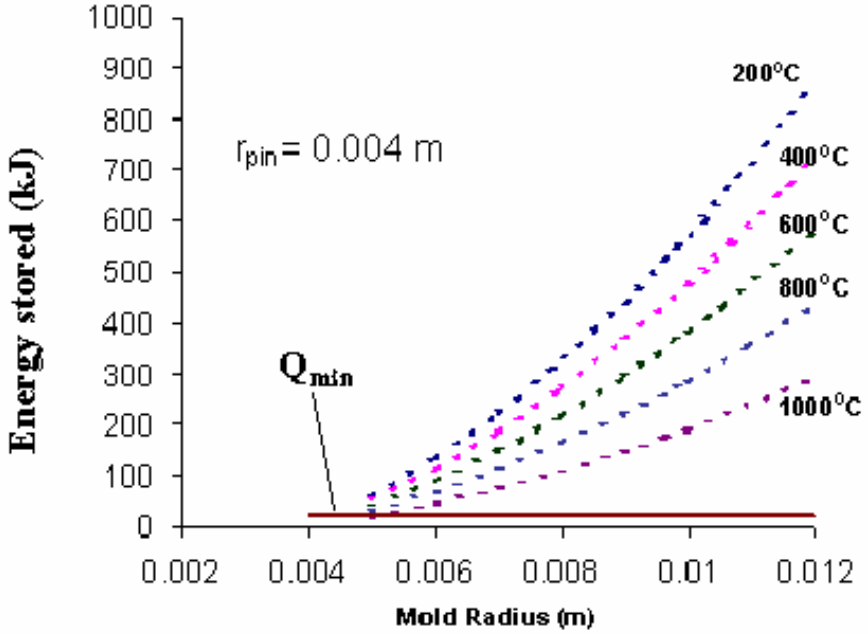

Figure 67 - Energy storing ability of a stainless steel mold.

From the above evaluation, it can be concluded that the bigger the mold outer radius is, the more energy can be stored in the mold. The stainless steel mold has the greatest storing ability whereas the quartz glass mold has the smallest one. On the other hand, for a bigger mold the solidification progress will take a longer time. This will lead to a low efficiency and is not anticipated in production. Finally an outer radius of 0.008 m is selected for the mold by ANL.

This value ensures that the energy stored by the mold is larger than the minimum heat needs to be absorbed from the melt and a fast solidification for all the three kind of mold materials.

4.2.2. Simple Solidification Process

The analysis of "simple" or "pure" solidification considers the mold to be filled with molten material before the solidification begins. The inlet boundary condition can be either constant velocity (simplified injection), or a constant pressure condition (realistic boundary condition for injection casting). This type of analysis gives insight into the time scales one must consider for the solidification of the melt once it is in the mold. In the "simple" solidification, we see a solidification process, in which the interface of the melt and the solidified melt moves in a radial direction. Note that the inlet temperature of the melt is set to a constant temperature representative of the superheat of the melt.

The result output from FIDAP is shown as in Figure 68. Since the mold is pretty skinny, only the part near the inlet is shown here.

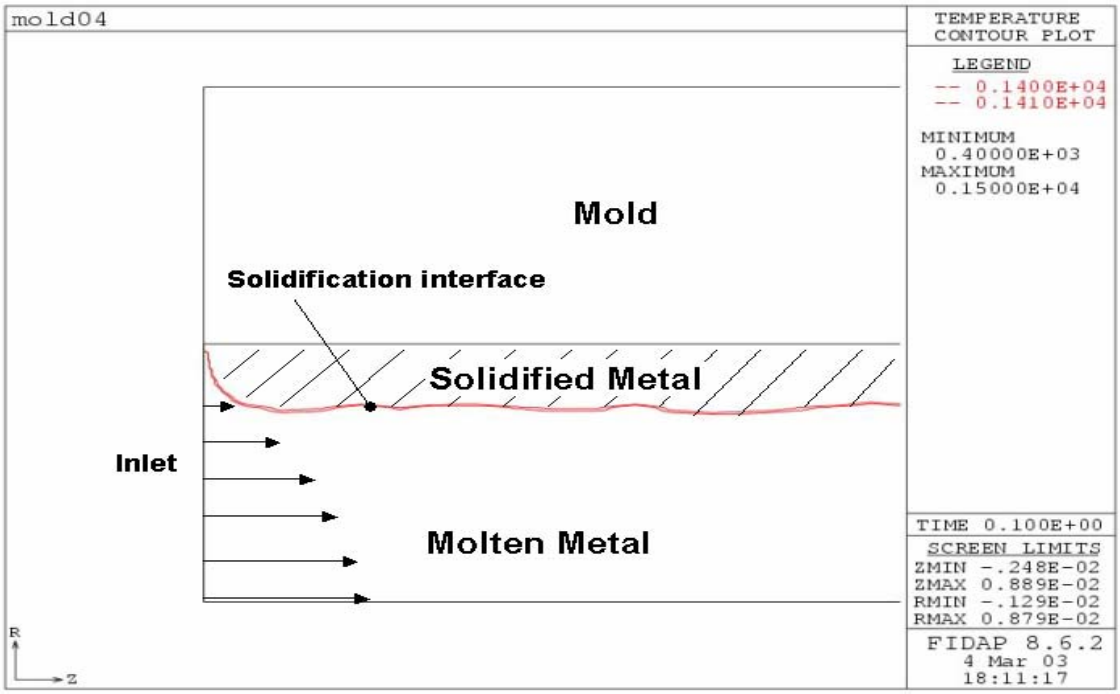

Figure 68 - The "pure" solidification process result from FIDAP

At first we keep the inlet velocity at a constant value. However, this boundary condition will lead to a divergence solution. The reason for this is that if we keep a constant inlet velocity the velocity of the molten material will become larger and larger as the solidification process takes place since the section area for the molten metal to flow through becomes smaller and smaller. The result is shown as in Figure 69.

Then we choose a constant inlet pressure as the filling condition. This simulation gives us a full solidification as shown in Figure 70.

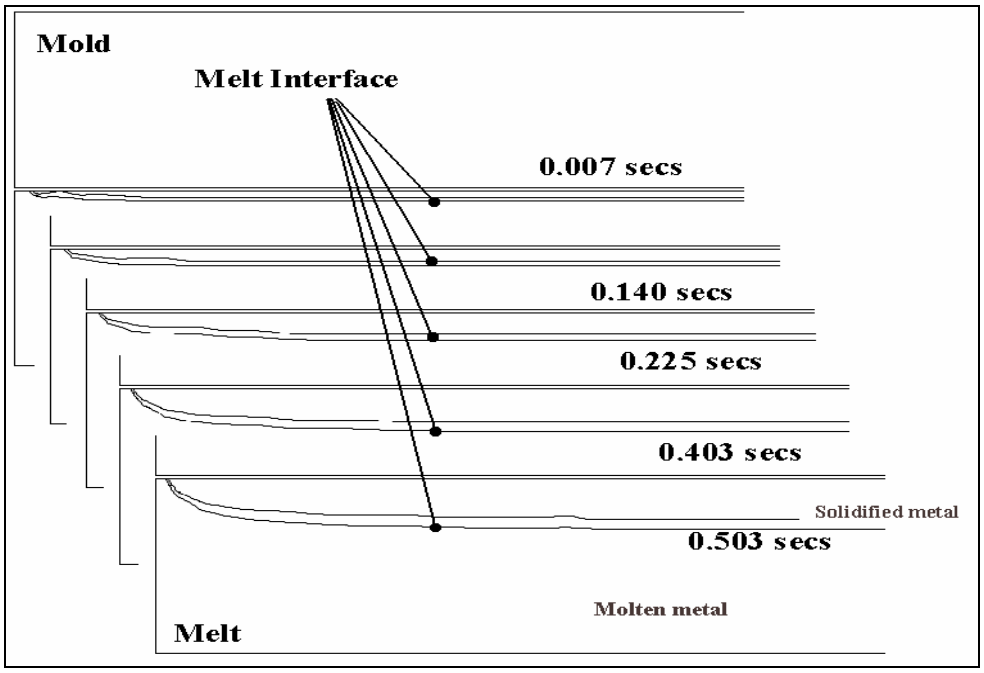

Figure 69 - The "pure" solidification process result for constant inlet velocity case (Mold preheated temperature = 400 ^{o}C, initial melt temperature = 1,500 ^{o}C, h = 2,000 W/m^{2}-K, phase change temperature: 1,400-1,410 ^{o}C; Uave =0.2m/s, mold material: copper)

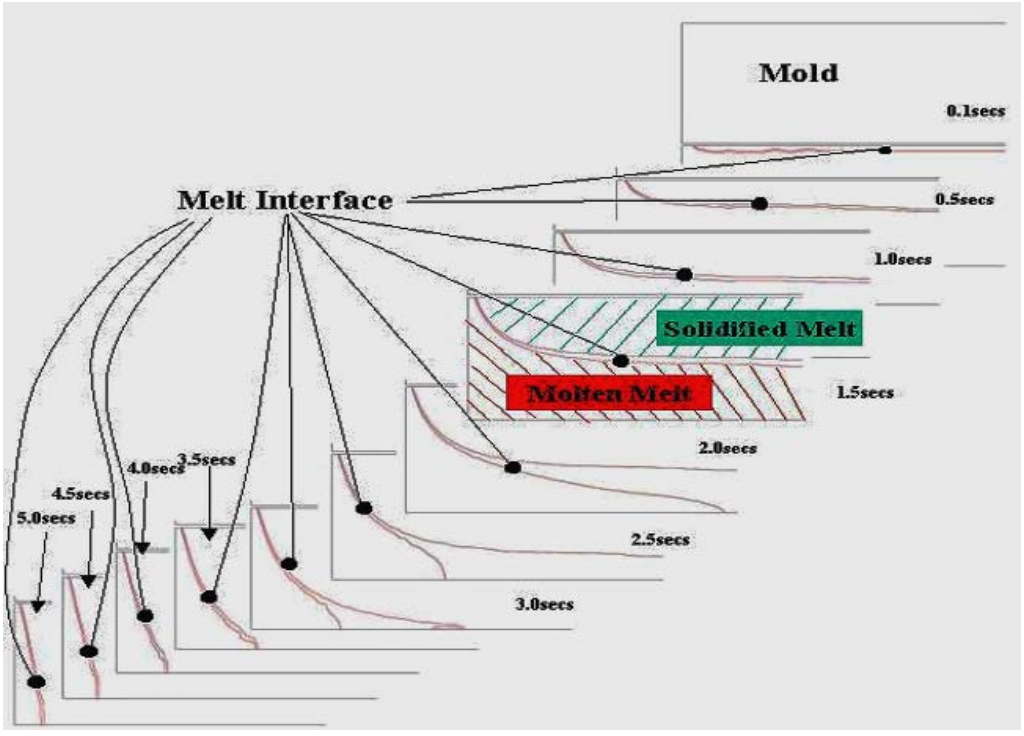

Figure 70 - The "pure" solidification process result for constant inlet pressure case (Constant Inlet Pressure: P=20 kPa, mold preheated temperature = 400 ^{o}C, initial melt temperature = 1,500 ^{o}C, h = 2,000 W/m^{2}-K, phase change temperature: 1,400-1,410 ^{o}C; mold material: copper)

From Figures 69 and 70 the interface of the molten and the solidified metal moves towards the centerline in a radial direction. These results tally with the theoretical analysis in Chapter 3. (See Figure 25)

Figures 71 and 72 show typical cooling and solidification profiles for a representative simulation. The results shown are for a constant pressure inlet condition of 20 kPa, mold heat transfer coefficient of 2,000 W/m^2-K, and an initial mold temperature of 400 ^{o}C. The dashed line in Figure 71 represents the phase change temperature for the simulation. Conduction only occurs within the solidified material as indicated by the nearly linear profiles. Figure 72 shows the heat up of the mold as a function of time. The heat capacity of the mold is much greater than the heat capacity of the molten material. The mold material is assumed to have properties similar to that of copper. The intent of the modeling is to assist in the design of the molds from a materials property standpoint and from a structural standpoint. The mold must be able to maintain its shape without warping while the melt solidifies.

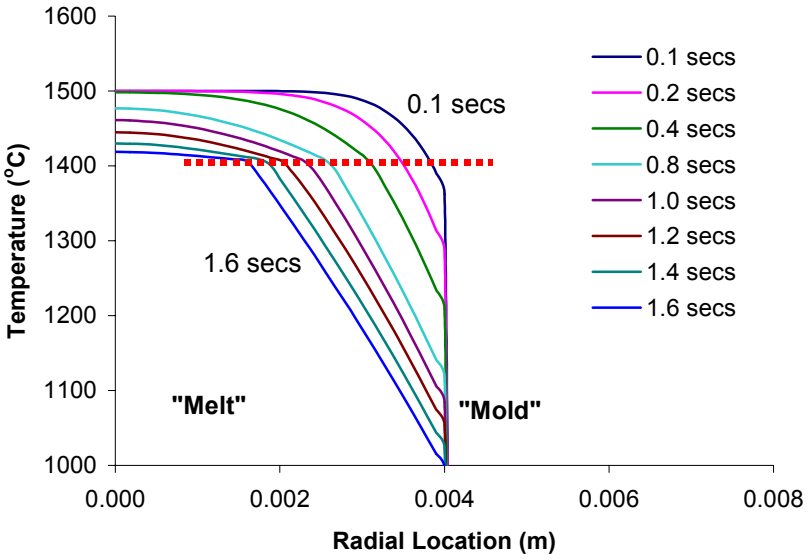

Figure 71 - Temperature profiles for flow through the mold prior to solidification for a constant pressure inlet boundary condition. The dashed line represents the temperature at which phase change occurs. (Inlet pressure = 20 kPa, Mold temperature = 400 ^{o}C, initial melt temperature = 1,500 ^{o}C, interfacial heat transfer coefficient = 2,000 W/m^2-K)

Figure 73 shows how the flow increases in velocity and then starts to decrease in velocity as the melt starts to solidify. A constant pressure boundary condition is representative of the injection casting process where pressure is suddenly ramped up, forcing the molten material into a mold. The flow starts of nearly in a plug flow shape, slowly moves to more of a parabolic shape, and the remains nearly parabolic as the total flow decreases as the melt solidifies towards the center of the geometry.

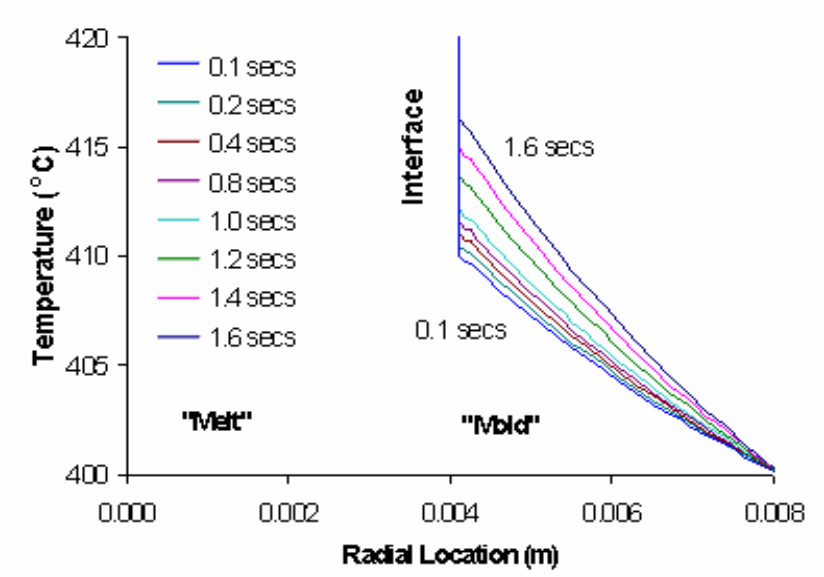

Figure 72 - Temperature profiles for the heating of the mold during the cooling and solidification of the melt. (Inlet pressure = 20 kPa, Mold temperature = 400 °C, initial melt temperature = 1,500 °C, interfacial heat transfer coefficient = 2,000 W/m^2-K)

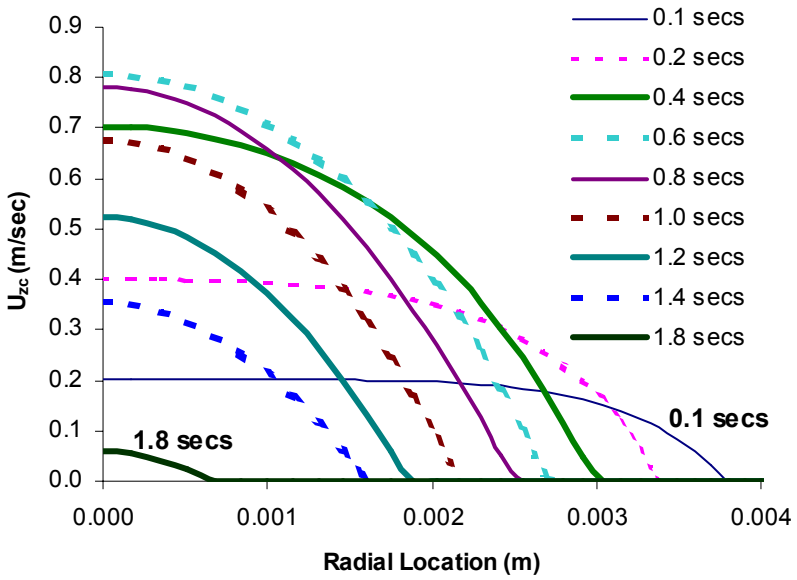

Figure 73 - Axial velocity profile for constant inlet pressure of 20 kPa (Mold temperature = 400 °C, initial melt temperature = 1500 °C, interfacial heat transfer coefficient = 2,000 W/m^2-K)

Figure 74 presents the flow field for a higher heat transfer coefficient for the same inlet pressure. Increasing the heat transfer decreases the peak velocity experienced during the flow and solidification of the melt. The actual heat transfer rates between the mold and the melt are

not known for the present concept because no experimental tests exist on the particular melt mold interface. Therefore, the impact of this parameter is studied and analyzed.

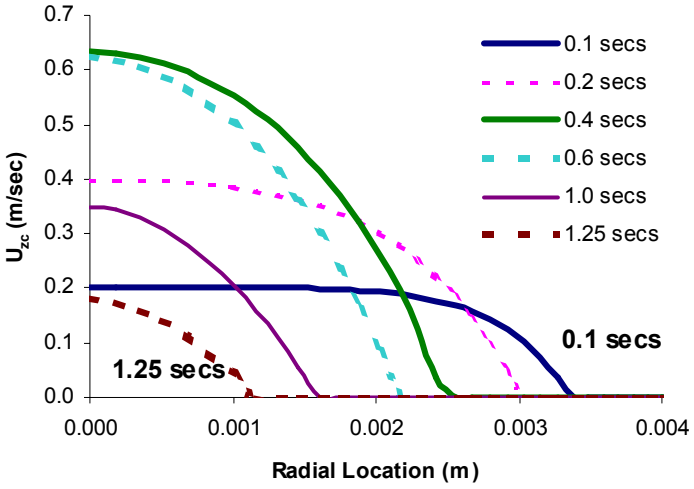

Figure 74 - Axial velocity profile for constant inlet pressure of 20 kPa and a higher heat transfer coefficient (mold temperature = 400 ^{o}C, initial melt temperature = 1500 ^{o}C, interfacial heat transfer coefficient = 5,000 W/m^2-K)

The impact of injection pressure can also be studied as shown in Figure 75. The results here are for an injection pressure at nearly 4 atmospheres. The mold temperature is also lower. The peak velocity is 1-2 orders of magnitude larger.

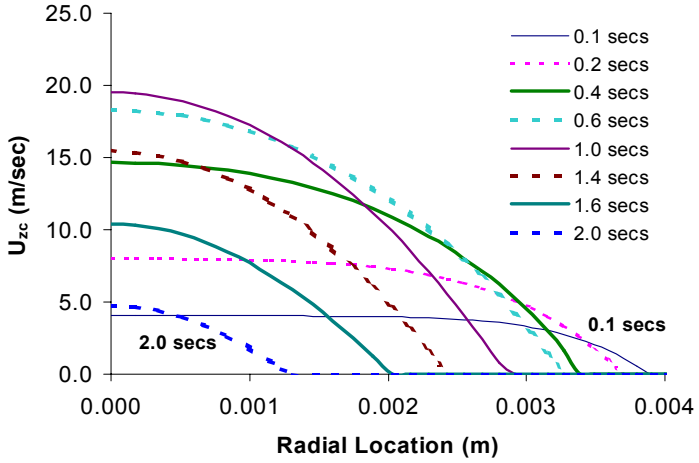

Figure 75 - Axial velocity profile for constant inlet pressure of 400 kPa (mold temperature = 800 ^{o}C, initial melt temperature = 1500 ^{o}C, interfacial heat transfer coefficient = 2,000 W/m^2-K)

The impact of the heat transfer on melt solidification can be found in Figure 76. This figure reports the location of the solidification front as the flow solidifies. The distance is the radial distance from the centerline of the solidification front. Some of the material quickly

solidifies by the wall, and then continues to solidify slowly until the radius becomes small. Once the diameter becomes roughly 25 percent of the outer diameter, the flow quickly solidifies and stops. Slow cooling occurs after this time.

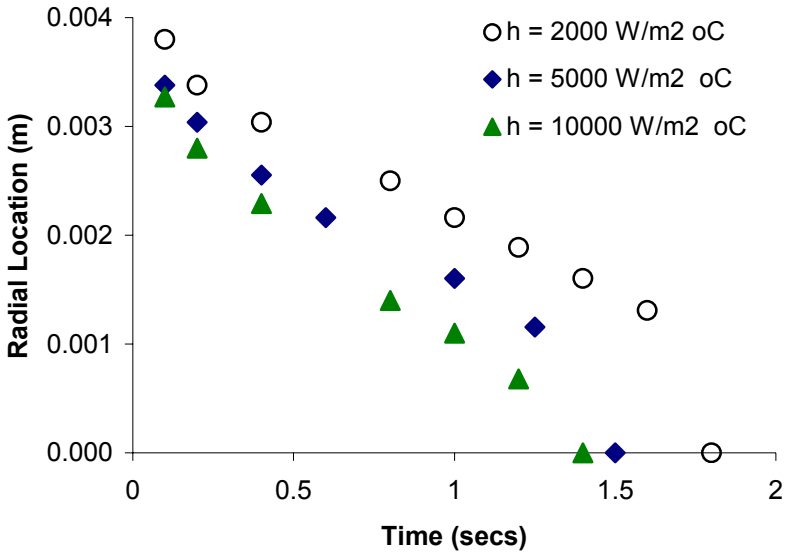

Figure 76 - Comparison of solidification front for different heat transfer coefficients (inlet pressure = 20 kPa, mold temperature = 400 ^{o}C, initial melt temperature = 1500 ^{o}C)

The impact of the mold material on melt solidification can be found in Figure 77. This figure also reports the location of the solidification front as the flow solidifies. The distance is the radial distance from the centerline of the solidification front. From this plot we can see that the melt in a glass quartz mold will solidify much slower than that in a copper mold or a stainless steel mold.

4.2.3. Pure Filling Process

The single-fluid Volume of Fluid (VOF) technique is used to simulate the molten metal entering the mold. In this part of work, we assume the flow temperature is much higher than its melting point so there is no phase change during the filling process. A fully developed flow is assumed so a parabolic velocity is input as the boundary condition. A lot of work of "pure" filling has been done by the former graduate student, Mr. Xiaolong Wu, except for a "slip" boundary condition was used since a "non-slip" boundary condition was easy to lead to a diverging solution. However, a "non-slip" boundary is more reasonable between the solid and the fluid. Using our developed subroutine, a "non-slip" boundary condition along the inner surface of the mold was successfully employed. From Figure 78 a parabolic velocity profile was kept from the inlet till the leading head. Solid line across the velocity vectors represents the fill front.

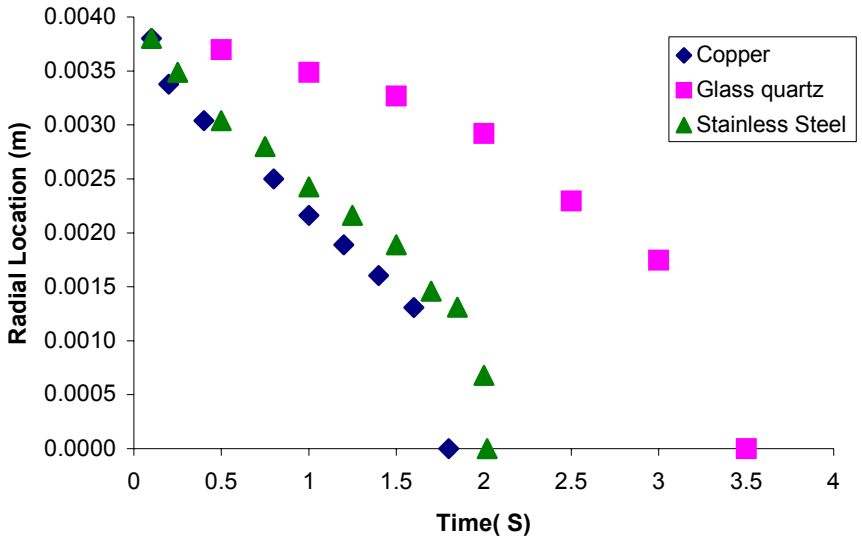

Figure 77 - Comparison of solidification front for different mold materials (inlet pressure: p= 20 kPa; inlet temperature= 1500 ^{o}C; mold preheated temperature: T=400 ^{o}C; phase change temperature: 1,400-1,410 ^{o}C; interfacial heat transfer coefficient h=2,000 W/m^{2}-K)

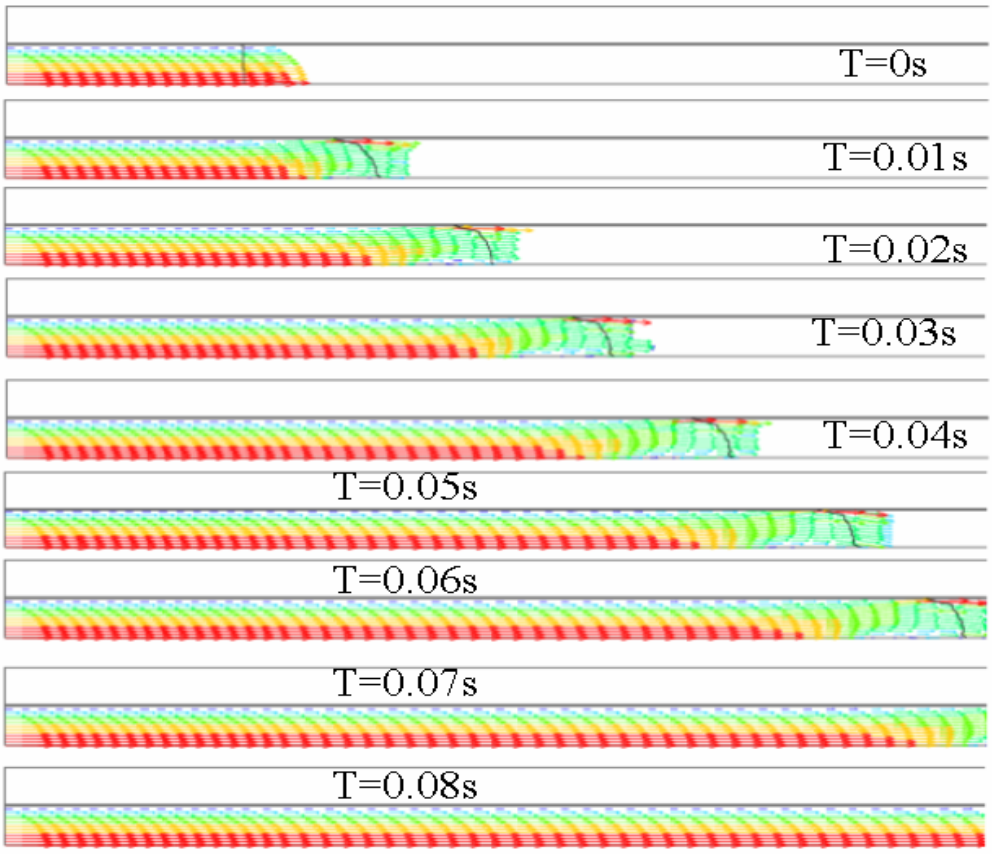

Figure 78 - Representative flow field for free surface flow into mold region (axisymmetric geometry shown). (inlet velocity Uavg=1 m/s, mold material: copper, inlet temperature: 1,500 ^{o}C, heat transfer coefficient h=2,000 W/m^{2}-K, mold preheated temperature 800 ^{o}C)

With the comparison of various cases for different boundary condition or initial condition, we found Mr. Xiaolong Wu's conclusions [43] are still suitable for this "pure" filling process with "non-slip" boundary condition:

- The mold-preheated temperature has certain effect on the heat transfer during the filling process.
- The heat transfer coefficient affects the heat transfer largely in the filling process.

4.2.4. Casting Process

The single-fluid Volume of Fluid (VOF) technique is again used in the casting process and phase change is considered at the same time. The VOF-solidification process near the inlet of the mold is shown in Figure 79.

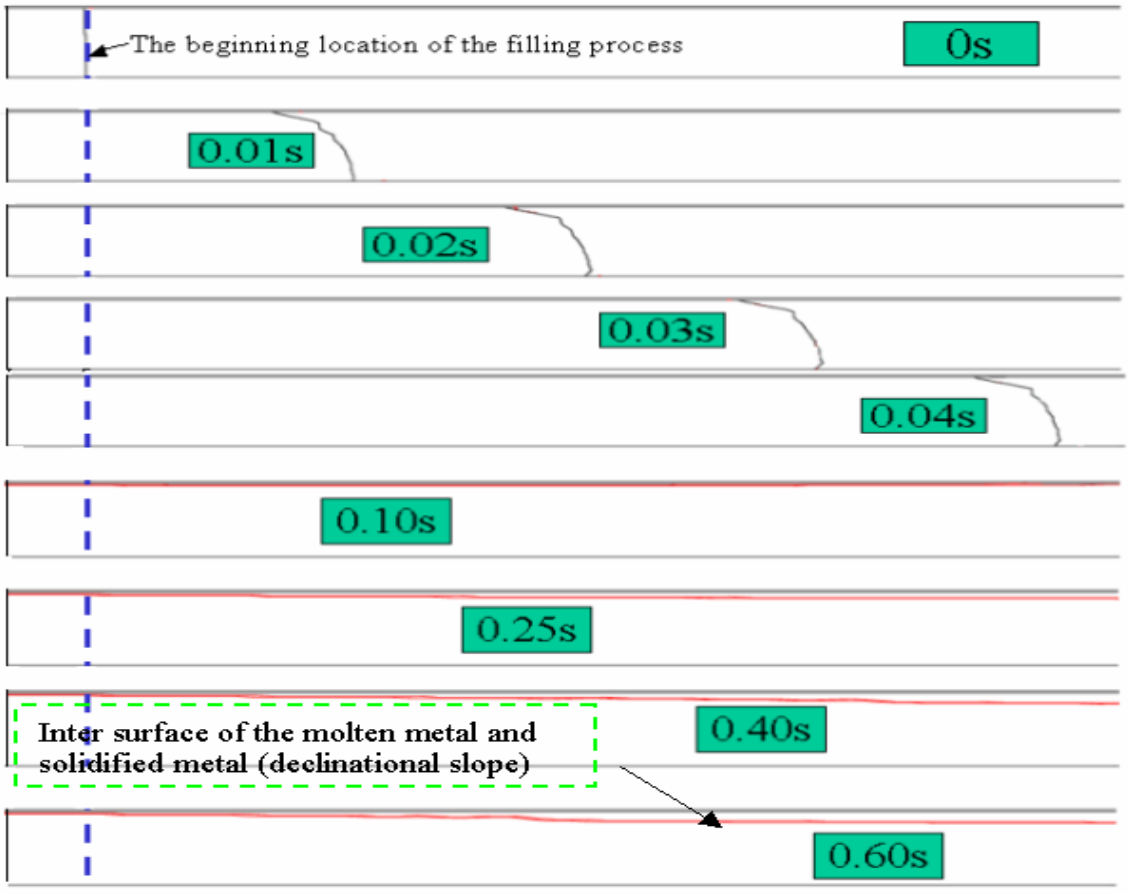

Figure 79 - VOF-solidification process near the inlet of the mold (average inlet velocity Uavg=1 m/s, (Parabolic velocity profile), mold material: copper, inlet temperature: 1,500 ^{o}C, Heat transfer coefficient h=2,000 W/m^{2}-K, mold preheated temperature: 800 ^{o}C)

The VOF-solidification process near the outlet of the mold is shown in Figure 80.

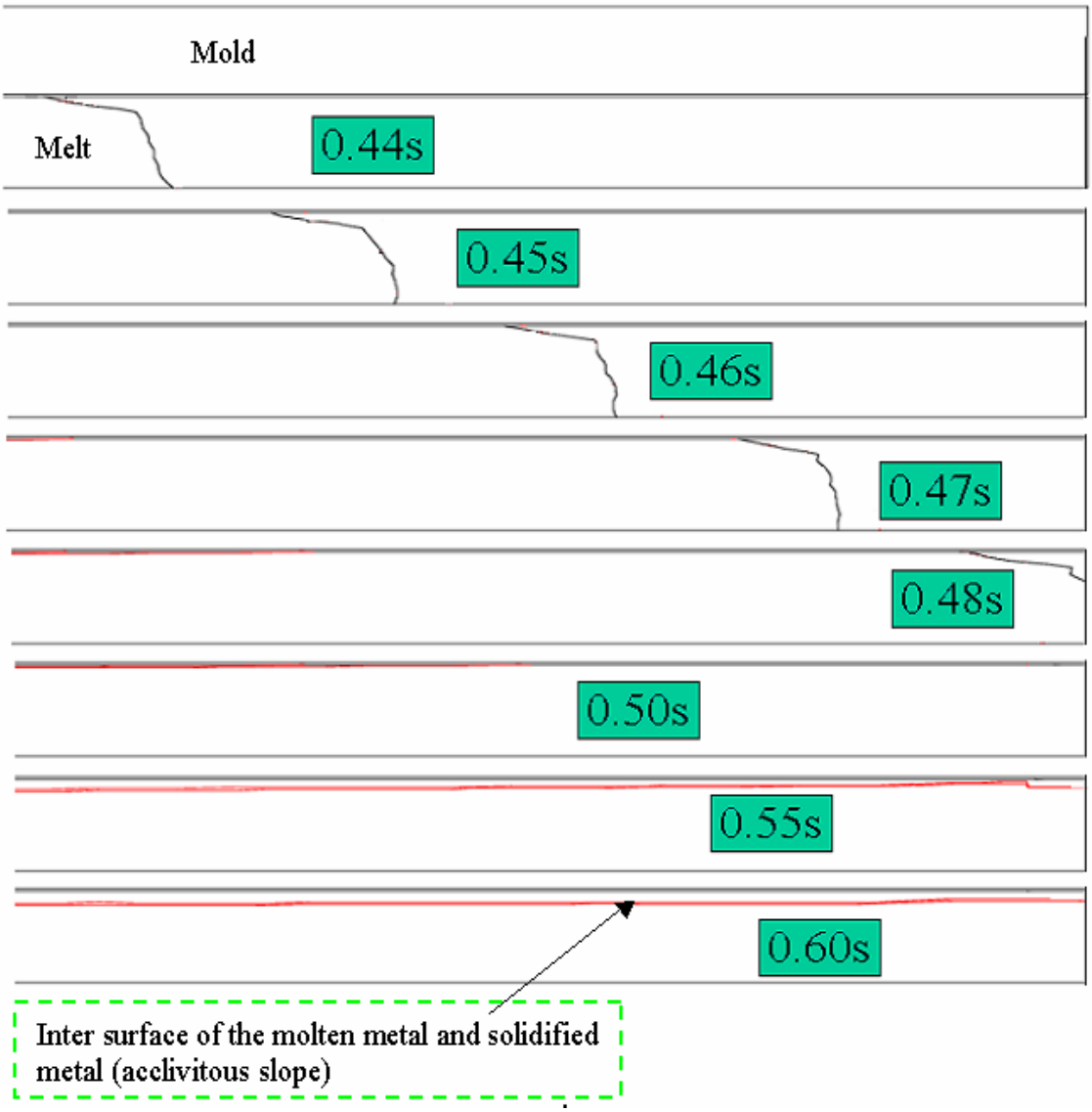

Figure 80 - VOF-solidification process near the outlet of the mold (average inlet velocity Uavg=1 m/s, (parabolic velocity profile), mold material: copper, inlet temperature: 1,500 ^{o}C, heat transfer coefficient h=2,000 W/m^{2}-K, mold preheated temperature: 800 ^{o}C)

From Figures 79 and 80, we can observe the two slopes clearly. This result coincides with our theoretical analysis in Chapter 3. (See Figure 27) From the calculations we also found that a larger value of the convection heat transfer coefficient will lead to a steeper slope. If the h value is too small, the solidification will not take place at the head of the molten (Left plot of Figure 81), which means the slope is behind the filling head and it will take a longer time for all the molten metal in the mold to solidify.

In the casting process as shown in Figure 82, the velocity profiles are found increasing rapidly and then dropping off as solidification occurs.

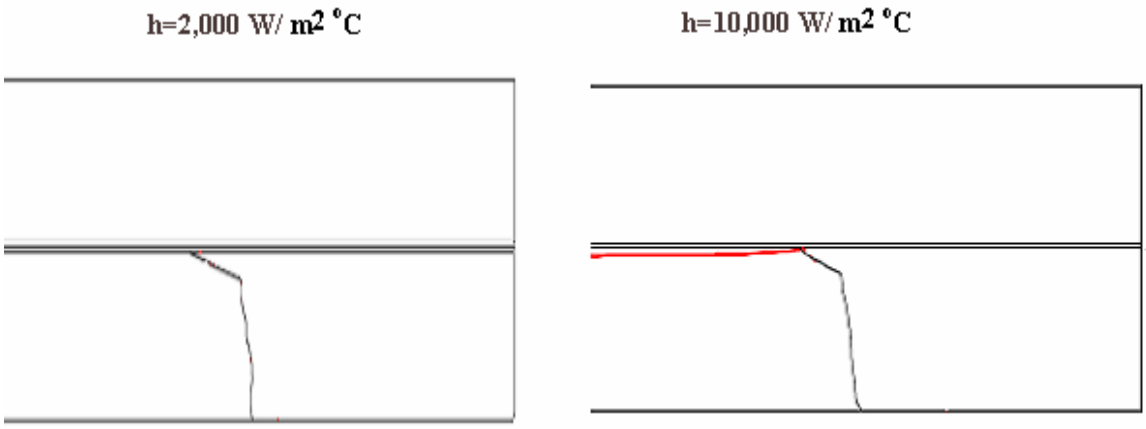

Figure 81 - The acclivitous slope for different h value in VOF-solidification process (average inlet velocity Uavg=1 m/s, (parabolic velocity profile), mold material: copper, inlet temperature: 1,500 °C, mold preheated temperature: 800 °C)

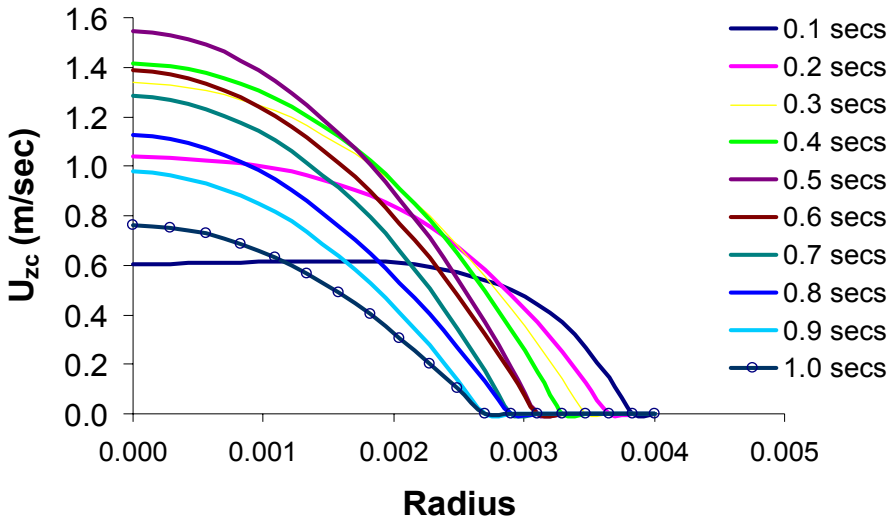

Figure 82 - Velocity profiles for different time steps in the VOF-solidification process (average inlet velocity Uavg =1 m/s, (parabolic velocity profile), mold material: copper, inlet temperature: 1,500 °C, heat transfer coefficient h=2,000 W/m^2-K, mold preheated temperature: 800 °C)

The main difference between the VOF-solidification process and the "pure" solidification is the slopes. The flat interface of the "pure" solidification is because we assumed the molten metal has filled the whole mold before the solidification took place, so there is almost no temperature difference in the wall of the mold. Moreover, there is no filling "head" and in turns there is no time difference for solidifying along the mold. And we noticed that the slop is very small especially when h value is not too high. From the calculations above, we can draw a

conclusion that the casting process can be analyzed by studying the "pure filling" and "pure solidification" process separately.

5. Conclusions and Recommendations

After considering the heating mechanisms, casting issues, crucible design and issues related to the mass transport of americium, an ISM system was selected for melting the feedstock and casting fuel pins containing high vapor pressure actinides (americium). The finite element commercial software (FIDAP) was used to simulate the induction melting process and the casting process. Phase change is considered both in the heating and in the solidification process. Various factors and properties are studied, such as boundary conditions and initial conditions, output current, frequency of the current, main dimensions of the system, mold preheating temperature, heat transfer coefficient and mold material. As shown in simulated results, several conclusions can be drawn:

- The design of the system has great impact on the induction melting process. In order to obtain high heat efficiency, the coils group number can be designed as many as possible and the coils are located as near to the crucible as possible.
- The induction melting process is sensitive to the electrical factors and properties (Current density; frequency and output power). Through the control of these values we can control the melting process. The thermal properties of the feedstock and the crucible material are also important in the heating process.
- A direct IH has a much higher efficiency than an indirect IH. In order to form the "skull", a low temperature and good thermal conductivity of the coolant is necessary.
- A VOF-Solidification process can be "divided" to a filling process and a solidification process and be studied respectively, especially for a case of low convective heat transfer coefficient value.
- A constant filling pressure is expected rather than a constant velocity in the casting process.
- Mold material, mold preheated temperature, inlet pressure, and heat transfer coefficient have relative large effects to the casting process.

The following recommendations are made for future work:

- Employ turbulent model for the inductive self-stirring effect in the induction melting process.
- Study on the mass transfer process of americium and analyze the control methods for decreasing the transfer efficient.

6. References

1. Carmelo Rodriguez, A. Baxter et al., "Transmutation of Nuclear Waste Using Gas-cooled Reactor Technologies", ICONE 8, Baltimore, MD USA, April 2-6, 2000.
2. R.L. Sheffield, "Super Conducting Technologies for the Advanced Accelerator Application Program", LANL, Los Alamos, NM 87545, USA.
3. Frank J.Rahn, Achilles G. Adamantiades, John E. Kenton, Chaim Braun, "A Guide to Nuclear Power Technology", ISBN 0-471-88914-8, 1984.
4. Dick Kovan et al. "The World Nuclear Handbook", ISBN 0-8160-1924-X, First edition, 1988.
5. John R. Lamarsh, "Introduction to Nuclear Engineering", Second Edition, ISBN 0-201-14200-7, 1983.
6. Pierre Bacher, "Objectives of Advanced Nuclear Power System", Proceedings of an ENS Class 1 Topic Meeting, Research Facilities for the Future of Nuclear Energy, Brussels, Belgium, 4-6 June, 1996, ISBN 981-02-2779-5, P124-133.
7. Jan Wallenius et al. "Application of Burnable Absorbers in an Accelerator Driven System", GLOBAL 2001, International Conference on Back-End of the Fuel Cycle, Paris, September 9-13, 2001.
8. M. Delpech et al. "The Am and Cm Transmutation, Physics and Feasibility", International Conference on Future Nuclear Systems, GLOBAL 99, ANS, 1999.
9. J.J.R.Rycroft, "Fuel Concepts in Support of Advanced Nuclear Plant Operation", Proceedings of an ENS Class 1 Topic Meeting, Research Facilities for the Future of Nuclear Energy, Brussels, Belgium, 4-6 June, 1996, ISBN 981-02-2779-5, P134-143.
10. Owen C. Jones, Jr. "Nuclear Reactor Safety Heat Transfer", ISBN 0-89116-224-0, 1981.
11. Seaborg, G. T., Katz, J. J., and Manning, W. M. (eds) (1949) The Transuranium Elements: Research Paper, Natl Nucl. En. Ser., Div. IV, 14B, McGraw-Hill, New York.
12. Joseph J. Katz, Glenn T. Seaborg and Lester R. Morss, "The Chemistry of the Actinide Elements", Second edition, Volume 2.
13. F.L. Oetting, M.H. Rand and R.J. (1976) The Chemical Thermodynamics of Actinides Elements and Compounds (Part1: The actinides elements), International Atomic Energy Agency, Vienna.
14. Joseph J. Katz, Glenn T. Seaborg and Lester R. Morss, "The Chemistry of the Actinide Elements", Second edition, Volume 2.
15. Xiaolong Wu, Randy Clarksean, Yitung Chen, Mitchell K. Meyer," Design and Analysis for Melt Casting Metallic Fuel Pins", ICAPP2002, Hollywood, Florida, June 9-13, 2002.
16. Xiaolong Wu, Randy Clarksean, Yitung Chen, Mitchell K. Meyer," An Analysis of the Melt Casting of Metallic Pin", IMECE2002, New Orleans, LA, November 17-22, 2002.
17. Taide Tan, Randy Clarksean, Yitung Chen, Mitchell K. Meyer, "Simulation and Analysis for Melt Casting a Metallic Fuel Pin Incorporating Volatile Actinides", IMCE2003-42092, ASME International Mechanical Engineering Congress and R&D Expo, Washington, DC, November 16-21, 2003.
18. Taide Tan, Randy Clarksean, Yitung Chen, Mitchell K. Meyer, "Numerical Simulation of an Induction Heating Process in An Induction Skull Melting Furnace ", CHT-04-200, ICHMT International Symposium on Advances in Computational Heat Transfer, Norway, April 19-24, 2004.

19. Pruncer, C. et al., “Transmutation of Minor Actinides: Behavior of Americium- and Neptunium-Based Fuels Under Irradiation”, Proc. International Conference on Fast Reactors and Related Fuel Cycles, Vol. II, p. 19.2, Kyoto, Japan, October, 1991.
20. Buccafurni, A, Landeyro, P.A., “Minor Actinide Burning in Thermal Systems”, Proc. 1992 Topical Meeting on Advances in Reactor Physics, Vol. 1, p. 1-301, Charleston, South CaroIina March 1992.
21. Bowman, C.D., “Transmutation of Existing Waste”, Specialist Meeting on Accelerator-Driven Transmutation Technology for Radwaste and Other Applications, SaltsjWaderh Stockholm, SW- June 1991.
22. Hill R.N. et al., “Physics Studies of Higher Actinide Consumption in an Lm” Proc. Ml. conference on the Physics of Reactor Operation, Design, and Computation Vol. 1, p. L83, Marseille, France, April 1990.
23. Khalil H., Hill R. et al. “Physics Considerations In the Design of Liquid Metal Reactors For Transuranium Element Consumption”, Argonne National Laborator, 9700 South Cass Avenue Argonne Illinois 60439-4842 U.S.A.
24. Till C.E., Chang, Y.I., “Progress and Status of the Integral Fast Reactor (IFR) Fuel Cycle Development”, Proc. International Conference on Fast Reactors and Related Fuel Cycles, Vol. I, p. 1.6, Kyoto, Japan, October 1991.
25. C.L. Trybus, J.E. Sanecki and S.P. Henslee (1993), “Casting of metallic fuel containing minor actinide additions, ” J. of Nuclear Materials 204, pp. 50-55.
26. F.L. Oetting, M.H. Rand and R.J. (1976) The Chemical Thermodynamics of Actinides Elements and Compounds (Part1: The actinides elements), International Atomic Energy Agency, Vienna.
27. Bellot J.P. et al. “Evaporation of Fe and Cr from Induction –stirred austenitic stainless Steel. Influence of the Inert Gas Pressure”, ISIJ International, Vol. 41(2001), No.7, pp.696-705.
28. Jingjie Guo et al. “Evaporation Behavior of Aluminum during the Cold Crucible Induction Skull Melting of Titanium Aluminum Alloys”, Metallurgical and Materials Transactions B, Vol. 31B, August 2000, pp.837-844.
29. Jingjie Guo et al. ”Mechanism of Skull Formation during Induction Skull Melting of Intermetallic Compounds”, Int. J. Cast Metals Res., 1999, 12, 35-40.
30. E.J. Davies, “Conduction and Induction Heating”, ISBN 0-86341-174-6, Peter Peregrinus Ltd. London, United Kingdom, 1990.
31. Jackson, J.D., John Wiley and Sons, “Classical Electrodynamics’, New York, Second Edition, 1975.
32. Dean M. Peters, “Casting Titanium at Duriron, Drrioun Succeeds with Titanium and Zirconium Investment Casting through the Use for its Slagless Induction Skull Melting (ISM) Process”, Foundry Management & Technology, October 1996, p.34-37.
33. “Induction Heating System Topology Review, Discrete Application”, Power Device Division, Fairchild Semiconductor, Fairchild Semiconductor AN9012, Rev D, July 2000, p.1-27.
34. Nathan Ida, Joao P.A. Bastps, “Electromagnetics and Calculation of fields”, Second edition, ISBN 0-387-94877-5, 1997.
35. Gross, C. et al., “Power Consumption of Skull Melting, Part I: Analytical Aspects and Experiments,” Cryst. Res. Technol., Vol. 34, no. 3, p. 319-328. 1999.

36. Muiznieks, A. et al., 1999 “Power Consumption of Skull Melting, Part II: Numerical Calculations of the Shape of the Molten Zone and Comparison with Experiment,” Cryst. Res. Technol., Vol. 34, no. 3, p. 329-338.
37. Vlatko Cingoski and Hideo Yamashita, “Analysis of Induction Skull Melting Furnace by Edge Finite Element Methods Excited from Voltage Source, ” IEEE Transactions on Magnetics “, Sep. 1994, Vol. 30, No. 5, pp. 3459-3462.
38. P.G. Breig and S. W. Scott (1989), “Induction Skull Melting of Titanium Aluminides, ” Materials & Manufacturing Processes, Vol. 4(1), pp. 73-83.
39. Hidekazu Kurimoto, Harendra Hath Mondal, and Toshiya Morisue (1996), “Analysis of Velocity and Temperature Fields of Molten Metal in DC Electric Arc Furnace, ” J. of Chemical Engineering of Japan, Vol. 29, No.1, pp. 75-81.
40. Frank Kreith Mark S.Bohn, “Principles of heat transfer”, Sixth Edition.
41. Gresho Philip M. and Jeffrey, J. Derby, 1987, “Solution of the Time-Harmonic Semi-Maxwell Equations for Induction Heating Using FIDAP,” First FIDAP User’s Group Meeting, Summer, Evanston, Illinois.
42. Atherton, L.J., and Martin, R.W., 1988 “Modeling Induction Heating and 3-D Heat Transfer for Growth of Rectangular Crystals Using FIDAP,” Second FIDAP User’s Group Meeting, Summer, Evanston, Illinois.
43. Xiaolong Wu, August, 2002, “Design and Analysis for Melt Casting Metallic Fuel Pins Incorporation Volatile Actinides”.
44. Gresho, Philip M., 1987, “Model Development for Induction Heating,” Lawrence Livermore National Laboratory Internal Report UCID-21154, August.
45. Gresho, P. M., and Derby, J. J., “A Finite Element Model for Induction Heating of a Metal Crucible,” Journal of Crystal Growth, 85:40-48.
46. Derby, J. J., Atherton, L. J., and Gresho, P. M., 1989, “An Integrated Process Model for the Growth of Oxide Crystals by the Czochralski Method,” Journal of Crystal Growth, 97:792-826.
47. FIDAP 8.6 User's Manual, Fiprep Manual, pr09.16-20; Theory Manual, Chapter 6; Examples Manual, Example 30, Example 34.
48. Frank M. White, “Viscous Fluid Flow”, Second Edition, ISBN 0-07-069712-4.
49. Kvicinsky, F. Longatte, J. L. Kueny and F. Avellan, “Free Surface Flows: Experimental Validation of Volume of Fluid (VOF) Method in the Plane Wall Case”, Proceedings of the 3rd ASME/JSME Joint Fluids Engineering Conference, July 18-23 1999, San Francisco, California.
50. Nichols, B.D. and Hirt, C.W., "Methods for Calculating Multi-Dimensional, Transient Free Surface Flows Past Bodies," Proc. First Intern. Conf. Num. Ship Hydrodynamics, Gaithersburg, ML, Oct. 20-23, 1975.
51. Darrell W. Pepper, Juan C. Heinrich, The Finite Element Method, Basic Concepts and Applications, 1991.
52. Darrell W. Pepper, Juan C. Heinrich, Intermediate Finite Element Method, Fluid Flow and Heat Transfer Application, ISBN: 1-56032-309-4, 1999.
53. Timothy Todd de Bues, “ An H-Adaptive Finite Element Compressible Flow Solver Applied to Light-Gas Gun Design”, May 2003.
54. Segerlind L. J., Applied Finite Element Analysis, New York, Wiley, 1976.

55. Harris, R., and Davenport, W.G., 1982, “Vacuum Distillation of Liquid Metals: Part 1. Theory and Experimental Study," *Metallurgical Transactions B*, vol. 13B, December, pp. 581-88.
56. Harris, R., and Davenport, W.G., 1982, “Vacuum Distillation of Liquid Metals: Part 1. Photographic Study," *Metallurgical Transactions B*, vol. 13B, December, pp. 589-91.
57. Ozberk, E., and Guthrie, R.I.L., 1985, “Evaluation of Vacuum Induction Melting of Copper Refining," *Transactions of the Institution of Mining and Metallurgy Section C Mineral Processing and Extractive Metallurgy*, vol 94, September, pp. C146-C157.
58. Ozberk, E., and Guthrie, R.I.L., 1986, “A Kinetic Model for the Vacuum Refining of Inductively Stirred Copper Melts," *Metallurgical Transactions B*, vol. 17B, March, pp. 87-103.
59. Hino, M., Wand, S., Nagasaka, T., and Ban-ya, S., 1994, “Evaporation Rate of Zinc in Liquid Iron," *ISIJ International*, vol. 34, no. 6, pp. 491-97.
60. Li, L., Tu, S., and Janke, D., 1995, “Kinetics of Zn and Pb Evaporation from Liquid Iron," *Steel Research*, vol. 66, no. 5, pp. 188-93.
61. Guo, J., Yuan, L. Yanquing, S., Hongsheng, D., and Jun, J., 1998, “Evaporation Behavior of Components in Ti-15-3 Melt During ISM Process," *Transactions of Nonferrous Metals Society of China*, vol. 8, no. 4, pp. 539-43.
62. Guo, J., Liu, Y., Su, Y., Ding, H., Liu, G., and Jia, J., 1999, “Evaporation Behavior of Aluminum During the Cold Crucible Induction Skull Melting of Titanium Aluminum Alloys," *Metallurgical and Materials Transactions B*, vol 31B, August, pp. 837-44.
63. Savov, L. and Janke, D., 2000, “Evaporation of Cu and Sn from Induction-Stirred Iron-Based Melts Treated at Reduced Pressure," *ISIJ International*, vol. 40, no. 2, pp. 95-104.
64. Guo, J., Liu, G., Su, Y., Liu, Y., Ding, H.S., and Jia, J, 2000, “Control of Al Content during ISM Process of Nb_3Al," *Transactions of Nonferrous Metals Society of China*, vol. 10, no. 5, pp. 571-75.
65. Bellot, J.P., Duval, H., Ritchie, M., Mitchell, A., and Ablitzer, D., 2001, “Evaporation of Fe and Cr from Induction-Stirred Austenitic Stainless Steel. Influence of Inert Gas Pressure," *ISIJ International*, vol. 41, no. 7, pp. 696-705.
66. Gokcen, N.A., 1986, Statistical Thermodynamics of Alloys, Plenum Press, New York.
67. Saito, T. (editor), 1999, Computational Materials Design, Springer, London.
68. Ilegbusi, O.J., Iguchi, M., and Wahnsiedler, W., 2000, Mathematical and Physical Modeling of Materials Processing Operations, Champan and Hall (CRC), Boca Raton, Florida.
69. Liw, H. and Bouchard, M., 1997, “Evaluation of Interaction Coefficient in Al-Cu-H Alloy," *Metallurgical and Materials Transactions B*, vol. 28B, August, pp. 625-632.
70. Waseda, Y., Ueno, S., and Toguri, J.M., 1989, “Theoretical Calculation of Solute Activity Coefficient at Infinite Dilution in Metallic Solution," *Zeitschrift fur Metallkunde*, vol. 80, no. 6, pp. 406-12.
71. Ogawa, T., 1993, “Alloying Behavior Among U, Np, Pu, and Am Predicted with the Brewer Valence Bond Model," *Journal of Alloys and Compounds*, vol. 194, pp. 1-7.
72. Dubinin, N.E., Yuryev, A.A., and Vatolin, N.A., 1995, “Thermodynamic Properties of Ternary Liquid Metal Alloys," *High Temperature Materials and Processes*, vol. 14, no. 4, pp. 285-290.

73. Wang, F.M., Li, X.P., Han, Q.Y., and Zhang, N.X., 1997, “A Model for Calculating Interation Coefficients Between Elements in Liquid and Iron-Base Alloy," *Metallurgical and Materials Transactions B*, vol. 28B, February, pp. 109-113.
74. Ueno, S., Waseda, Y., Jacob, K.T., and Tamaki, S., 1988, “Theoretical Treatment of Interaction Parameters in Multicomponent Metallic Solutions," *Steel Research*, vol 59, no. 11, pp. 474-83.
75. Toop, G.W., 1965, “Predicting Ternary Activities Using Binary Data," *Transactions of the Metallurgical Society of AIME*, vol. 233, pp. 850-55.
76. Sherwood, T.K., and Cooke, N.E., 1957, “Mass Transfer at Low Pressures," *A.I.Ch.E. Journal*, vol. 3, no. 1, pp. 37-42.
77. Tanaka, T., Gokcen, N.A., and Morita, Z., 1990, “Relationship Between Enthalpy of Mixing and Excess Entropy in Liquid Binary Alloys," *Zeitschrift fur Metallkunde*, vol. 81, no. 1, pp. 49-54.
78. Tanaka, T., Gokcen, N.A., Spencer, P.J., Morita, Z., and Iida, T., 1993, “Evaulation of Interaction Parameters in Dilute Liquid Ternary Alloys by a Solution Method Based on the Free Volume Theory," *Zeitschrift fur Metallkunde*, vol. 84, no. 2, pp. 100-05.
79. Pehlke, R.D., 1973, Unit Processes of Extractive Metallurgy, American Elsevier Publishing Company, Inc., New York.
80. Turkdogan, E.T., 1980, Physical Chemistry of High Temperature Technology, Academic Press, New York.
81. Akinlade, O., and Sommer, F., 2001, “Concentration Fluctuations and Thermodynamic Properties of Ternary Liquid Alloys," *Journal of Alloys and Compounds*, vol. 316, pp. 226-235.
82. Su, Y., Guo, J., Ding, H., Liu, S., Liu, Y., Liu, G., and Jia, J., 2001, “Component Evaporation of Ti-15-3 Melt During ISM Processing," *Journal of Materials Science and Technology*, vol. 17, no. 1, pp. 83-4.
83. Gokcen, N.A., 1997, “Thermodynamics of Solutions: A Unified Concept," *J Chim Phys*, vol. 94, pp. 817-843.
84. Maeda, M., Kiwake, T., Shibuya, K., and Ikeda, T., 1997, “Activity of Aluminum in Molten Ti-Al Alloy," *Materials Science and Engineering*, vol. A239-240, pp. 276-80.
85. Ma, Z., 2000, “Thermodynamic Description for Concentrated Metallic Solutions Using Interaction Parameters," *Metallurgical and Materials Transactions B*, vol 32B, February, pp. 87-103
86. Ding, X., Fan, P., and Wang, W., 1999, “ Thermodynamic Calculation for Alloy Systems," *Metallurgical and Materials Transactions B*, vol. 30B, April, pp. 271-77.
87. Gokcen, N.A., Tanaka, T., and Morita, Z., 1993, “Atomic Theories on Energetics of Alloy Formation," *J Chim Phys*, vol. 90, pp. 233-248.
88. Turkdogan, E.T., Grieveson, P., and Darken, L.S., 1963, “Enhancement of Diffusion-Limited Rates of Vaporization of Metals," *J. Phys. Chem*., vol. 67, August, pp. 1647-54.
89. Miedema, A.R., de Chatel, P.F., de Boer, F.R., 1980, “Cohesion in Alloys - Fundamentals of a Semi-Empirical Model," *Physica*, vol. 100B, pp. 1-28.
90. Ferro, R., Cacciamani, G., Saccone, A., and Borzone, G., “Systematics of Lanthanide and Actinide Compound Formation: Remarks on the Americium Alloying Behaviour," *Journal of Alloys and Compounds*, vol. 320, pp. 326-40.
91. Ogawa, T., Ohmichi, T., Maeda, A., Arai, Y., and Suzuki, Y., 1995, “Vaporization Behaviour of (Pu, Am)N," *Journal of Alloys and Compounds*, vol 224, pp. 55-59.

7. Publications and Presentations

Tan, T., Clarksean, R., Chen, Y., Hsieh, S., and Meyer, M., 2004, "Analyzing a Process for Casting Volatile Actinides," *6th International Topical Meeting on Nuclear Reactor Thermal Hydraulics, Operations and Safety*, Nara, Japan, October 4-8, (submitted).

Tan, T., Clarksean, R., Chen, Y., Hsieh, S., and Meyer, M, 2004, "Numerical Simulation of an Induction Heating Process in an Induction Skull Melting Furnace," *ICHMT International Symposium on Advances in Computational Heat Transfer*, April 19-24, Norway (accepted).

Tan, T., Clarksean, R., Chen, Y., Hsieh, S., and Meyer, M., 2004, "Simulation of the Casting Process for Melt Casting a Metallic Fuel Pin," submitted to *Nuclear Engineering and Design – under review*.

Taide, T., Clarksean, R., Chen, Y., Hsieh, S., and Meyer, M., 2004, "Simulating the Casting Process for Melt Casting a Metallic Fuel Pin," *12th International Conference on Nuclear Engineering (ICONE)*, Arlington, Virginia (Washington, D.C.), USA April 25-29.

Taide, T., Clarksean, R., Chen, Y., Hsieh, S., and Meyer, M., 2004, "Simulating the Induction Heating Process in an Induction Skull Melter for Casting Metallic Fuel," *12th International Conference on Nuclear Engineering (ICONE)*, Arlington, Virginia (Washington, D.C.), USA April 25-29.

Tan, T., Clarksean, R., Chen, Y., Pepper, D., and Meyer, M., 2003, "Simulation and Analysis for Melt Casting a Metallic Fuel Pin Incorporating Volatile Actinides" *International Mechanical Engineering Congress and Exposition*, Washington, D.C., November 16-21.

Wu, X., Clarksean, R., Chen, Y., Pepper, D., and Meyer, M.K., 2002, "An Analysis of the Melt Casting of Metallic Fuel Pins," *International Mechanical Engineering Congress and Exposition*, New Orleans, November 17-22.

Wu, X, Clarksean, R., Chen, Y., and Pepper, D., 2002, "Design and Analysis for Melt Casting Metallic Fuel Pins Incorporating Volatile Actinides," *International Youth Nuclear Congress,* Daejeon, Korea, April 16-20.

Wu, X., Clarksean, R., and Chen, Y., 2002, "Design and Analysis for Melt Casting Metallic Fuel Pins Incorporating Volatile Actinides," *International Congress on Advanced Nuclear Power Plants*, embedded topical meeting at the ANS Summer Meeting, Hollywood, Florida, June 9-13.

Presentations

Clarksean, R., Chen, Y., and Hsieh, S., 2004, "Modeling Induction Heating with FIDAP: Equations, Procedures, and Examples," FIDAP Users' Group Meeting, Dearborn, Michigan, June 8-9.

Clarksean, R., Tan, T., Chen, Y., Meyer, M.K., 2003, "Modeling Fill and Solidification of an Injection Casting Process," FIDAP Users' Group Meeting, Evanston, Illinois, June 10-11.

Tan, T., Clarksean, R., Chen, Y., Hseih, H.T., and Pepper, D., 2003, "Numerically Simulating the Solidification Process of a Melt Casing Metallic Fuel Pin Mold Using FIDAP," 2003 ANS Student Conference, April 2-5, Berkeley, California.

Royyuru, H.P., Sun, L., Chen, Y., Hseih, H.T., Clarksean, R.L., and Pepper, D., 2003 "Development of an Optimization Systems Engineering Model for Spent Fuel Extraction Process," 2003 ANS Student Conference, April 2-5, Berkeley, California.

Yitung Chen, Randy Clarksean, and Darrell W. Pepper, 2002, "Design and Analysis for Melt Casting Metallic Fuel Pins Incorporating Volatile Actinides," *Argonne National Laboratory-West Transmuter Fuel Development Workshop*, Idaho Fall, September 11-12

Clarksean, R., and Chen, Y., 2002, "Calculating an Induction Heating Field with FIDAP," FIDAP Users' Group Meeting, Evanston, Illinois, June.

Clarksean, R., Chen, Y., and Horner, M., 2002, "An Analysis of Injection Casting into Chill Molds," FIDAP Users' Group Meeting, Evanston, Illinois, June.

Y. Chen, R. Clarksean, and X. Wu, 2001, "Examination of Casting Furnace Designs for Inclusion of Am in Metallic Fuel," presented at the ANL Transmuter Fuel Development Workshop, Idaho Falls, ID., November 20.

Wu, X, Clarksean, R., Chen, Y., and Pepper, D. 2001, "Design and Analysis for Melt Casting Metallic Fuel Pins Incorporating Volatile Actinides," presented at the American Nuclear Society (ANS) Conference in Reno, Nevada, November 10-12.

Sun, L., Chen, Y., Clarksean, R., and Pepper, D., 2001, "Development of a System Engineering Model of the Chemical Separations Process," Lijian Sun, Yitung Chen, Randy Clarksean, and Darrell Pepper, presented at the American Nuclear Society (ANS) Conference in Reno, Nevada, November 10-12.

Munaga, S., Chen, Y., Clarksean, R., and Pepper, D., 2001, "Improvement, Automation, and Modernization of AMUSE Code for the Chemical Separations Process," presented at the American Nuclear Society (ANS) Conference in Reno, Nevada, November 10-12.

Appendix I – Nomenclature

Induction Heating Model :

$\dot{Q}'''$	time average power deposition rate (w/ m^3)
r	radial coordinate (m)
K	(m^{-1}) K=1/r
Jo	current density in the coils (amp/ m^2)
J_i (0)	induced current density at the load surface (amp/ m^2)
J_i (x)	induced current density of the load at distance x from the skin (amp/ m^2)
x	the distance from the skin of the load (m)
δ	the skin depth or the current penetration depth (m)
f	current frequency (Hz)
ω	angular frequency (Hz), ω=2πf
μ	magnetic permeability (Wb/a-m)
σ	electric conductivity (mhos/m)
C, S	2 real and complex components of Q, they are functions of location
d	the distance between the coils' surfaces, d_0=3mm
b	the distance between the coils and the crucible, b_0= 10mm
n	coils group number
C_p	specific heat (J/kg·K)
C_{eqiv}	equivalent specific heat (J/Kg·K)
H	enthalpy (J)
k	thermal conductivity (W/m·K)
k_l	thermal conductivity of the molten feedstock (W/m·K)
k_{mt}	thermal conductivity of the unmelted feedstock (W/m·K)
δ_l	a large but infinite value for the modified Dirac delta function
L	latent heat per unit mass (J/g)
n^*	normal vector to the solidification front
ρ	density of the molten feedstock flow (kg/m^3)

ρ_s density of solid (kg/m^3)

T temperature (^0C)

T_l temperature of liquid (^0C)

T_s temperature of solid (^0C)

T_m temperature of the melting point of the materials (^0C)

ΔT a small temperature difference across which phase change occurs (^0C)

u^* interface velocity(m/s) (speed at which solidification front moves into the melt)

μ viscosity of material ($N \cdot s/m^2$)

μ_0 viscosity of the material in liquid phase ($N \cdot s/m^2$)

μ_∞ viscosity of the material in solid phase, has a large but finite value ($N \cdot s/m^2$)

$\eta(T-T_m)$ unit function, 1 if T greater than or equal to T_m, and 0 if less than T_m

$\delta(T-T_m)$ Dirac delta function, infinite if T equal to T_m, and 0 if T not equal to T_m

$\delta^*(T-T_m, \Delta T)$ modified Dirac delta function, has a large but finite value over the temperature range ($T_m-\Delta T/2$) to T_m and is zero outside this range.

Casting model:

∇ Gradient operator

$\nabla \cdot$ Divergence operator

ρ Density of the molten metal (kg/m^3)

ρ_s Density of solid (solidified metal) (kg/m^3)

ρ_{mold} Density of the mold material

τ Shear stress (N/m^2)

τ_w Wall shear stress (N/m^2)

μ Viscosity ($N \cdot s/m^2$)

$\boldsymbol{\mu_0}$ viscosity of the material in liquid phase ($N \cdot s/m^2$)

μ_∞ A large but finite value for numerical simulation of solidified material ($N \cdot s/m^2$)

$\eta(T-T_m)$ Unit function, equals 1 if T greater than or equal to T_m, and 0 if less than Tm

$\delta(T-T_m)$ Dirac delta function, infinite if T equal to T_m, and 0 if T not equal to T_m

$\delta^*(T-T_m, \Delta T)$ Modified Dirac delta function, has a large but finite value (δ_∞) over the temperature range ($T_m-\Delta T/2$) to ($T_m-\Delta T/2$) and is zero outside this range.

δ_∞ A large but finite value for the modified Dirac delta function

C_p Specific heat (J/kg·K)

$C_{p.mold}$ Specific heat of the mold material (J/kg·K)

$C_{p.melt}$ Specific heat of the melt (J/kg·K)

C_{eqiv} Equivalent specific heat (J/kg·K)

d Internal pipe diameter (m)

F Indicator function of fluid volume

H Enthalpy (J)

k Thermal conductivity (W/m·K)

k_l Thermal conductivity of the melt materials in liquid state (W/m·K)

k_{mt} Thermal conductivity of the melt materials in solid state (W/m·K)

L Latent heat of the melt (J/kg)

l Length of the mold (m)

p Pressure (N/m^2)

$\hat{p}$ Effective pressure, $p+\rho gh$ (N/m^2)

Q Heat (J)

Q_{min} The minimum heat must be absorbed by the mold for the phase change of the melt in one pin (J)

r_{pin} Radius of a metallic fuel pin (inner radius of a mold, m)

r_{mold} Outer radius of a mold (m)

R_e Reynolds number

t Time (s)

T Temperature (^0C)

T_{melt} Temperature of the melt (^0C)

T_{pre} Preheated temperature of a mold (^0C)

T_l Temperature of liquid (molten metal) (^0C)

T_s Temperature of solid (solidified metal) (^0C)

T_m Melting point (^0C)

ΔT a small temperature difference across which phase change occurs (0C)

$\vec{u}$ Velocity of the melt flow (m/s)

u^* Interface moving velocity (m/s) (speed at which solidification front moves into the melt)

Appendix II – Finite Element Method

Many numerical techniques for modeling systems of partial differential equations are in use today, for example, finite difference method, finite element method and finite volume method. Through the use of these numerical techniques approximate solutions are obtained for problems in physics and engineering.

Comparing with other methods, finite element methods can utilize unstructured meshes, since the solution algorithm and the process of mesh generation are uncoupled. This decoupling permits any arbitrarily shaped region to be discretized (Lohner et al., 1986). Also it enables local refinement of the mesh to occur independently of the solution algorithm. For these reasons, the finite element method has been chosen to model the governing equations. [51-53]

The objective of the finite-element method (FEM) is to reduce the continuum problem (infinite number of degrees of freedom) to a discrete problem (finite number of degrees of freedom) described by a system of algebraic equations. As mentioned before, the fluid is considered to be an incompressible Newtonian fluid. For simplicity we shall show the finite element techniques on the discretization of the continuity and momentum equations using linear triangular elements. For purposes of clarity, this chapter will restrict itself to a discussion of determining the two-dimensional velocity and pressure field in the metallic fuel pin mold. Here the flow field at the entrance of the mold is assumed to be fully developed.

The continuity equation for an incompressible fluid is given by:

$$\frac{\partial u}{\partial x} + \frac{\partial v}{\partial y} = 0 \tag{II-1}$$

where u and v are components of the fluid velocity at any point (x, y). The Navier-Stokes equations in the x and y directions are given by

$$\rho \left(u \frac{\partial u}{\partial x} + v \frac{\partial u}{\partial y} \right) = - \frac{\partial p}{\partial x} + \mu \left(\frac{\partial^2 u}{\partial x^2} + \frac{\partial^2 u}{\partial y^2} \right) + F_x \tag{II-2}$$

$$\rho \left(u \frac{\partial v}{\partial x} + v \frac{\partial v}{\partial y} \right) = - \frac{\partial p}{\partial y} + \mu \left(\frac{\partial^2 v}{\partial x^2} + \frac{\partial^2 v}{\partial y^2} \right) + F_y \tag{II-3}$$

where p is the pressure, ρ is the fluid density, μ is the absolute viscosity, F_x and F_y are the body forces per unit volume in the x and y directions, respectively.

The convective acceleration terms on the left hand side of Equations (II-2) and (II-3) make the problem to be solved nonlinear. The region to be analyzed may be discretized in the usual manner with triangular or rectangular elements. The goal is to determine the nodal values of the pressure and the velocity components, since the formulation is to be based on the so-called primitive variables.

If the Galerkin method is applied to Equation (II-1), we get

$$\int_{A^e} N^T \left(\frac{\partial u}{\partial x} + \frac{\partial v}{\partial y}\right) h dx dy = 0 \tag{II-4}$$

where the thickness h is introduced so that each term in Equation (II-4) has dimensions of volume per unit time (i.e. , a volumetric flow rate). For convenience, h can be taken to be unity. Let us assume

$$u = N a_u^e \tag{II-5}$$

and

$$v = N a_v^e \tag{II-6}$$

where a_u^e and a_v^e are given by

$$a_u^e = [u_i \;\; u_j \;\; u_k]^T \tag{II-7}$$

and

$$a_v^e = [v_i \;\; v_j \;\; v_k]^T \tag{II-8}$$

for the triangular element. In Equations (II-4) and (II-5), u_i, u_j, u_k are the x components of the velocity at nodes i, j, and k etc.

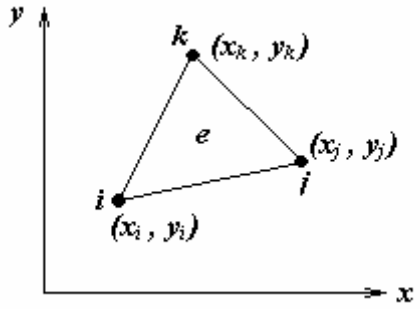

Figure 83 Three-node triangular element showing local nodal coordinates i, j, k

where the shape functions N for the linear triangle are determined as

$$N_i(x,y) = m_{11} + m_{21}x + m_{31}y \tag{II-9}$$

$$N_j(x,y) = m_{12} + m_{22}x + m_{32}y \tag{II-10}$$

$$N_k(x,y) = m_{13} + m_{23}x + m_{33}y \tag{II-11}$$

where

$$m_{11} = (x_j y_k - x_k y_j)/2A \quad m_{21} = (y_j - y_k)/2A \quad m_{31} = (x_k - x_j)/2A \tag{II-12}$$

$$m_{12} = (x_k y_i - x_j y_k)/2A \quad m_{22} = (y_k - y_i)/2A \quad m_{32} = (x_i - x_k)/2A \tag{II-13}$$

$$m_{13} = (x_i y_j - x_j y_i)/2A \quad m_{23} = (y_i - y_j)/2A \quad m_{33} = (x_j - x_i)/2A \tag{II-14}$$

and

$$A = \tfrac{1}{2}\det\begin{bmatrix} 1 & x_i & y_i \\ 1 & x_j & y_j \\ 1 & x_k & y_k \end{bmatrix} = \textit{area of triangle ijk} \tag{II-15}$$

Since a_u^e and a_v^e are independent of x and y, Equation (II-4) can be written in the form

$$K_u^e a_u^e + K_v^e a_v^e = 0 \tag{II-16}$$

where

$$K_u^e = \int_{A^e} N^T \frac{\partial N}{\partial x} h dx dy \tag{II-17}$$

and

$$K_v^e = \int_{A^e} N^T \frac{\partial N}{\partial y} h dx dy \tag{II-18}$$

Let us now apply the Galerkin method to Equation (II-12) by writing

$$\int_{A^e} N^T [\rho (u \frac{\partial u}{\partial x} + v \frac{\partial u}{\partial y}) + \frac{\partial p}{\partial x} - \mu (\frac{\partial^2 u}{\partial x^2} + \frac{\partial^2 u}{\partial y^2}) - F_x] h dx dy = 0 \tag{II-19}$$

Note that each term in Equation (II-19) has units of force. The Green-Gauss theorem may be applied in the usual manner to the two terms involving second-order derivatives. However, the integrals around the element boundary (over C^e) need not be considered further because the

velocity components are generally prescribed on the global boundary. The boundary integral terms are related to the shear stresses (which are not generally prescribed). Noting Equations (II-5) and (II-6) and representing the pressure p over the element by

$$p = Na^{e}_{p} \tag{II-20}$$

Equation (II-19) may be written in the form

$$(K^{e}_{uu} + K^{e}_{vu} + K^{e}_{ux} + K^{e}_{uy})a^{e}_{u} + K^{e}_{px}a^{e}_{p} = f^{e}_{x} \tag{II-21}$$

where

$$K^{e}_{uu} = \int_{A^e} N^{T} \rho Na^{e}_{u} \frac{\partial N}{\partial x} hdxdy \tag{II-22}$$

$$K^{e}_{vu} = \int_{A^e} N^{T} \rho Na^{e}_{v} \frac{\partial N}{\partial y} hdxdy \tag{II-23}$$

$$K^{e}_{ux} = \int_{A^e} \frac{\partial N}{\partial x}^{T} \mu \frac{\partial N}{\partial x} hdxdy \tag{II-24}$$

$$K^{e}_{uy} = \int_{A^e} \frac{\partial N}{\partial y}^{T} \mu \frac{\partial N}{\partial y} hdxdy \tag{II-25}$$

$$K^{e}_{px} = \int_{A^e} N^{T} \frac{\partial N}{\partial x} hdxdy \tag{II-26}$$

and

$$f^{e}_{x} = \int_{A^e} N^{T} f_x hdxdy \tag{II-27}$$

In a similar fashion, it can be shown that if the Galerkin method is applied to Equation (II-3), the result is

$$(K^{e}_{uv} + K^{e}_{vv} + K^{e}_{vx} + K^{e}_{vy})a^{e}_{v} + K^{e}_{py}a^{e}_{p} = f^{e}_{y} \tag{II-28}$$

where

$$K^{e}_{uv} = K^{e}_{uu} = \int_{A^e} N^{T} \rho Na^{e}_{u} \frac{\partial N}{\partial x} hdxdy \tag{II-29}$$

$$K^{e}_{vu} = K^{e}_{vu} = \int_{A^e} N^{T} \rho Na^{e}_{v} \frac{\partial N}{\partial y} hdxdy \tag{II-30}$$

$$K^{e}_{vx} = K^{e}_{ux} = \int_{A^e} \frac{\partial N}{\partial x}^{T} \mu \frac{\partial N}{\partial x} h dx dy \tag{II-31}$$

$$K^{e}_{vy} = K^{e}_{uy} = \int_{A^e} \frac{\partial N}{\partial y}^{T} \mu \frac{\partial N}{\partial y} h dx dy \tag{II-32}$$

$$K^{e}_{py} = \int_{A^e} N^{T} \frac{\partial N}{\partial y} h dx dy \tag{II-33}$$

and

$$f^{e}_{y} = \int_{A^e} N^{T} f_y h dx dy \tag{II-34}$$

There are two different ways in which the assemblage step maybe performed. The first step in both procedures is to write Equations (II-16), (II-21), and (II-28) in the following partitioned matrix form:

$$\begin{bmatrix} K^{e}_{u} & K^{e}_{v} & 0 \\ K^{e}_{uu}+K^{e}_{vu}+K^{e}_{ux}+K^{e}_{uy} & 0 & K^{e}_{px} \\ 0 & K^{e}_{uv}+K^{e}_{vv}+K^{e}_{vx}+K^{e}_{vy} & K^{e}_{py} \end{bmatrix} \begin{bmatrix} a^{e}_{u} \\ a^{e}_{v} \\ a^{e}_{p} \end{bmatrix} = \begin{bmatrix} 0 \\ f^{e}_{x} \\ f^{e}_{y} \end{bmatrix} \tag{II-35}$$

In the first method of assemblage, the individual terms in Equation (II-35) are assembled such that the vector of nodal unknowns is given by

$$a = [u_1 \; u_2 \; \ldots \; u_n \vdots v_1 \; v_2 \; \ldots \; v_n \vdots p_1 \; p_2 \; \ldots \; p_n]^T \tag{II-36}$$

where n nodes are assumed in the discretization of the region being analyzed. This type of assemblage results in a significantly increased bandwidth of the assemblage system equations. Therefore, a more practical method of assemblage is needed, and one such method is presented below.

Let us denote the submatrices and subvectors in Equation (II-37) as follows:

$$\begin{bmatrix} K^{11} & K^{12} & K^{13} \\ K^{21} & K^{22} & K^{23} \\ K^{31} & K^{32} & K^{33} \end{bmatrix} \begin{bmatrix} a^{e}_{u} \\ a^{e}_{v} \\ a^{e}_{p} \end{bmatrix} = \begin{bmatrix} f^{1} \\ f^{2} \\ f^{3} \end{bmatrix} \tag{II-37}$$

Note the use of the numerical superscripts to indicate the relative position of each submatrix and subvector in Equation (II-37). Let us now use subscripts to indicate the entries within each submatrix. For example, if the three-node triangular element is used, let us write

$$K_u^e = K^{11} = \begin{bmatrix} K_{11}^{11} & K_{12}^{11} & K_{13}^{11} \\ K_{21}^{11} & K_{22}^{11} & K_{23}^{11} \\ K_{31}^{11} & K_{32}^{11} & K_{33}^{11} \end{bmatrix} \tag{II-38}$$

and

$$f_x^e = f^2 = \begin{bmatrix} f_1^2 \\ f_2^2 \\ f_3^2 \end{bmatrix} \tag{II-39}$$

and so forth. Note that K^{13}, K^{22}, K^{31}, are 3×3 null matrices and f^1 is a 3×1 null vector. Let us now do a mini-assemblage such that the vector of nodal unknowns on an element basis is given by

$$a^e = [u_i \;\; v_i \;\; p_i \vdots u_j \;\; v_j \;\; p_j \vdots u_k \;\; v_k \;\; p_k]^T \tag{II-40}$$

Using the nomenclature illustrated by Equations (II-39-40), Equation (II-35) may be written

$$\begin{bmatrix} K_{11}^{11} & K_{11}^{12} & K_{11}^{13} & K_{12}^{11} & K_{12}^{12} & K_{12}^{13} & K_{13}^{11} & K_{13}^{12} & K_{13}^{13} \\ K_{11}^{21} & K_{11}^{22} & K_{11}^{23} & K_{12}^{21} & K_{12}^{22} & K_{12}^{23} & K_{13}^{21} & K_{13}^{22} & K_{13}^{23} \\ K_{11}^{31} & K_{11}^{32} & K_{11}^{33} & K_{12}^{31} & K_{12}^{32} & K_{12}^{33} & K_{13}^{31} & K_{13}^{32} & K_{13}^{33} \\ K_{21}^{11} & K_{21}^{12} & K_{21}^{13} & K_{22}^{11} & K_{22}^{12} & K_{22}^{13} & K_{23}^{11} & K_{23}^{12} & K_{23}^{13} \\ K_{21}^{21} & K_{21}^{22} & K_{21}^{23} & K_{22}^{21} & K_{22}^{22} & K_{22}^{23} & K_{23}^{21} & K_{23}^{22} & K_{23}^{23} \\ K_{21}^{31} & K_{21}^{32} & K_{21}^{33} & K_{22}^{31} & K_{22}^{32} & K_{22}^{33} & K_{23}^{31} & K_{23}^{32} & K_{23}^{33} \\ K_{31}^{11} & K_{31}^{12} & K_{31}^{13} & K_{32}^{11} & K_{32}^{12} & K_{32}^{13} & K_{33}^{11} & K_{33}^{12} & K_{33}^{13} \\ K_{31}^{21} & K_{31}^{22} & K_{31}^{23} & K_{32}^{21} & K_{32}^{22} & K_{32}^{23} & K_{33}^{21} & K_{33}^{22} & K_{33}^{23} \\ K_{31}^{31} & K_{31}^{32} & K_{31}^{33} & K_{32}^{31} & K_{32}^{32} & K_{32}^{33} & K_{33}^{31} & K_{33}^{32} & K_{33}^{33} \end{bmatrix} \begin{bmatrix} u_i \\ v_i \\ p_i \\ u_j \\ v_j \\ p_j \\ u_k \\ v_k \\ p_k \end{bmatrix} = \begin{bmatrix} f_1^1 \\ f_1^2 \\ f_1^3 \\ f_2^1 \\ f_2^2 \\ f_2^3 \\ f_3^1 \\ f_3^2 \\ f_3^3 \end{bmatrix} \tag{II-41}$$

The assemblage of Equation (II-41) may now be done in thee usual manner such that the vector of nodal unknowns is given by

$$a = [u_1 \;\; v_1 \;\; p_1 \vdots u_2 \;\; v_2 \;\; p_2 \vdots \cdots \vdots u_n \;\; v_n \;\; p_n]^T \tag{II-42}$$

where again n nodes are assumed in the discretization of the region being analyzed. The assemblage system equations are unsymmetrical. This system of equations can be solved using one of matrix solving techniques available in FIDAP.

The integrals are evaluated numerically using Gauss-Legendre quadrature rules (Segerlind, 1975). For the linear triangle, a four-point integration rule is used.

For four-noded bilinear rectangular element case, a_u^e, a_v^e and a_p^e are given by three 4×1 matrices instead of 3×1 matrices as shown in Equation (II-7), (II-8) and (II-20). The procedures will be similar whereas there are more nodes involved in the calculation. Each element is bounded by four nodes. The elements may not overlap, but may share nodes with adjacent elements. The wide variety of element shapes across the solution domain makes determination of the shape functions and numerical integration tedious. To simplify these processes, a transformation from the Cartesian coordinate system to the so-called "natural" coordinate system is employed (see Figure 84). In the natural coordinate system, all physical dimensions (ξ, η) of the isoparametric elements lie within the range of –1 to 1.

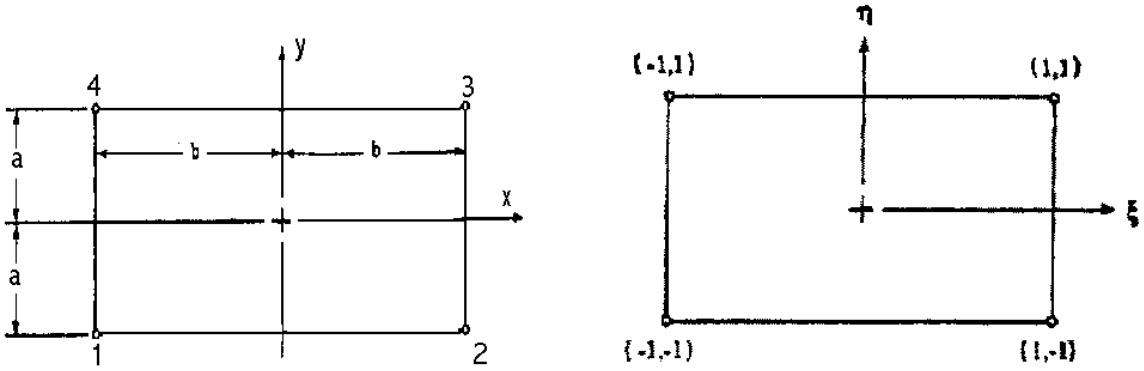

Figure 84 Coordinate transformation to natural coordinates

In the natural coordinate system, the shape functions can easily be written as:

$$\begin{bmatrix} N_1 \\ N_2 \\ N_3 \\ N_4 \end{bmatrix} = \frac{1}{4}\begin{bmatrix} (1-\xi)(1-\eta) \\ (1+\xi)(1-\eta) \\ (1+\xi)(1+\eta) \\ (1-\xi)(1+\eta) \end{bmatrix} \tag{II-43}$$

The derivatives of the shape functions are obtained using the chain rule:

$$\frac{\partial N_i}{\partial \xi} = \frac{\partial N_i}{\partial x}\frac{\partial x}{\partial \xi} + \frac{\partial N_i}{\partial y}\frac{\partial y}{\partial \xi} \tag{II-44}$$

$$\frac{\partial N_i}{\partial \eta} = \frac{\partial N_i}{\partial x}\frac{\partial x}{\partial \eta} + \frac{\partial N_i}{\partial y}\frac{\partial y}{\partial \eta} \tag{II-45}$$

Equation (II-44-45) can be rewritten in matrix form as:

$$\begin{bmatrix} \frac{\partial N_i}{\partial \xi} \\ \frac{\partial N_i}{\partial \eta} \end{bmatrix} = \begin{bmatrix} \frac{\partial x}{\partial \xi} & \frac{\partial y}{\partial \xi} \\ \frac{\partial x}{\partial \eta} & \frac{\partial y}{\partial \eta} \end{bmatrix} \begin{bmatrix} \frac{\partial N_i}{\partial x} \\ \frac{\partial N_i}{\partial y} \end{bmatrix} \tag{II-46}$$

or

$$\begin{bmatrix} \frac{\partial N_i}{\partial \xi} \\ \frac{\partial N_i}{\partial \eta} \end{bmatrix} = J \begin{bmatrix} \frac{\partial N_i}{\partial x} \\ \frac{\partial N_i}{\partial y} \end{bmatrix} \tag{II-47}$$

where J is the Jacobian matrix. Similarly, the derivatives of any computational variable can be transformed into the natural coordinate system via the relation:

$$\begin{bmatrix} \frac{\partial}{\partial \xi} \\ \frac{\partial}{\partial \eta} \end{bmatrix} = J \begin{bmatrix} \frac{\partial}{\partial x} \\ \frac{\partial}{\partial y} \end{bmatrix} \tag{II-48}$$

When dealing with isoparametric elements, it is sometimes convenient to express the Jacobian in terms of the shape functions defined in equation (II-49) as follows:

$$J = \begin{bmatrix} \sum \frac{\partial N_i}{\partial \xi} x_i & \sum \frac{\partial N_i}{\partial \xi} y_i \\ \sum \frac{\partial N_i}{\partial \eta} x_i & \sum \frac{\partial N_i}{\partial \eta} x_i \end{bmatrix} \tag{II-49}$$

In the transfer back to Cartesian coordinates, the inverse of equation (II-49) is used.

$$\begin{bmatrix} \frac{\partial}{\partial x} \\ \frac{\partial}{\partial y} \end{bmatrix} = J^{-1} \begin{bmatrix} \frac{\partial}{\partial \xi} \\ \frac{\partial}{\partial \eta} \end{bmatrix} \tag{II-50}$$

The inverse of the Jacobian equation (II-50) is:

$$J^{-1} = \begin{bmatrix} \frac{\partial x}{\partial \xi} & \frac{\partial x}{\partial \eta} \\ \frac{\partial y}{\partial \xi} & \frac{\partial y}{\partial \eta} \end{bmatrix} \tag{II-51}$$

Although many numerical methods exist for evaluating integrals, Gauss-Legendre quadrature is a very appropriate algorithm to implement. The finite element method employed for this study makes use of the transformation to a normalized computational domain where all physical dimensions (ξ, η) lie within the range of -1 to 1. Since the limits of integration used for Gauss-Legendre quadrature also range from -1 to 1, no change in limits is required.

Integrals in this study take the form of

$$\int_{-a}^{a}\int_{-b}^{b} F(x,y)dxdy = \int_{-1}^{1}\int_{-1}^{1} f(\xi,\eta)|J|d\xi d\eta \tag{II-52}$$

Using Gauss-Legendre quadrature to evaluate this integral yields (Pepper and Heinrich, 1992):

$$\int_{-1}^{1}\int_{-1}^{1} f(\xi,\eta)|J|d\xi d\eta \cong \sum_{i=1}^{N}\sum_{j=1}^{N} W_i W_j f(\xi_i,\eta_j)|J|(\xi_i,\eta_j) \tag{II-53}$$

where, W_i and W_j are the Gauss weights of integration evaluated at the Gauss points ξ_i and η_j. With N Gauss points, we can integrate exactly a polynomial of degree 2N-1. Thus, if 2×2 quadrature is chosen, the double integral (II-53) will be integrated exactly with:

$$W_i = W_j = 1.0 \tag{II-54}$$

$$\xi_i = \eta_j = \pm\frac{1}{\sqrt{3}} \tag{II-55}$$

After integrating each terms of the Equation of (II-18), similarly the unsymmetrical assemblage system equation can be solved using matrix solving techniques available in FIDAP.

FIDAP uses the penalty function algorithm to solve the above set of continuity and momentum equations. The continuity equation

$$\frac{\partial u}{\partial x} + \frac{\partial v}{\partial y} = 0 \tag{II-56}$$

is replaced by its analogue to introduce pressure into the right side of the equation in the form

$$\frac{\partial u}{\partial x} + \frac{\partial v}{\partial y} = -\varepsilon\, p \tag{II-57}$$

where ε is the penalty parameter equal to a very large number.

In practical computations, the selection of the value of the penalty parameter ε can be of crucial importance. To get an accurate solution, the penalty parameter must be chosen small enough to approximate incompressibility well, yet large enough to comply with the machine accuracy. Numerical studies reveal that for floating point word lengths of 60 - 64 bits, an appropriate choice of ε is 10^{-6}. [54]

Appendix III – Development of a Model for Induction Heating

The development of this derivation was taken from References [31, 41, 42, 44-46]. The development leads to a set of equations that can be used to solve for the amount of induction heating within a conductor.

The following equations are a version of Maxwell's equations. Details of the initial assumptions to reach this state can be found in References [31] and [44].

$$\nabla \times E = -\frac{\partial B}{\partial t} \tag{A-1}$$

$$\nabla \times B = \mu J \tag{A-2}$$

$$\nabla \bullet B = 0 \tag{A-3}$$

$$\nabla \bullet E = 0 \tag{A-4}$$

Where

J = free charge current density vector (amp/ m^2)
E = electric field intensity (V/m)
H = magnetic field intensity (amp/m)
B = magnetic flux density (webers/ m2)
ρ = free charge density (coulombs/ m^3)
D = electric flux density vector (coulombs/ m^2)
μ = permeability (Wb/a-m)
σ= conductivity (mhos/m)
J is in defined in conductors to be

$$J = \sigma E \tag{A-5}$$

In a conductor, we can substitute this relationship into Equation (A-2) to give us

$$\nabla \times B = \mu J = \mu(\sigma E) \tag{A-6}$$

Then taking the divergence of this relationship.

$$\nabla \bullet (\nabla \times B) = \nabla \bullet (\mu\sigma E) \tag{A-7}$$

$$0 = \mu\sigma (\nabla \bullet E) \tag{A-8}$$

which implies $\nabla \bullet E = 0$, this is same as Equation (A-4)

Going one step farther with the assumption of constant σ, we have

$$\nabla \bullet J = \nabla \bullet (\sigma E) = \sigma (\nabla \bullet E) \tag{A-9}$$

So

$$\nabla \bullet J = 0 \tag{A-10}$$

Next, we introduce a vector potential A and a scalar potential V as defined here.

$$B \equiv \nabla \times A \tag{A-11}$$

$$E \equiv -\nabla V - \frac{\partial A}{\partial t} \tag{A-12}$$

Substituting in the new vector potential A in Equation (A-2) and then by identity we have

$$\nabla \times (\nabla \times A) = \mu J \tag{A-13}$$

$$\nabla (\nabla \bullet A) - \nabla^2 A = \mu J \tag{A-14}$$

Recalling from Equation (A-4) that $\nabla \bullet E = 0$ and substituting in the new scalar potential for E gives

$$\nabla \bullet (-\nabla V - \frac{\partial A}{\partial t}) = 0 \tag{A-15}$$

$$-\nabla^2 V - \frac{\partial (\nabla \bullet A)}{\partial t} = 0 \tag{A-16}$$

$$\nabla^2 V = -\frac{\partial (\nabla \bullet A)}{\partial t} \tag{A-17}$$

Requiring the vector potential A to be conserved

$$\nabla \bullet A = 0 \tag{A-18}$$

This gives us from Equation (A-14)

$$\nabla^2 A = -\mu J \tag{A-19}$$

and from Equation (A-17) we have

$$\nabla^2 V = 0 \tag{A-20}$$

In the absence of free charges, it is appropriate to set

$$V = 0 \tag{A-21}$$

which satisfies Equation (A-20). And then Equation (A-12) gives us

$$E = -\frac{\partial A}{\partial t} \tag{A-22}$$

Knowing Equation (A-19) and then solving this equation for A would allow the determination of B from Equation (A-11). E could also be determined from Equation (A-22). At present, we do not really need B because we are seeking the power dissipated in the crucible, which can be determined from

$$P = J \bullet E \tag{A-23}$$

Now, if J were independent of time and substituting Equation (A-22) into Equation (A-5) gives

$$J = -\sigma \frac{\partial A}{\partial t} \tag{A-24}$$

Equation (A-19) would imply that A≠ F(t). In addition, this would imply that $E = -\frac{\partial A}{\partial t} = 0$, which can not be true because if this was true there would be no induction heating. But since we have alternating current power, E ≠0.

Taking the Equation (A-19) for a conductor and rearranging it gives

$$J = -\frac{1}{\mu}\nabla^2 A \tag{A-25}$$

Thus considering Equations (A-24) and (A-25)

$$\nabla^2 A = \sigma\mu \frac{\partial A}{\partial t} \tag{A-26}$$

In an insulator (σ = 0)

$$\nabla^2 A = 0 \tag{A-27}$$

In the coil, we assume that J is known (prescribed and time varying) and satisfies Equations (A-19): $\nabla^2 A = -\mu J$.

Up to this point, the solution has been discussed in general Cartesian coordinates. If we were to assume axisymmetric behavior of the fields, the equations can be simplified even further. The coordinate system would depend on r, ϕ, and z. Assuming that the relevant quantities do not vary with ϕ allows us to define A as

$$A = e_r A_r(r,z,t) + e_\phi A_\phi(r,z,t) + e_z A_z(r,z,t) \tag{A-28}$$

Now, going back to the coil equation (Equation (A-19)) and recalling that A is a vector in cylindrical coordinates gives us

$$\frac{\partial}{\partial r}\left(\frac{1}{\partial r}\frac{\partial}{\partial r}(rA_r)\right) + \frac{1}{r^2}\frac{\partial^2 A_r}{\partial \phi^2} - \frac{2}{r^2}\frac{\partial A_\phi}{\partial \phi} + \frac{\partial^2 A_r}{\partial z^2} = -\mu J_r \tag{A-29}$$

$$\frac{\partial}{\partial r}\left(\frac{1}{\partial r}\frac{\partial}{\partial r}(rA_\phi)\right) + \frac{1}{r^2}\frac{\partial^2 A_\phi}{\partial \phi^2} + \frac{2}{r^2}\frac{\partial A_r}{\partial \phi} + \frac{\partial^2 A_\phi}{\partial z^2} = -\mu J_\phi \tag{A-30}$$

$$\frac{\partial}{\partial r}\left(r\frac{\partial A_z}{\partial r}\right) + \frac{1}{r^2}\frac{\partial^2 A_z}{\partial \phi^2} + \frac{\partial^2 A_z}{\partial z^2} = -\mu J_z \tag{A-31}$$

Eliminating all of the derivatives with respect to ϕ leaves

$$\frac{\partial}{\partial r}\left(\frac{1}{\partial r}\frac{\partial}{\partial r}(rA_r)\right) + \frac{\partial^2 A_r}{\partial z^2} = -\mu J_r \tag{A-32}$$

$$\frac{\partial}{\partial r}\left(\frac{1}{\partial r}\frac{\partial}{\partial r}(rA_\theta)\right) + \frac{\partial^2 A_\phi}{\partial z^2} = -\mu J_\phi \tag{A-33}$$

$$\frac{\partial}{\partial r}\left(r\frac{\partial A_z}{\partial r}\right) + \frac{1}{r^2}\frac{\partial^2 A_z}{\partial \phi^2} + \frac{\partial^2 A_z}{\partial z^2} = -\mu J_z \tag{A-34}$$

By neglecting the helicity (pitch) of the coils as well as 3D effects, along with appropriate boundary conditions gives $A_r = 0$ and $A_z = 0$. This reduces the previous set of equations to

Equation (A-33) only: $\frac{\partial}{\partial r}\left(\frac{1}{\partial r}\frac{\partial}{\partial r}(rA_\theta)\right) + \frac{\partial^2 A_\phi}{\partial z^2} = -\mu J_\phi$.

Because we know that A_r and A_z are both 0 we can conclude from Equation (A-22) that

$$E = -\frac{\partial A}{\partial t} = -\frac{\partial A_\phi}{\partial t} \tag{A-35}$$

Also from Equation (A-11) $B \equiv \nabla \times A$:

$$B_r = \frac{1}{r}\frac{\partial A_z}{\partial \phi} - \frac{\partial A_\phi}{\partial z} \tag{A-36}$$

$$B_\phi = \frac{\partial A_r}{\partial z} - \frac{\partial A_z}{\partial r} \tag{A-37}$$

$$B_z = \frac{1}{r}\frac{\partial}{\partial r}(rA_\phi) - \frac{1}{r}\frac{\partial A_r}{\partial \phi} \tag{A-38}$$

Once again eliminating all derivatives with respect to ϕ leaves us with

$$B_r = -\frac{\partial A_\phi}{\partial z} \tag{A-39}$$

$$B_z = \frac{1}{r}\frac{\partial}{\partial r}(rA_\phi) \tag{A-40}$$

It can be shown that this implies that $\nabla \bullet B = 0$ by examining the definition of this relationship in conjunction with the relationships for B_r and B_z that were just found.

$$\begin{aligned}
\nabla \bullet B &= \frac{1}{r}\frac{\partial}{\partial r}(rB_r) + \frac{1}{r}\frac{\partial B_\phi}{\partial \phi} + \frac{\partial B_z}{\partial z} \\
&= \frac{1}{r}\frac{\partial}{\partial r}(-r\frac{\partial A_\phi}{\partial z}) + \frac{\partial}{\partial z}(\frac{1}{\partial r}\frac{\partial}{\partial r}(rA_\phi)) \\
&= \frac{-1}{r}\frac{\partial}{\partial r}(r\frac{\partial A_\phi}{\partial z}) + \frac{1}{r}\frac{\partial}{\partial z}(\frac{\partial}{\partial r}(rA_\phi)) \\
&= \frac{-1}{r}\frac{\partial}{\partial r}(r\frac{\partial A_\phi}{\partial z}) + \frac{1}{r}\frac{\partial}{\partial r}(\frac{\partial}{\partial z}(rA_\phi)) \quad =0
\end{aligned}$$

Recall that we were left with Equation (A-33). But, this formulation is not amenable to Galerkin weak formulation, so we let

$$\psi(r,z,t) \equiv rA_{\phi}(r,z,t) \tag{A-40}$$

Subsisting into Equation (A-33) gives

$$\frac{\partial}{\partial r}\left(\frac{1}{\partial r}\left(\frac{\partial \psi}{\partial r}\right)\right) + \frac{\partial}{\partial z}\left(\frac{1}{r}\frac{\partial \psi}{\partial z}\right) = -\mu J_{\phi} \tag{A-41}$$

This remarkably looks like $\nabla \bullet (K\nabla \psi)$, but do not forget that we are in cylindrical coordinates. In cylindrical coordinates, $\nabla \bullet (K\nabla \psi)$, would look like

$$\nabla \bullet (K\nabla \psi) = \frac{1}{\partial r}\frac{\partial}{\partial r}\left(rK\,\frac{\partial \psi}{\partial r}\right) + \frac{\partial}{\partial z}\left(K\,\frac{\partial \psi}{\partial z}\right) \tag{A-42}$$

where, K = 1/r

We will return to the "form" of the equation later as it relates to being solved within a computational fluid dynamics package.

Now, assuming that a solution for $\psi(r,z,t)$ could be obtained, we could post process the solution to obtain

$$A_{\phi} = \frac{\psi}{r} \tag{A-43}$$

$$E_{\phi} = -\frac{1}{r}\frac{\partial \psi}{\partial r} \tag{A-44}$$

$$B_{r} = -\frac{1}{r}\frac{\partial \psi}{\partial z} = -K\,\frac{\partial \psi}{\partial z} \tag{A-45}$$

$$B_{z} = \frac{1}{r}\frac{\partial \psi}{\partial r} = K\,\frac{\partial \psi}{\partial r} \tag{A-46}$$

where, E_{ϕ} is the only item needed to solve for the power density in a crucible.

For the type of engineering problem to be solved here, we want to remove the time-dependence of the problem by seeking the quasi-steady (periodic or time-harmonic) solution associated with the periodic driving force - the alternating current in the coil.

$$J_\phi = J_0(r,z)\exp^{i\omega t} \tag{A-47}$$

In the conductor we have $J = \sigma E$ and recall that

$$\frac{\partial}{\partial r}\left(\frac{1}{r}\frac{\partial \psi}{\partial z}\right) = -\mu J_\phi \tag{A-48}$$

$$\nabla \bullet (K \nabla \psi) = -\mu J_\phi \tag{A-49}$$

and also we have Equation (A-44): $E_\phi = -\frac{1}{r}\frac{\partial \psi}{\partial r}$. This leads to the following equation in the coil

$$\nabla \bullet (K \nabla \psi) = -\mu J_0 \exp^{i\omega t} \tag{A-50}$$

In the conductors we have

$$\nabla \bullet (K \nabla \psi) = -\mu(\sigma E_\phi) = \mu\sigma\left(-\frac{1}{r}\frac{\partial \psi}{\partial r}\right) \tag{A-51}$$

Thus

$$\nabla \bullet (K \nabla \psi) = -\frac{\mu\sigma}{r}\frac{\partial \psi}{\partial r} \tag{A-52}$$

And in the dielectrics

$$\nabla \bullet (K \nabla \psi) = 0 \tag{A-53}$$

But ψ is complex and we to revert to real arithmetic we let

$$J_\phi = J_0 \cos(\omega t) \tag{A-54}$$

$$\psi(r,z,t) = S(r,z)\sin(\omega t) + C(r,z)\cos(\omega t) \tag{A-55}$$

This results in two real equations everywhere within the solution domain. For the coil we have

$$\frac{\partial}{\partial r}\left(\frac{1}{\partial r}\left(\frac{\partial C}{\partial r}\right)\right) + \frac{\partial}{\partial z}\left(\frac{1}{r}\frac{\partial C}{\partial z}\right) = -\mu J_0 \tag{A-56}$$

$$\frac{\partial}{\partial r}\left(\frac{1}{\partial r}\left(\frac{\partial S}{\partial r}\right)\right)+\frac{\partial}{\partial z}\left(\frac{1}{r}\frac{\partial C}{\partial z}S\right)=0 \tag{A-57}$$

In the conductors this results in

$$\frac{\partial}{\partial r}\left(\frac{1}{\partial r}\left(\frac{\partial C}{\partial r}\right)\right)+\frac{\partial}{\partial z}\left(\frac{1}{r}\frac{\partial C}{\partial z}\right)=\frac{\mu\sigma\omega}{r}S \tag{A-58}$$

$$\frac{\partial}{\partial r}\left(\frac{1}{\partial r}\left(\frac{\partial S}{\partial r}\right)\right)+\frac{\partial}{\partial z}\left(\frac{1}{r}\frac{\partial C}{\partial z}S\right)=-\frac{\mu\sigma\omega}{r}c \tag{A-59}$$

Everywhere else we end up with

$$\frac{\partial}{\partial r}\left(\frac{1}{\partial r}\left(\frac{\partial C}{\partial r}\right)\right)+\frac{\partial}{\partial z}\left(\frac{1}{r}\frac{\partial C}{\partial z}\right)=0 \tag{A-60}$$

$$\frac{\partial}{\partial r}\left(\frac{1}{\partial r}\left(\frac{\partial S}{\partial r}\right)\right)+\frac{\partial}{\partial z}\left(\frac{1}{r}\frac{\partial C}{\partial z}S\right)=0 \tag{A-61}$$

Rewriting these equations in tensor notation for Cartesian coordinates and a variable K = 1/r gives us:

For coils

$$\nabla\bullet(K\nabla C)=-\mu J_0 \tag{A-62}$$

$$\nabla\bullet(K\nabla S)=0 \tag{A-63}$$

For conductors

$$\nabla\bullet(K\nabla C)=\frac{\mu\sigma\omega}{r}S \tag{A-64}$$

$$\nabla\bullet(K\nabla S)=-\frac{\mu\sigma\omega}{r}C \tag{A-65}$$

and elsewhere

$$\nabla\bullet(K\nabla C)=0 \tag{A-66}$$

$$\nabla\bullet(K\nabla S)=0 \tag{A-67}$$

If we solve these equations with the appropriate boundary conditions, they will yield C(r, z) and S(r, z). Using S and C, we must now determine the power deposited in the conductive components. Recall that power is

$$P = J \bullet E \tag{A-68}$$

Making substitutions of Equations (A-5) and (A-44) into Equations (A-68)

$$P = J \bullet E = J_\phi E_\phi = (\sigma E_\phi) E_\phi = \sigma E_\phi^{\,2}$$
$$= \sigma(-\frac{1}{r}\frac{\partial \psi}{\partial r})^2 = \frac{\sigma}{r^2}(\frac{\partial \psi}{\partial r})^2 \tag{A-69}$$

Determining the time derivative of $\psi\ (r, z, t)$ defined from Equation (A-55) gives

$$\frac{\partial \psi}{\partial t} = \frac{\partial}{\partial t}(S(r,z)\sin(\omega t) + C(r,z)\cos(\omega t))$$
$$= S\omega\cos(\omega t) - C\omega\sin(\omega t) \tag{A-70}$$

Substituting back into the power relationship.

$$P = \frac{\sigma}{r^2}(S\omega\cos(\omega t) - C\omega\sin(\omega t))^2 \tag{A-71}$$

$$P = \frac{\sigma\omega^2}{r^2}(S\cos(\omega t) - C\sin(\omega t))^2 \tag{A-72}$$

To determine the power deposition rate, we need to integrate this over one period.

$$\dot{Q}'''(r,z) \equiv \frac{\omega}{2\pi}\int_0^{\frac{2\pi}{\omega}} P(r,z,t)dt \tag{A-73}$$

$$= \frac{\omega}{2\pi}\frac{\sigma\omega^2}{r^2}\int_0^{\frac{2\pi}{\omega}}(S^2\cos^2(\omega t) - 2SC\cos(\omega t)\sin(\omega t) + C^2\sin^2(\omega t))dt$$

$$= \frac{\omega}{2\pi}\frac{\sigma\omega^2}{r^2}\{[\frac{S^2}{2\omega}\sin(\omega t)\cos(\omega t) + 2t]_0^{\frac{2\pi}{\omega}} - 2SC[\frac{1}{2\omega}\sin^2(\omega t)]_0^{\frac{2\pi}{\omega}}$$
$$+[-\frac{c^2}{2\omega}\cos(\omega t)\sin(\omega t) + \frac{t}{2}]_0^{\frac{2\pi}{\omega}}\}$$

Which reduces to

$$\dot{Q}'''(r,z) = \frac{\sigma\omega^2}{2r^2}(S^2 + C^2) \tag{A-74}$$

The penetration depth, or "skin" depth of the heating is defined as

$$\delta = \sqrt{\frac{2}{\mu\delta\omega}} \tag{A-75}$$

As shown above, there are two coupled equations that must be solved in order to determine the power deposition. The numerical solution of these equations is needed in order to apply a source term within the energy equations.

These equations have previously solved in FIDAP. That implementation used modified versions of the momentum and energy equations to provide a mechanism for the solution of two coupled equations. Currently, we want to solve for the induction heating field in addition to the flow field and the energy equation. In order to do this, a mechanism has to be defined within FIDAP to solve these equations.

It is possible to solve for the transport of 15 different species within FIDAP. The goal is to be able to use two of the species transport equations to determine C and S, which would allow the calculation of a source term within the energy equation.

The species equations within FIDAP, take the following form in vector notation.

$$\rho_0\left(\frac{\partial C_n}{\partial t} + \vec{u} \bullet \nabla C_n\right) = \rho_0 \nabla \bullet (\alpha_n \nabla C_n) + q_{cn} + R_n \tag{A-76}$$

For a steady problem that does not consider velocity for the source term R_n we have

$$\nabla \bullet (\alpha_n \nabla C_n) = -\frac{q_{cn}}{\rho_0} \tag{A-77}$$

Recall the governing equations (A-62- A-67) for the coil, conductors, and all other locations. This results in a situation where the source term q_{cn} within FIDAP has to be set to equal the right-hand-side of the governing equations. The diffusivity α_n is set equal to K which is defined as 1/r - a variable.

Appendix IV – Development of Mass Transfer Model